UNIVERSITY OF CALIFORNIA, SAN DIEGO

Nonlinear Active Metamaterial Surfaces

A Dissertation submitted in partial satisfaction of the
requirements for the degree
Doctor of Philosophy

in

Electrical Engineering (Electronic Circuits and Systems)

by

Sanghoon Kim

Committee in charge:

Professor Daniel F. Sievenpiper, Chair
Professor Todd P. Coleman
Professor William S. Hodgkiss
Professor Boubacar Kante
Professor Vitaliy Lomakin

2017

The Dissertation of Sanghoon Kim is approved, and it is acceptable in quality and form for publication on microfilm and electronically:

_____

_____

_____

_____

_____

Chair

University of California, San Diego

2017

DEDICATION

To my beloved wife *Jung-A Chu* and adorable angel *Dana Kim*,

and my parents Mr. *Sung-Soo Kim* and Mrs. *Seung-Ok Jang*.

TABLE OF CONTENTS

LIST OF FIGURES

LIST OF TABLES

LIST OF ABBREVIATIONS

EBG	Electromagnetic band gap
HIS	High impedance surface
TEM	Transverse electromagnetic
EM	Electromagnetic
TE	Transverse electric
TM	Transverse magnetic
RF	Radio frequency
DC	Direct current
PEC	Perfect electric conductor
PMC	Perfect magnetic conductor
AMC	Artificial magnetic conductor
TRM	Transverse resonance method
magRAM	Magnetic radar absorbing material
MOSFET	Metal-oxide-semiconductor field effect transistor
MEMS	Micro-electro mechanical sensor
LNA	Low noise amplifier

ACKNOWLEDGEMENTS

I would like to express the greatest appreciation to my advisor, Professor Daniel F. Sievenpiper. Without his great supervision and sincere support, this research would not have been completed and I could not have derived as much fun from my life and research in San Diego. I would like to show my appreciation to my committee members, Professor Boubacar Kante, Professor Vitaliy Lomakin, Professor Todd P. Coleman, and Professor William S. Hodgkiss, for taking the time to be part of my committee and for their comments and suggestions. A special thank my parents, family, and friends, and especially everyone in the Applied Electromagnetics Group.

The material in this dissertation is based on the following papers which are either published or preparation for publication.

Chapter 2 is based on and is mostly a reprint of the following paper: **S. Kim**, D. Sievenpiper, "Theoretical Limitations for TM Surface Wave Attenuation by Lossy Coatings on Conductive Surfaces", *IEEE Transactions on Antennas and Propagation*, vol. **62**, no.1, pp.475-480, January 2014. The dissertation author was the primary author of the work of the material in this paper, and the co-author has approved the use of the material for this dissertation.

Chapter 3 is based on and is mostly a reprint of the following papers: **S. Kim**, H. Wakatsuchi, J. Rushton, D. Sievenpiper, "Switchable Nonlinear Metasurfaces for Absorbing High Power Surface Waves", *Applied Physics Letters* **108**, 041903, 2016.; **S. Kim**, H. Wakatsuchi, J. Rushton, D. Sievenpiper, "Nonlinear Metamaterial Surfaces for Absorption of High Power Microwave Surface Currents", IEEE Antennas and Propagation Symposium Digest, Orlando, FL, USA, July 8-14, 2013. The dissertation author was the primary author of the work of the material in these papers, and the co-authors have approved the use of the

material for this dissertation.

Chapter 4 is based on and is mostly a reprint of the following paper: **S. Kim**, A. Li, D. Sievenpiper, "Self-Tuning Metamaterial Surfaces", in preparation. The dissertation author was the primary author of the work of the material in this paper, and the coauthors have approved the use of the material for this dissertation.

Chapter 5 is based on and is mostly a reprint of the following paper: **S. Kim**, A. Li, D. Sievenpiper, "Reconfigurable Impedance Ground Plane for Broadband Antenna Systems", 2017 IEEE Antennas and Propagation Symposium, San Diego, CA, July 9, 2017. The dissertation author was the primary author of the work of the material in this paper, and the co-authors have approved the use of the material for this dissertation.

Chapter 6 is based on and is mostly a reprint of the following paper: **S. Kim**, A. Li, D. Sievenpiper, Omni-directional metamaterial surface, in preparation. The dissertation author was the primary author of the work of the material in this paper, and the co-authors have approved the use of the material for this dissertation.

Sanghoon Kim

La Jolla, CA

June 2017

VITA

2005	Bachelor of Science in Physics, *Summa cum laude*, Konkuk University, Seoul, Korea
2008	Master of Science in Physics, Konkuk University, Seoul, Korea
2010-2017	Graduate Student Researcher, University of California, San Diego, U.S.A.
2017	Doctor of Philosophy in Electrical Engineering (Electronic Circuits and Systems), University of California, San Diego, U.S.A.

PUBLICATIONS

Journal Articles

S. Kim, A. Li, D. Sievenpiper, "Omni-Directional Metamaterial Surfaces", in preparation.

S. Kim, A. Li, D. Sievenpiper, "Self-Tuning Metamaterial Surfaces", in preparation.

Y. Luo, **S. Kim**, A. Li, D. Sievenpiper, "The Advantages of Nonlinear Metasurface in Bandwidth and Magnitude", in preparation.

A. Li, **S. Kim**, Y. Luo, Y. Li, J. Long, D. Sievenpiper, "High-Power, Transistor-Based Tunable and Switchable Metasurface Absorber", accepted for publication.

S. Kim, H. Wakatsuchi, J. Rushton, D. Sievenpiper, "Switchable Nonlinear Metasurfaces for Absorbing High Power Surface Waves", *Applied Physics Letters* **108**, 041903, 2016.

H. Wakatsuchi, D. Anzai, J. Rushton, F. Gao, **S. Kim**, D. Sievenpiper, "Waveform selectivity at the same frequency", *Scientific Reports* **5**, Article 9639, 2015.

S. Kim, D. Sievenpiper, "Theoretical Limitations for TM Surface Wave Attenuation by Lossy Coatings on Conductive Surfaces", *IEEE Transactions on Antennas and Propagation*, vol. **62**, no.1, pp.475-480, January 2014.

H. Wakatsuchi, **S. Kim**, J. Rushton, D. Sievenpiper, "Waveform-Dependent Absorbing Metasurfaces", *Physical Review Letters* **111**, 245501, December 2013.

H. Wakatsuchi, J. Rushton, J. Lee, F. Gao, M. Jacob, **S. Kim**, D. F. Sievenpiper, "Experimental Demonstration of Nonlinear Waveform-Dependent Metasurface Absorber with Pulsed Signals", *Electronics Letters*, vol. **49**, no.24, pp.1530-1531, November 2013.

H. Wakatsuchi, **S. Kim**, J. Rushton, D. Sievenpiper, "Circuit-based nonlinear metasurface absorbers for high power surface currents", *Applied Physics Letters* **102**, 214103, 2013.

D. Sievenpiper, D. Dawson, M. Jacob, T. Kanar, **S. Kim**, J. Long, R. Quarfoth, "Experimental Validation of Performance Limits and Design Guidelines for Small Antennas", *IEEE Transactions on Antennas and Propagation*, vol. **60**, no. 1, pp. 8-19, January 2012.

Conference Papers

S. Kim, A. Li, D. Sievenpiper, "Reconfigurable Impedance Ground Plane for Broadband Antenna Systems", 2017 IEEE Antennas and Propagation Symposium, San Diego, CA, July 9, 2017

A. Li, E. Forati, **S. Kim**, J. Lee, Y. Li, D. Sievenpiper, Periodic Structures for Scalable High-Power Microwave Transimitters, 2017 IEEE Antennas and Propagation Symposium, San Diego, CA, July 9, 2017

D. Sievenpiper, **S. Kim**, A. Li, J. Long, J. Lee, "Advances in Nonlinear, Active, and Anisotropic Artificial Impedance Surfaces", 2016 European Microwave Conference, London, United Kingdom, October 6, 2016.

H. Wakatsuchi, J. Rushton, **S. Kim**, D. Sievenpiper, "Metasurfaces to Select Waveforms at the Same Frequency", 8th International Congress on Advanced Electromagnetic Materials in Microwaves and Optics, pp. 286-288, 2014.

S. Kim, H. Wakatsuchi, J. Rushton, D. Sievenpiper, "Nonlinear Metamaterial Surfaces for Absorption of High Power Microwave Surface Currents", IEEE Antennas and Propagation Symposium Digest, Orlando, FL, USA, July 8-14, 2013.

H. Wakatsuchi, **S. Kim**, J. Rushton, D. Sievenpiper, "Numerical and experimental demonstration of nonlinear metamaterial surfaces designed for high power surface current absorption", Metamaterials 2012: The Sixth International Congress on Advanced Electromagnetic Materials in Microwaves and Optics, St. Petersberg, Russia, September 17-22, 2012.

ABSTRACT OF THE DISSERTATION

Nonlinear Active Metamaterial Surfaces

by

Sanghoon Kim

Doctor of Philosophy in Electrical Engineering (Electronic Circuits and Systems)

University of California, San Diego, 2017

Professor Daniel F. Sievenpiper, Chair

Nonlinear active metamaterial surfaces are constructed of planar periodic engineered structures in the sub-wavelength ($\ll \lambda/4$) scale on which the nonlinear circuit components have been populated. Unusual electromagnetic properties of the metamaterials derived by the resonant behavior of the constitutive unit cells have produced remarkable effects such as negative index of refraction, cloaking, and an electromagnetic band gap due to high impedance, while the implementations are restricted in bandwidth and polarization.

The added nonlinearity from the nonlinear components can give the degree of freedom to achieve the unique and useful functionalities which could not be realized

with linear and passive metamaterials. This thesis studies the theory, characterization, and capability of nonlinear active metasurfaces. The primary application of the invented metasurfaces is focused on exploring a new type of microwave absorbing structure, and the other unique electromagnetic properties.

The state-of-the-art nonlinear circuits deployed on the metasurface offer the adaptive capabilities to tune the inherited electromagnetic properties. First, the theoretical limitations of the linear lossy coating are addressed to establish the necessity for the need for advanced absorbing structures. Subsequent chapters introduce the invented nonlinear metasurfaces with the different tunabilities, specifically the switchable metasurfaces that selectively absorb high power signals to avoid destructive interference to sensitive electronic devices. The self-tuning metasurfaces adaptively tune the resonance frequencies to match the frequencies of the incident waves for broadband absorbing bandwidth. The reconfigurable impedance surface has octave tunability maintaining the artificial magnetic conductor property to support an extreme broadband antenna system, and the omni-directional metamaterial surface to response all-directional incoming waves to minimize unexpected scattering effects in oblique angles.

Chapter 1

Introduction

Microwave technology has been developed extensively over cross-disciplinary scientific fields for the antenna, radar, wireless and satellite communications, as well as other applications, ever since the invention of a coherer as a radio signal detector [1]. With the increase in microwave applications, modern electronics and sensitive antennas are easily exposed to interference from external microwave signals. Specifically, when high power signals impinge on a conductive enclosure, surface currents can cause interference that triggers faults or malfunctions of the enclosed electronic devices [2].

Hence, the demand for a lightweight and electrically thin adaptive surface coating to act as a microwave absorber to minimize the unexpected interference from the threat of the surface currents by actively adjusting their frequency of optimum absorption in response to the incoming high power radiation.

1.1 Motivation

Interference due to surface currents, which is induced when microwaves impinge on the metallic enclosure, arises as a common issue in wireless communication and other sensitive electronic systems. The interference may cause damage because of penetration of high power signals through even a tiny opening, gap, or nearby aperture on a shared conductive shielded system as shown in Fig. 1.1.

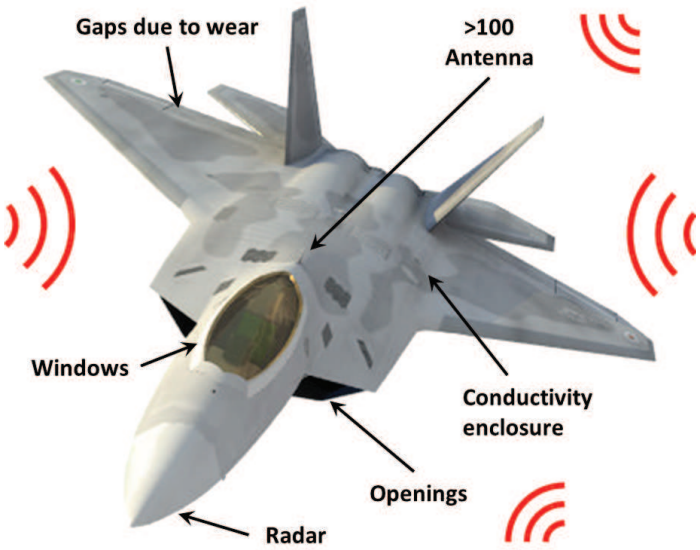

Figure 1.1: Possible interference points on the conductive enclosure.

Available conventional approaches to treat this issue are to use microwave absorbing materials such as pyramidal absorbing forms and magnetic radar absorbing materials for a broadband absorber. Also, artificial structures such as Salisbury screen [3, 4, 5] or resistive sheets are used to dissipate the energy of the surface currents as a resonant absorber. While applying a reactive surface or a lossy coating can mitigate leakage, scattered waves due to impedance mismatches at the boundary between reactive and nonreactive regions can disturb aspects of the systems as shown in Fig. 1.2. In practice for many applications, the

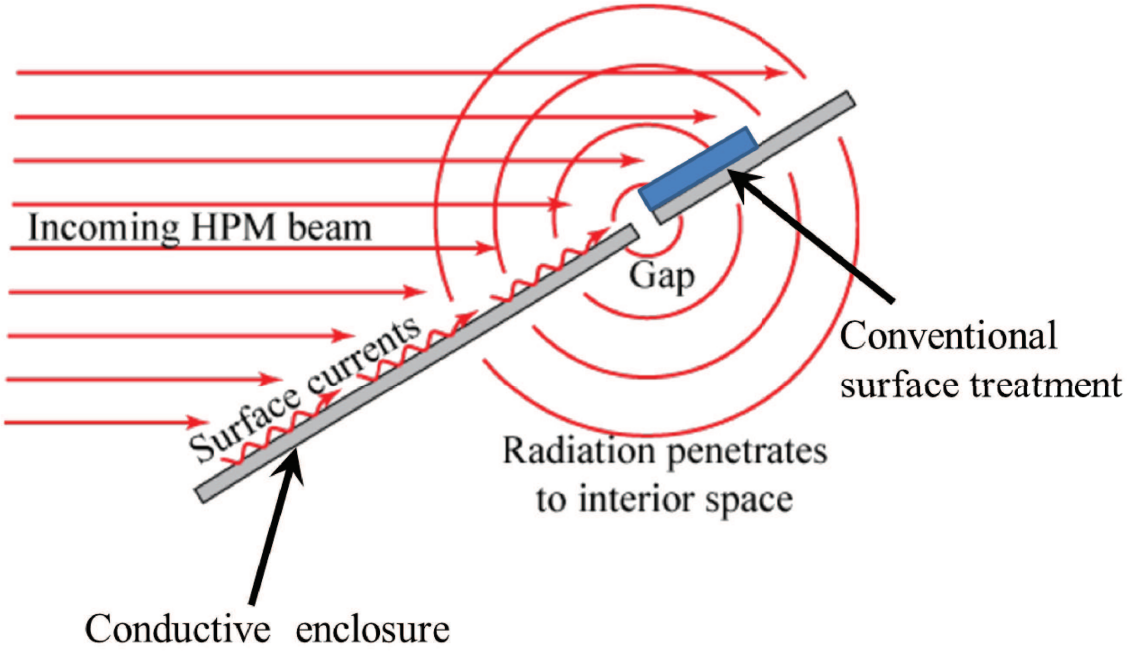

Figure 1.2: Leakage fields through an electronically tiny gap, although linear absorbing coatings or reactive surfaces are partially covered on the conductive body.

absorbers are prohibitive due to the large dimensions, high cost, and heavy weight, and the absorbing coating may reduce the electronic performances that share the same platform. Based on the difficulty of applying conventional approaches, there is demand for a novel method that would not only minimize disturbances of low power signals in the system, but also strongly absorb undesired surface currents of high power radiations.

Other possible approaches are to apply a reactive coating such as a high-impedance surface [6, 7] or metamaterials [8] to block the flow of the induced surface currents. The band diagram of the high impedance surface shown in Fig. 1.3 exhibits an electromagnetic band gap (EBG). By changing the band edge, where the interaction between the surface and wave is greatest, it may be possible to build an adaptive surface that absorbs the power incoming signals. The nonlinear adaptivity by the diodes can be achieved by rectifying incoming signals to static fields. The output result that has been Fourier-transformed (i.e.

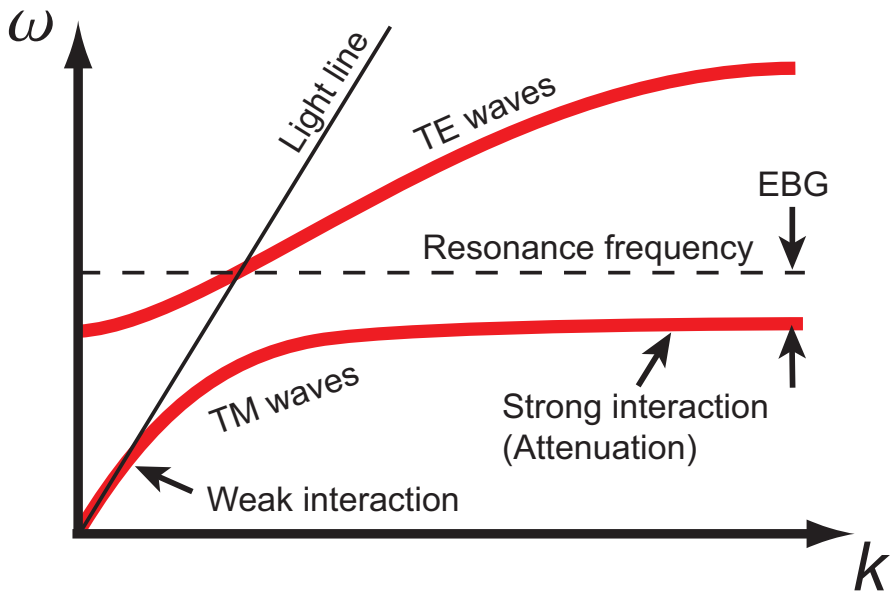

Figure 1.3: Dispersion diagram of the high impedance surface.

$\int_{-\infty}^{\infty}\cos(2\pi ft)\exp(-j2\pi t)dt)$ of the input signal contains only f term. The surface currents from the microwave illuminated on the conductive enclosure result in an infinite set of the spectrum with decreasing magnitude by the Fourier transform. The largest term is a DC or static term of the full-wave rectification, and the second harmonic term from the half-wave rectification can be a useful term. All higher harmonic terms of the Fourier transformation are addressed in Table. 1.1. Additionally, although the artificially engineered structures are

Table 1.1: Fourier components of various modes for half- and full-wave rectifications

Fourier term	W/O Rectification cos	Half-Wave Rectification $(\cos+\lvert\cos\rvert)/2$	Full-Wave Rectification $\lvert\cos\rvert$
0	0	$1/\pi$	2π
f	1/2	1/4	0
$2f$	0	$1/(3\pi)$	$2/(3\pi)$
$3f$	0	0	0
$4f$	0	$-1/(15\pi)$	$-2/(15\pi)$

able to work as the absorber, there will be significant scattering into free space or backward reflections to other systems which are sharing the same platform, while the reactive coating does not cover the entire outer structure of interest. Therefore, a new type of nonlinear metasurface such as an adaptive absorber is needed to mitigate high surface currents for decoupling other sensitive components of the shared conductive body.

1.2 Metamaterial Surfaces

In nature, each material has unique properties to distinguish itself. Permittivity and permeability factors define electromagnetic properties such as wave parameters including the index of refraction (1.1), corresponding wavelength (1.2), and wave impedance (1.3) of the medium.

$$n = \sqrt{\frac{\varepsilon}{\mu}} \tag{1.1}$$

$$\lambda_m = \frac{\lambda}{\sqrt{\varepsilon\mu}} \tag{1.2}$$

$$Z = \sqrt{\frac{\mu}{\varepsilon}} \tag{1.3}$$

The index of refraction is one of the fundamental factors to exhibit the electromagnetic phenomena, called Snell's law; the interactions on the interface between two different mediums, when electromagnetic radiation is incident at an oblique angle. The indices of refraction of all materials that exist in natural environments exhibit positive values. However, a Russian physicist, Veselago, has theoretically reported that the negative index of refraction

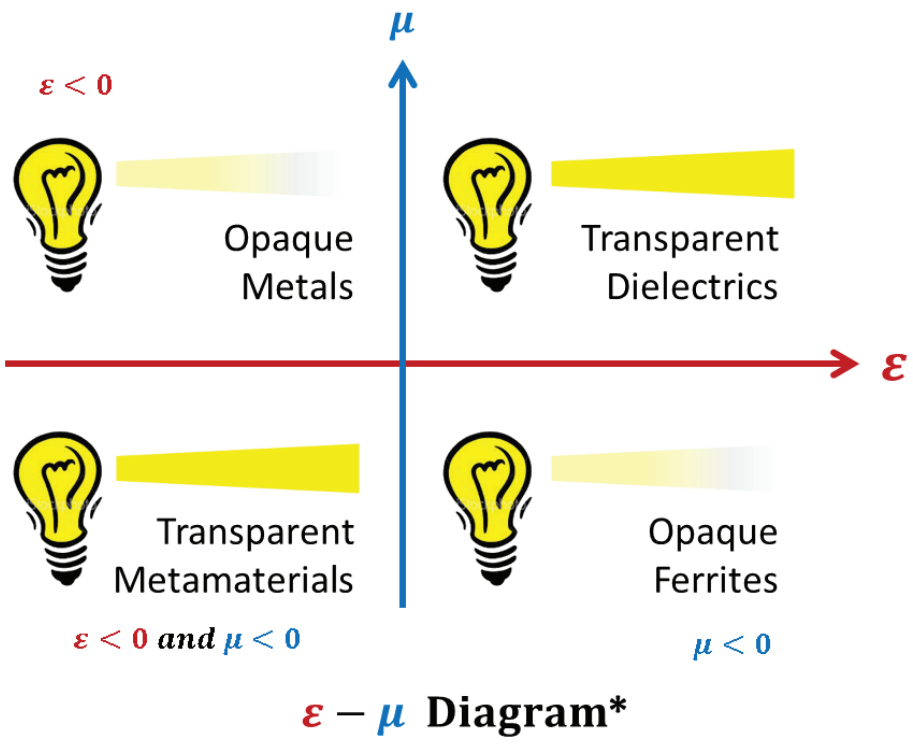

Figure 1.4: The index of refraction in ε - μ diagram.

exists, and such materials do not violate any fundamental physical laws [9]. The negative index medium has unusual electromagnetic characteristics unlike ordinary materials, so it was termed a 'left-handed' material as shown in Fig. 1.4.

Since the first experimental verification of a negative index of refraction materials [10], termed metamaterials, the new field of electromagnetics has aroused new interest. The initial area of the metamaterials has focused on the negative index of refraction, and applications of cloaking structures [11]. The relevant implementations have been expanded to the spectral range, from radio [12], microwave [13], mm-Wave [14], THz [15], near infrared [16], to optical [17, 18]. Today, metamaterials have defined periodic engineered structures in the sub-wavelength ($\lambda_m << \frac{\lambda}{4}$) scale. Electromagnetic properties of the artificial materials are derived from their geometry like an effective medium including effective

permittivity and permeability rather than inheriting them directly from their material composition [19]. The research agenda in the metamaterial fields is now shifting from the negative index superlens towards the emerging field of meta-devices achieving unique and useful functionalities such as tunable, switchable, nonlinear and sensing [20].

Among different types of metamaterials, the planar metamaterial structures, termed as metasurfaces [21, 22, 23, 24, 25, 26], manipulate of electromagnetic waves by densely arranged periodic structures in a two-dimensional area. The metasurface bounds the electric and magnetic polarizations, and modifies over the reflected and transmitted waves for the novel applications in the microwave and optical regions [27].

The high impedance surface [6], one of the conventional metasurfaces, has been described as a two-dimensional dense array with an electrically thin substrate, which totally reflects an incident plane wave in-phase and supports no bounded surface waves on the surface interface as shown in Fig. 1.5. In other words, the image current results in constructive interference termed a perfect magnetic conductor (PMC) or artificial magnetic conductor (AMC), instead of destructive on a perfect electric conductor (PEC).

The unit cell of a high impedance surface shown in Fig. 1.6 is constructed of an array of metal plates at sub-wavelength ($\lambda/10$) scale connected to a ground plane by vertical conductive vias. Its surface impedance is typically modeled as a parallel LC resonance circuit, in which the induced capacitance is provided by the metal plates, and the induced inductance is associated with the conductive path that links neighboring plates through the vertical vias and the ground plane. Near the LC resonance frequency, the structure has high surface impedance and suppresses surface current propagation. In other words, the high impedance surface relates to an electromagnetic band gap which represents a forbidden spontaneous emission in periodic structures within a finite frequency band at the resonance

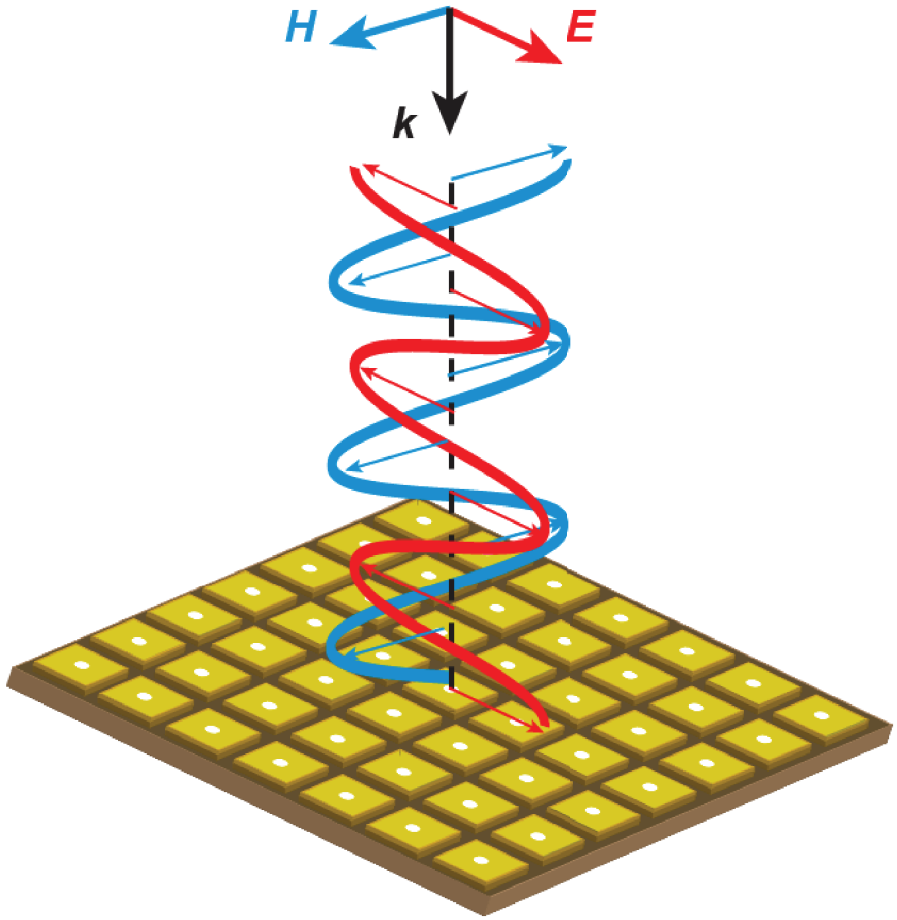

Figure 1.5: Artificial magnetic conductor properties of the high impedance surface.

frequency. In this regime corresponding to a high capacitive surface impedance, neither TM nor TE surface waves are allowed to propagate on the surface, which drives an exponential decay in both fields in the surface plane and provides considerable absorptivity in use of the low profile absorbing structures.

The metasurfaces using a microwave absorber are limited by their narrow bandwidth, which is generally determined by their substrate thickness. Hence, applying nonlinear components such as diodes and transistors will give an additional degree of freedom that cannot be easily achieved with linear materials. The proposed nonlinear active metasurfaces can convert the incident waves into a different frequency, mode, or polarization, to allow

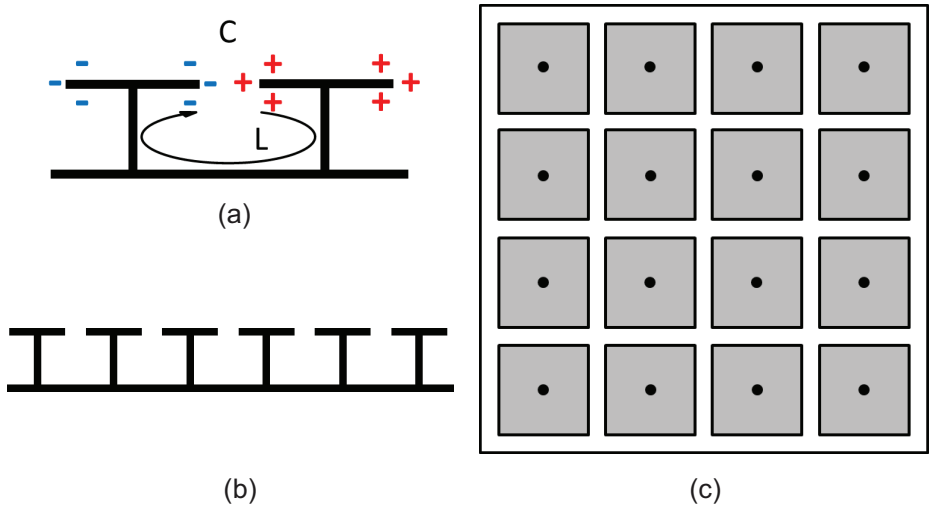

Figure 1.6: Scheme of the high impedance surface (HIS).

alternative absorbing mechanisms.

1.3 Dissertation Organization

This thesis presents the unique electromagnetic functionalities and applications of the nonlinear active metasurfaces for protection of sensitive electronic devices and high performance communication systems, and objectively analyze nonlinear advantages taking into account the possible applications in the advanced electromagnetic fields.

Chapter 1 is an overview of the motivation behind the dissertation, fundamental properties of the metamaterial surfaces, and a brief introduction of the nonlinear advantages.

Chapter 2 addresses analytical and numerical methods to examine theoretical limitations for TM surface wave attenuation by lossy impedance boundaries on conductive surfaces.

Chapter 3 presents analysis, simulation, and measurement results of the switchable metasurface for the power dependent absorber. New measurement systems are also proposed

to measure suppression of surface currents and leakage fields through an electrically tiny gap.

Chapter 4 studies the concept of the self-tunability. A feedback circuit with the slope detector and RF-DC rectifier is introduced to detect and generate the desired DC bias to achieve the active adjustments of the self-tuning metasurface following incoming frequencies.

Chapter 5 examines using the octave-tunability to systematically manipulate surface impedance by MOSFET transistors. The reconfigurable ground plane can be reconfigured to support advanced antenna systems.

Chapter 6 explores anisotropic surface topologies that exhibit all-directional responses against incoming waves.

Chapter 7 summarizes and concludes the thesis, and addresses directions for further research.

Chapter 2

Theoretical Limitations for TM Surface Wave Attenuation by Lossy Coatings on Conducting Surfaces

In this chapter, the theoretical limitations for TM surface wave attenuation on lossy coated conducting surfaces containing electric and/or magnetic loss are analyzed by analytical and numerical methods. The proposed analytical approaches are consistent with numerical simulation data. A simple expression to approximate a wide range of material properties is proposed in this chapter. Furthermore, lossy slabs with simple equivalent circuit boundaries on top are analyzed, which may be provided by frequency selective surfaces or other patterned structures. Such composite lossy coating can exceed the attenuation of a simple lossy slab, but with limited bandwidth. Additionally, only through increasing permeability, and not permittivity, can the peak absorption frequency be lowered for a given thickness without reducing the relative absorption bandwidth.

2.1 Overview of TM Surface Wave Attenuation

A grounded dielectric slab can support bound surface waves [28, 29]. The bound waves are related to the ordinary surface currents that occur in any metal surface in the limit where the dielectric thickness approaches zero. The surface currents contribute significantly to interference between nearby antennas or electronics [30, 2], and suppressing the currents such as by using a lossy coating can be an important tool for interference reduction [6, 31]. An analytical solution to the attenuation by a dielectric slab has been provided by Attwood [32], where he calculated loss terms for both the conductor loss in the metal surface and dielectric loss due to the slab. However, there has been no attempt to analyze general trends or theoretical limits of the attenuation by lossy coatings, particularly for surface waves. The most relevant general analysis is for plane waves at normal incidence [33]. Furthermore, Attwoods original analysis cannot be applied to many modern lossy coatings that may contain magnetic materials, as well as patterned composite materials such as frequency selective surfaces [34] or metamaterials [35]. In this work, we extend Attwood's analysis to include both of these effects and we verify our analytical solution with numerical simulations. We refer to lossy slabs that may contain impedance sheets, frequency selective surfaces (FSS), or other such structures collectively as "coatings." Our analytical solution allows us to sweep a wide range of material properties to derive general trends and establish theoretical limits. In particular, we find that the attenuation by a lossy slab can be approximated by a simple formula. Adding an impedance sheet on top of the slab that can be described by an equivalent circuit can provide greater attenuation than the slab alone, but over limited bandwidth. Thus, lossy coatings combined with frequency selective surfaces, metamaterials or other such patterned surfaces can be effective narrowband absorbers. A transverse magnetic (TM) type wave is assumed to be a uniform surface wave propagating parallel to

the surface of a dielectric slab on a conducting surface. We focus on TM waves because most absorbing coatings are electrically thin, however because the purpose of this paper is to establish trends, we will study a wide range of thicknesses. We follow Attwood's analysis and label the conductor as region 1, the slab as region 2 and the surrounding air as region 3. In order to consider only the effects of the slab, we assume that region 1 is a perfect electric conductor as shown in Fig. 2.1. Region 2 is a dielectric material of thickness 'a' with relative permittivity (ε) and permeability (μ). The loss properties are represented by the imaginary permittivity (ε_2'') and permeability (μ_2''). In region 3, we assume the material outside of the dielectric slab is air with relative permittivity and permeability of unity. We also consider the case where an impedance sheet is located between the slab and the air region. The sheet is considered to have an infinitesimal thickness such as a thin frequency selective surface [34].

2.2 Analytical Solution

To determine the theoretical limitations of attenuation by a lossy slab, first, we consider an analytical solution. The analytical solution is developed from Maxwell's equations, assuming a traveling TM surface wave. We follow Attwood's analysis [32] and also add the effects of magnetic loss, and lossy or reactive impedance sheets.

2.2.1 Without Impedance Sheet

For the transverse fields in the slab and air regions, we first start with Maxwell's equations under source-free, linear and homogeneous space conditions.

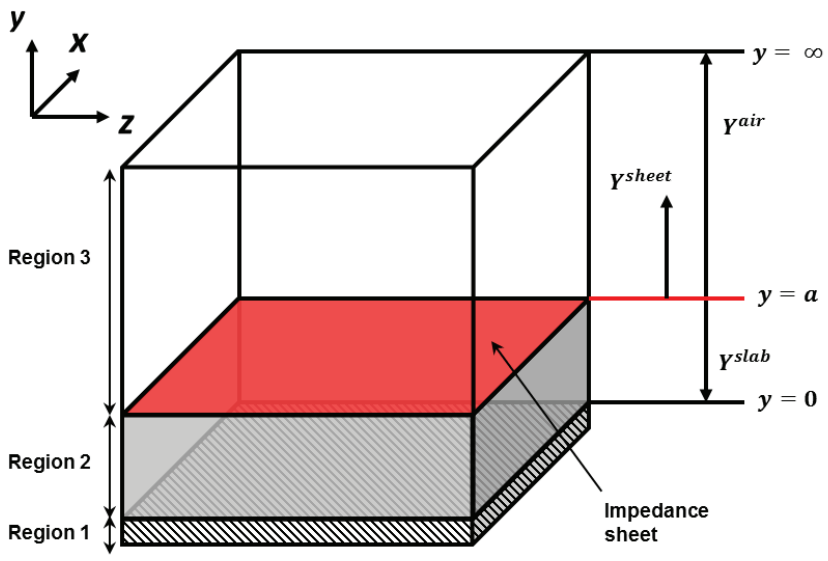

Figure 2.1: Geometry for TM surface wave propagating along the direction with the electric field decaying in the *y*-direction. Schematic of the structure and properties of materials; region 1 is assumed to be a perfect conductor ($\sigma = \infty$), region 2 is a slab of thickness a with loss properties, given by the imaginary components of relative permittivity (ε_2'') and permeability (μ_2''), region 3 is air. There is a possible impedance sheet between the region 2 and region 3.

$$\begin{aligned} \nabla \bullet E &= 0 \\ \nabla \bullet B &= 0 \\ \nabla \times E &= -j\omega\mu H \\ \nabla \times H &= j\omega\varepsilon E \end{aligned} \tag{2.1}$$

A propagating TM surface wave along the z-direction is considered as a monochromatic wave. The wave components are functions of y, and independent of x. Therefore, Maxwells equations (2.1) are reduced to below.

$$\begin{aligned}
\frac{\partial E_y}{\partial y} - j\beta E_z &= 0 \\
\frac{\partial E_z}{\partial y} + j\beta E_y &= -j\omega\mu H_x \\
-j\beta H_x &= j\omega\varepsilon E_y \\
-\frac{\partial H_x}{\partial y} &= j\omega\varepsilon E_z
\end{aligned} \tag{2.2}$$

To obtain the propagating field E_z as a wave equation, we differentiate (2.2) with respect to the y direction, and then combine both equations. The equation represents the electric field along propagating direction, E_z, as below.

$$\frac{\partial^2 E_z}{\partial y^2} = -(\omega^2\mu\varepsilon - \beta^2)E_z \tag{2.3}$$

Following a similar procedure, we can derive equations for the transverse fields in the y and x vector components, E_y and H_x, respectively.

$$\frac{\partial^2 E_y}{\partial y^2} = -(\omega^2\mu\varepsilon - \beta^2)E_y \tag{2.4}$$

$$\frac{\partial^2 H_x}{\partial y^2} = -(\omega^2\mu\varepsilon - \beta^2)H_x \tag{2.5}$$

From above field components, (2.3), (2.4), and (2.6), a propagation constant is represented in which the wave number β which must be real. The propagation constant k along the y-direction is given by

$$k^2 = \omega^2\mu\varepsilon - \beta^2 = \left(\frac{\omega}{c}\right)^2 \mu_r\varepsilon_r - \beta^2 \tag{2.6}$$

Here, c is the speed of light.

We assume equations for the fields as below.

$$\begin{aligned} E_z &= \frac{1}{2}(Ae^{+jky} + Be^{-jky}) \\ E_y &= \frac{1}{2}(Ae^{+jky} + Be^{-jky}) \\ H_x &= \frac{1}{2}(Ae^{+jky} + Be^{-jky}) \end{aligned} \tag{2.7}$$

We applied the above field equations to the structure as shown in Fig. 2.1. In the slab, we have an equation to represent the tangential electric field at the conductor boundary $y = 0$, where the boundary conditions are $E_{z2} = 0$, and therefore $B_2 = -A_2$, where subscript 2 represents region 2, the slab. Thus, we have

$$E_{x2} = \frac{1}{2}A_2(e^{+jk_2y} - e^{-jk_2y}) = jA_2\sin(k_2y) \tag{2.8}$$

In a similar manner, we have equations for the other transverse fields below.

$$E_{y2} = \frac{1}{2}A_2\frac{\beta}{k_2}(e^{+jk_2y} + e^{-jk_2y}) = A_2\frac{\beta}{k_2}\cos(k_2y) \tag{2.9}$$

$$H_{x2} = -\frac{1}{2}A_2\frac{\omega\varepsilon_2}{k_2}(e^{+jk_2y} + e^{-jk_2y}) = -A_2\frac{\omega\varepsilon_2}{k_2}\cos(k_2y) \tag{2.10}$$

From (2.8), (2.9), and (2.10), we see that inside the slab the unattenuated field components are sinusoidally distributed in the z-direction. On the other hand, in the air region the fields are exponentially decaying in the y-direction, so k_3 is imaginary and $B_3 = 0$, where subscript 3 represents region 3, the air region.

$$\begin{aligned} E_{z3} &= (A_3e^{+jk_3y} + B_3e^{-jk_3y}) \\ &= jA_3e^{-jk_3y} \end{aligned} \tag{2.11}$$

The electric field in (2.8) and (2.11) must be same at the dielectric boundary $y = a$, so A_3 can be represented in terms of A_2.

$$A_3 = A_2 e^{+k_3 a} \sin(k_2 a) \tag{2.12}$$

Therefore, we have an equation for the electric field at the air region in z-direction.

$$E_{z3} = +jA_2 e^{+k_3 a} \sin(k_2 a) e^{-k_3 y} \tag{2.13}$$

By using similar methods, we can obtain transverse fields in the air region, E_{y3} and H_{x3} respectively. From (2.10) by considering $K_z = -A_2(\omega\varepsilon_2/k_2)$ we rewrite the field components on both dielectric regions, below. For the dielectric slab in region 2,

$$E_{z2}^{slab} = jK_z \frac{k_2}{\omega\varepsilon_2} \sin(k_2 y), \tag{2.14}$$

$$E_{y2}^{slab} = K_z \frac{\beta}{\omega\varepsilon_2} \cos(k_2 y), \tag{2.15}$$

$$H_{x2}^{slab} = -K_z cos(k_2 y). \tag{2.16}$$

For the air in region 3,

$$E_{z3}^{air} = jK_z \frac{k_2}{\omega\varepsilon_2} \exp^{+k_3 a} \sin(k_2 a) \exp^{-k_3 y}, \tag{2.17}$$

$$E_{y3}^{air} = K_z \frac{k_2}{k_3} \frac{\beta}{\omega\varepsilon_2} \exp^{+k_3 a} \sin(k_2 a) \exp^{-k_3 y}, \tag{2.18}$$

$$H_{x3}^{air} = -K\frac{k_2}{k_3}\frac{\varepsilon_3}{\varepsilon_2}\exp^{+k_3 a}\sin(k_2 a)\exp^{-k_3 y}. \tag{2.19}$$

Here, K_z is an amplitude of tangential component in (2.15) of the slab, $K_z \propto -(\omega\varepsilon_2/k_2)$. The relations between the propagation factor, permittivity, permeability and frequency in both regions are developed from the wave equation. The relations are represented below.

$$k_2^2 = \omega^2\mu_2\varepsilon_2 - \beta^2, \tag{2.20}$$

$$(jk_3)^2 = -k_3^2 = \omega^2\mu_3\varepsilon_3 - \beta^2, \tag{2.21}$$

$$k_2^2 + k_3^2 = \omega^2(\mu_2\varepsilon_2 - \mu_3\varepsilon_3). \tag{2.22}$$

At the boundary, $y = a$, the impedance is continuous, because the tangential components of electric field E and magnetic field H are continuous. From this condition, the propagation constant in the air region is represented as below.

$$k_3 = k_2\frac{\varepsilon_3}{\varepsilon_2}\tan(k_2 a) \tag{2.23}$$

Substituting (2.23) into (2.22), we obtain an equation for the propagation constant in the slab.

$$k_2^2\left[1 + \frac{\varepsilon_3^2}{\varepsilon_2^2}\tan^2(k_2 a)\right] = \omega(\mu_2\varepsilon_2 - \mu_3\varepsilon_3) \tag{2.24}$$

Using the above relations, we can solve for β, k_2 and k_3 from (2.21), (2.24) and

(2.23). In formulating an equation for the attenuation by the loss properties of the slab, we had to consider the fields in both dielectric and air regions. The attenuation is proportional to the time average loss in the slab and to the time average power of the wave propagating in both regions. To obtain the time average power propagating along the z-direction, we determine the time average Poynting vector in both regions.

$$P_z = -\frac{1}{2}\int_{y=0}^{y=a} Re[E_{y2}H_{x2}^*]dy - \frac{1}{2}\int_{y=a}^{y=\infty} Re[E_{y3}H_{x3}^*]dy \tag{2.25}$$

In (2.25), the first term represents the time average power in the slab, and the second term represents the time average power of the air region. Each field components are from (2.15), complex conjugate of (2.15), (2.17), and complex conjugate of (2.18). Hence, in each region, the time average propagating power is derived as below. For the slab,

$$\overline{P_{z2}^{slab}} = +K_z^2 \frac{1}{4k_2}\frac{\beta}{\omega\varepsilon_2}\left[k_2 a + \frac{1}{2}\sin(2k_2 a)\right]. \tag{2.26}$$

For the air region,

$$\overline{P_{z3}^{air}} = +K_z^2 \frac{1}{4}\frac{\varepsilon_3}{\varepsilon_2}\frac{k_2^2}{k_3^3}\frac{\beta}{\omega\varepsilon_2}\sin^2(k_2 a). \tag{2.27}$$

To obtain the time average loss in the slab including both dielectric and magnetic loss, we calculate the real power dissipated in the slab.

$$\begin{aligned}\overline{P_{loss}} &= \int_{y=0}^{y=a}\left[\frac{\omega}{2}\varepsilon''|E|^2 + \frac{\omega}{2}\mu''|H|^2\right]dy \\ &= \int_{y=0}^{y=a}\left[\frac{\omega}{2}\varepsilon''(E_{y2}\cdot E_{y2}^* + E_{z2}\cdot E_{z2}^*) + \frac{\omega}{2}\mu''(H_{x2}\cdot H_{x2}^*)\right]dy\end{aligned} \tag{2.28}$$

In (2.28), the first term is for electrical loss and the second is for magnetic loss, respectively. Each field components are from (2.14), complex conjugate of (2.16), (2.17),

and complex conjugate of (2.18). Hence, the loss of time average propagating power in the slab with dielectric and magnetic loss properties is given below.

$$\begin{aligned}\overline{P_{loss}^{slab}} = +K_z^2 \frac{\omega\varepsilon''}{4(\omega\varepsilon)^2}\left[(\beta^2+k_2^2)a+\frac{\beta^2-k_2^2}{2k_2}\sin(2k_2a)\right] \\ +K_z^2\frac{\omega\mu''}{4}\left[\frac{1}{2k_2}\sin(2k_2a)+a\right]\end{aligned} \tag{2.29}$$

Finally, the attenuation of TM surface waves on a lossy slab is given by

$$\alpha = \frac{\overline{P_{loss}^{slab}}}{2(\overline{P_{z2}^{slab}}+\overline{P_{z3}^{air}})} \tag{2.30}$$

2.2.2 With Impedance Sheet

In the case of applying the impedance sheet to the top of the slab, we assume it is represented by an equivalent transmission line system in which the slab, the impedance sheet and the air region are connected in parallel. To develop an analytical solution for the attenuation with the impedance sheet, we need to calculate modified propagation constants for both the slab and air regions. The transverse resonance method (TRM) [28, 36] has been used to calculate the modified propagation constants with the impedance sheet. The propagation constants that satisfy the TRM are determined by equating the admittance looking down into the slab, and up into the air region, including the susceptance component of the impedance sheet [37].

$$Y^{air} + susceptance of Y^{sheet} = Y^{slab} \tag{2.31}$$

We can construct an equation at the boundary that is expressed in terms of the field components in both slab and air regions and the susceptance B of Y^{sheet} as shown in Fig. 2.1.

$$\frac{H_{x3}}{E_{z3}}\Big|_{y=a}^{y=\infty} + B = \frac{H_{x2}}{E_{z2}}\Big|_{y=a}^{y=0} \tag{2.32}$$

After applying the previous field components to (2.32), we obtain the propagation constants, k_2 and k_3 that include properties of the impedance sheet.

$$\frac{\omega\varepsilon_3}{k_3} = \frac{\omega\varepsilon_2}{k_2}\cot(k_2 a) - B. \tag{2.33}$$

Therefore, the modified propagation constant in the air region is derived from (2.33), and shown below.

$$k_3 = \frac{\omega\varepsilon_3}{\frac{\omega\varepsilon_2}{k_2}\cot(k_2 a) - B} \tag{2.34}$$

Substituting (2.34) into (2.22), the other constant in the slab including the susceptance is derived from an equation below.

$$k_2^2 + \left(\frac{\omega\varepsilon_3}{\frac{\omega\varepsilon_2}{k_2}\cot(k_2 a) - B}\right)^2 = \omega^2(\mu_2\varepsilon_2 - \mu_3\varepsilon_3) \tag{2.35}$$

In addition, adding the sheet generates an additional loss term due to the resistance of the sheet at the boundary $y = a$. For the sheet loss, we consider the electric fields in the z direction, parallel to the sheet.

$$\begin{aligned}\overline{P_{loss}^{sheet}} &= \frac{\frac{1}{2}\frac{1}{R_{sheet}}[E_{z2}\cdot E_{z2}^*]|_{y=a}}{2(\overline{P_{z2}} + \overline{P_{z3}})} \\ &= \frac{\frac{1}{2}\frac{1}{R_{sheet}}\left[K_z^2\frac{k_2^2}{(\omega\varepsilon_2)^2}\sin^2(k_2 a)\right]}{2(\overline{P_{z2}} + \overline{P_{z3}})}\end{aligned} \tag{2.36}$$

Therefore, the sheet loss can be linearly added to the total attenuation, α, as given below.

$$\alpha = \frac{\overline{P_{loss}^{slab}} + \overline{P_{loss}^{sheet}}}{2(\overline{P_{z2}^{slab}} + \overline{P_{z3}^{air}})} \tag{2.37}$$

By applying the TRM to calculate the modified propagation constants, we now have an expression for the attenuation which includes the properties of the impedance sheet on the top of the slab. In the case of applying an impedance boundary to the sheet, the susceptance B is given by

$$Y_{sheet} = G + jB = \frac{1}{Z_{sheet}} = \frac{1}{R + jX} \tag{2.38}$$

Table 2.1: Summary of analytical solutions

Time average propagating power in slab region	$\overline{P_{z2}^{slab}} = +K_z^2 \frac{1}{4k_2} \frac{\beta}{\omega\varepsilon_2} \left[k_2 a + \frac{1}{2} \sin(2k_2 a) \right]$	
Time average propagating power in the air region	$\overline{P_{z3}^{air}} = +K_z^2 \frac{1}{4} \frac{\varepsilon_3}{\varepsilon_2} \frac{k_2^2}{k_3^3} \frac{\beta}{\omega\varepsilon_2} \sin^2(k_2 a)$	
Time average power loss in the slab region	$\overline{P_{loss}^{slab}} = +K_z^2 \frac{\omega\varepsilon''}{4(\omega\varepsilon)^2} \left[(\beta^2 + k_2^2)a + \frac{\beta^2 - k_2^2}{2k_2} \sin(2k_2 a) \right] + K_z^2 \frac{\omega\mu''}{4} \left[\frac{1}{2k_2} \sin(2k_2 a) + a \right]$	
Impedance surface (Z_s)	Without Z_s	With Z_s
Transvers Resonance Method (TRM)		$\frac{H_{x3}}{E_{z3}}\Big\|_{y=a}^{y=\infty} + B = \frac{H_{x2}}{E_{z2}}\Big\|_{y=a}^{y=0}$
Time average power loss in the impedance sheet		$\overline{P_{loss}^{sheet}} = \frac{\frac{1}{2}\frac{1}{R_{sheet}} \left[K_z^2 \frac{k_2^2}{(\omega\varepsilon_2)^2} \sin^2(k_2 a) \right]}{2(\overline{P_{z2}} + \overline{P_{z3}})}$
Attenuation	$\alpha = \frac{\overline{P_{loss}^{slab}}}{2(\overline{P_{z2}^{slab}} + \overline{P_{z3}^{air}})}$	$\alpha = \frac{\overline{P_{loss}^{slab}} + \overline{P_{loss}^{sheet}}}{2(\overline{P_{z2}^{slab}} + \overline{P_{z3}^{air}})}$

$$\begin{aligned} G &= \frac{R}{R^2+X^2} \\ B &= -\frac{X}{R^2+X^2} \end{aligned} \tag{2.39}$$

The analytically summarized field solutions to the each region, and attenuations are listed in Table. 2.1.

We assume that the dielectric slab and ground plane provide inductance, so our analysis focuses on sheets having resistance and capacitance, and we consider both series and parallel RC circuits for the impedance sheet. In the parallel connection of resistance and capacitance, the susceptance is given by

$$\begin{aligned} Y_{sheet} &= G + jB = Y_R + Y_C \\ &= \frac{1}{R} + j\omega C \end{aligned} \tag{2.40}$$

$$\begin{aligned} G &= \frac{1}{R} \\ B &= \omega C \end{aligned} \tag{2.41}$$

In series connection between resistance and capacitance, the susceptance is given by

$$Z_{sheet} = Z_R + Z_C = R - j\frac{1}{\omega C} \tag{2.42}$$

$$Y_{sheet} = \frac{1}{Z_{sheet}} = G + jB = \frac{R}{R^2 + \left(\frac{1}{\omega C}\right)^2} + j\frac{\frac{1}{\omega C}}{R^2 + \left(\frac{1}{\omega C}\right)^2} \tag{2.43}$$

$$G = \frac{R}{R^2 + \left(\frac{1}{\omega C}\right)^2}$$
$$B = \frac{\frac{1}{\omega C}}{R^2 + \left(\frac{1}{\omega C}\right)^2} \tag{2.44}$$

Using the susceptances of (2.39), (2.41), and (2.44) under each condition, the analytical solution for attenuation is modified to include the properties of various kinds of impedance sheets.

2.3 Numerical Solution

As discussed above, analytical solutions have been developed for TM surface wave attenuation by a lossy slab and an impedance sheet. To validate the analytical solutions, we compare the results to numerical solutions. In obtaining the numerical solutions, we simulated the same structure as shown in Fig. 2.1 using Ansoft HFSS. To determine the attenuation of TM surface waves, we calculated the complex dispersion curves for TM waves using an eigenmode solver in HFSS. We also tried various approaches using a driven modal solution, but the eigenmode solution provided results that were the cleanest and easiest to interpret. We simulated a small piece (2 mm length by 10 mm width) of the slab and impedance sheet as shown in Fig. 2.2. In the x-y plane, we applied periodic boundary conditions (master and slave boundaries). We then enter a phase difference across the structure corresponding to a wave vector, and the eigenmode solver provides the corresponding frequency of that TM surface wave mode. In the y-z plane, we applied perfect H boundaries because we are simulating TM surface waves. In x-z plane, the bottom

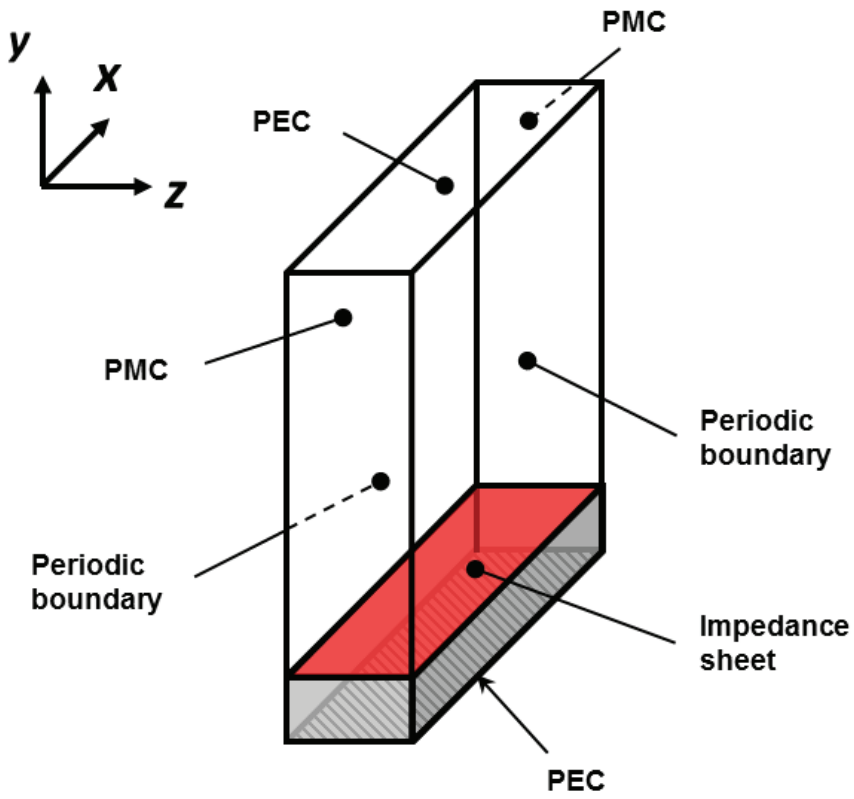

Figure 2.2: Schematic for the numerical solutions and assigned boundaries. In the $x-y$ plane, master and slave boundaries are applied, in the $y-z$ plane, perfect magnetic conductor (PMC) boundaries are applied, in the $x-z$ plane, perfect electric conductor (PEC) boundaries are applied.

and top planes are perfect E boundaries with 50 mm height between the planes including 10 mm height of the slab. At the surface of the dielectric slab, we applied an impedance sheet or lumped RLC boundary. In the slab, we used a material with relative complex permittivity and permeability. The relative complex values, $\varepsilon_r = 10 + j0.001$ and $\mu_r = 1 + j0.001$ are used in most simulations. Also, we examined a wide variety of material properties in this study. At the impedance sheet, using the lumped RLC boundary, a range of resistance and capacitance were studied. As part of the eigenmode solution, we also obtain the quality factor Q of each mode which is a function of the real and imaginary parts of frequency, ω and ω''.

$$Q = \left| \frac{\omega^{'}}{2\omega^{''}} \right| \tag{2.45}$$

This definition of Q indicates that it is a measure of how quickly the mode would decay in time if it were excited uniformly across the surface at some starting time, and then allowed to decay without additional excitation. However, what we need is the rate of decay along the surface for a wave starting at one end with continuous excitation. These two quantities are related through the group velocity of the wave, which itself is a function of frequency.

$$\alpha = \frac{\omega^{''}}{v_g} = \omega^{''} \frac{dk}{d\omega} \tag{2.46}$$

Here, k is the wave number, and ω and $\omega^{''}$ represent real and imaginary angular frequencies, respectively. The magnitude of electric field decreases along the length of the surface by $E \propto \exp^{-jkz}$. Therefore, the modified wave number can be expressed by $k = \phi/z$. Here z is the length of the structure in our simulation, and ϕ is the phase difference applied to the periodic boundary conditions in the z-direction. Substituting (2.45) and the modified wave number into (2.46) gives the equation for attenuation using calculated values in the HFSS eigenmode solver, and then we numerically differentiate to obtain

$$\alpha = \omega^{''} \frac{dk}{d\omega} = \frac{\omega^{'}}{2Q} \frac{1}{z} \frac{d\phi}{d\omega} = \frac{\omega_{n+1}}{2Q} \frac{1}{z} \frac{\phi_{n+1} - \phi_n}{\omega_{n+1} - \omega_n} \tag{2.47}$$

Where n and n+1 represent two successive simulations.

2.4 Results

2.4.1 Validation of Analytical Solution

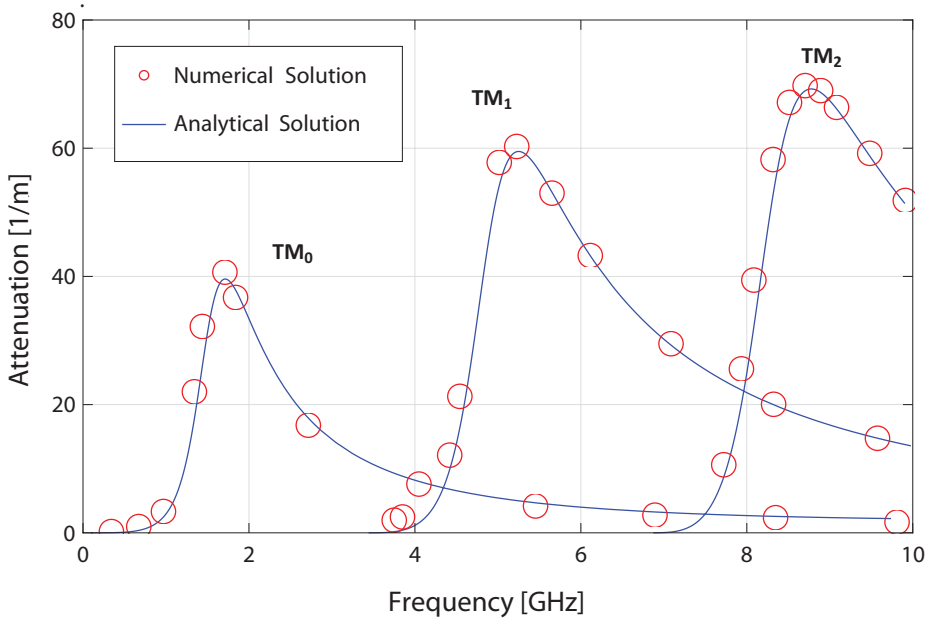

Figure 2.3: Matching plot between the analytical and numerical solutions with an impedance sheet on the slab of dielectric loss 0.001 and magnetic loss 0.001 with resistance of $377\Omega/square$ and reactance of $1\Omega/square$, respectively.

In previous sections, we discussed the analytical and numerical solutions, separately. To verify the analytical solutions, we have performed a detailed comparison with the numerical solutions from HFSS simulations. The matching plot shown in Fig. 2.3 is representative of a range of different conditions. In the plot, the impedance sheet is modeled as a series RC circuit, but we have also checked the parallel case for consistency. Multiple peaks in the plot correspond to different TM surface waves and are labeled TM_0, TM_1, etc. In the plot, the solid lines represent the analytical solutions and the dots represent the numerical solutions. Because of the close agreement between the analytical and numerical solutions for a wide range of properties for the slab and the impedance sheet, we are

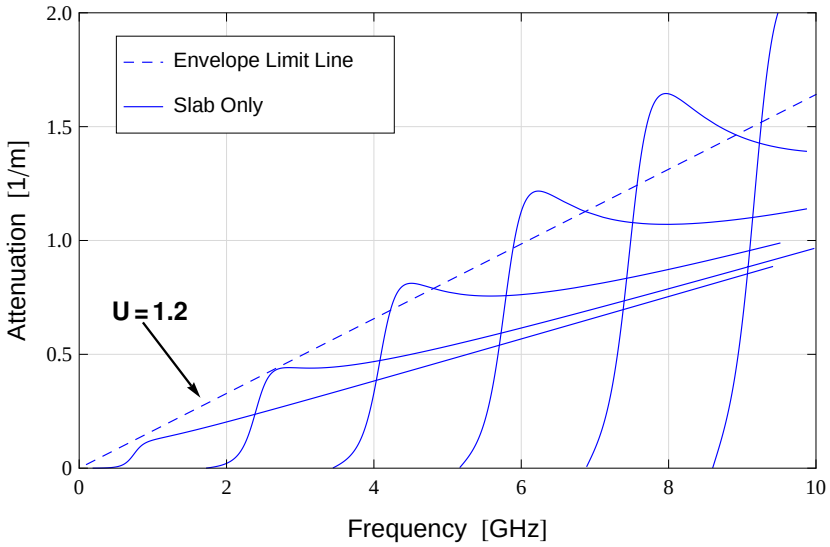

Figure 2.4: Envelope limit line for the dielectric slab without any impedance sheet. Properties of the dielectric slab are the relative permittivity 10, permeability 2, dielectric loss tangent 0.001 and magnetic loss tangent 0.001 with thickness 1 cm. The unit factor, U, of the enveloped limit line is 1.2.

convinced that the analytical solution for the attenuation is formulated correctly.

2.4.2 Theoretical Limitations

After having validated our analytical model, we now explore a wide range of material and impedance sheet properties to identify trends and limits. For the following discussion, we initially consider the case where there is no impedance sheet on the slab. In every case, we find that the attenuation shows a series of peaks corresponding to the surface wave modes, and that these peaks form an envelope that can be approximated by a linear function that is consistent over a wide range of material properties. An example is shown in Fig. 2.4. We designated the line as the *'envelope limit line'* which is given by

$$\alpha \cong U \cdot f \cdot \varepsilon_2 \cdot \mu_2 \cdot \tan\delta \tag{2.48}$$

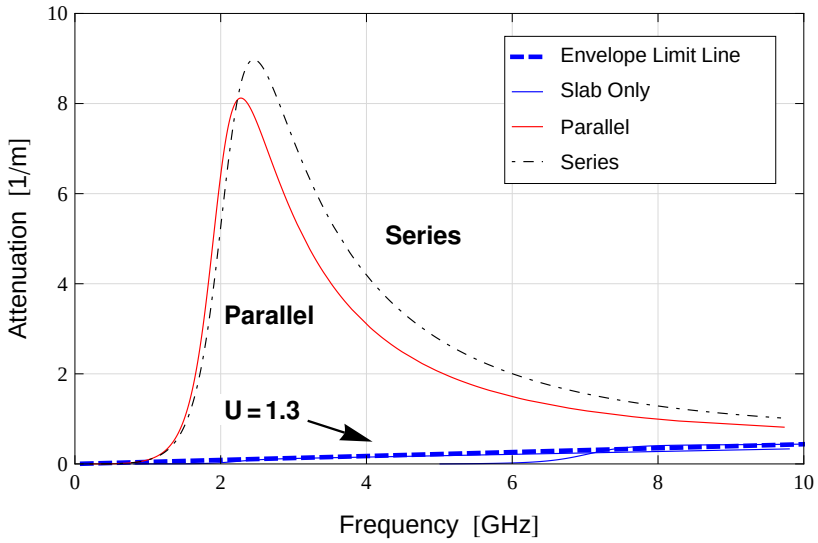

Figure 2.5: Comparison of attenuation values when adding an impedance sheet to the dielectric slab: the dashed line shows the envelope limit line with $U = 1.3$. the solid and the dot dashed lines show parallel and series impedance sheets, respectively, with resistance of $1000\Omega/square$ and capacitance of $0.1\ pF/square$. Note that we have only plotted the first of a series of attenuation peaks.

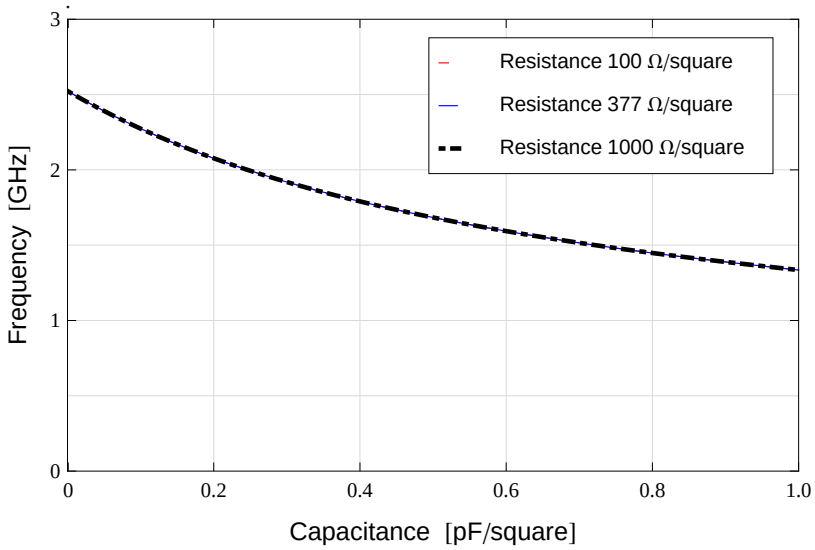

Figure 2.6: Peak frequency as a function of the capacitance of an impedance sheet in parallel connection of resistance and capacitance values. The dot dashed line, dashed line, and solid line represent different sheet resistances of 100, 377 and $1000\Omega/square$, respectively.

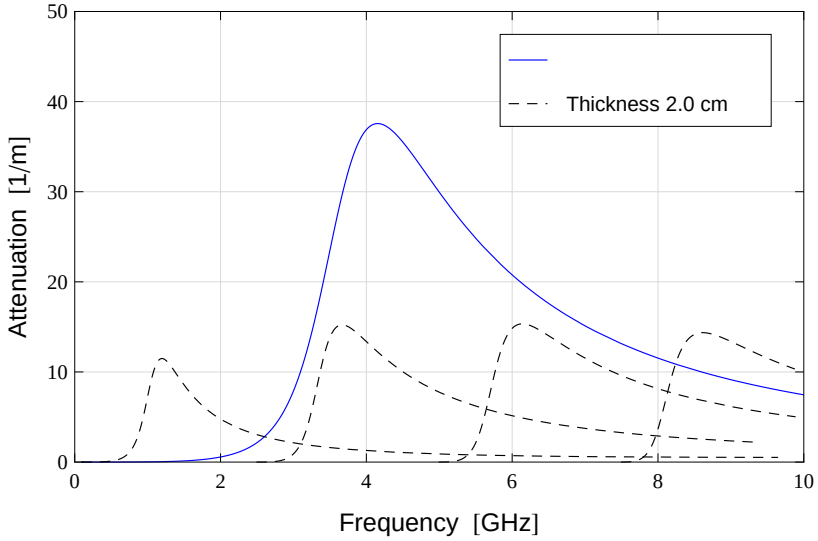

Figure 2.7: Attenuation value for different thickness of the slab with an impedance sheet having resistance of $377\Omega/square$ and capacitance of $0.1\ pF/square$. The thicknesses of the slab are 0.5 and 2.0 cm, respectively.

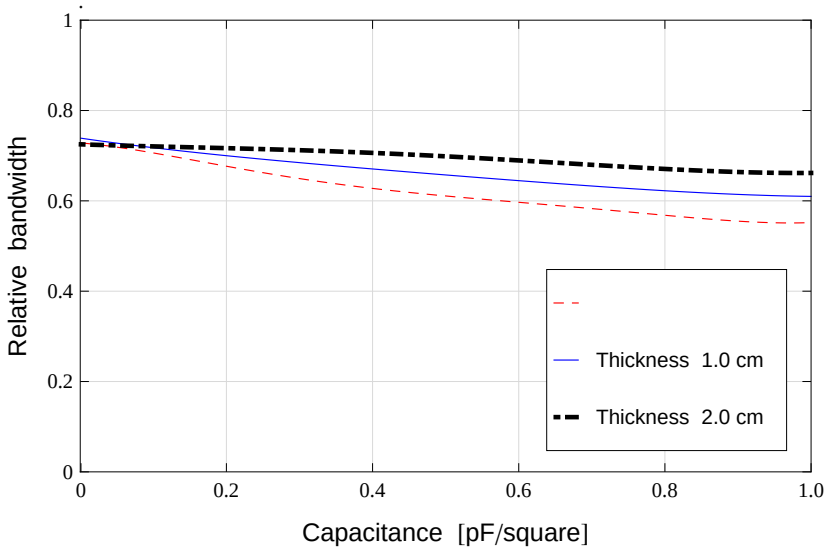

Figure 2.8: Relative bandwidth for different thicknesses of the slab as a function of capacitance. This is for an impedance sheet represented by a parallel RC circuit.

$$\tan\delta = \frac{\mu_2\varepsilon_2'' + \mu_2''\varepsilon_2}{\mu_2\varepsilon_2 - \mu_2''\varepsilon_2''} \tag{2.49}$$

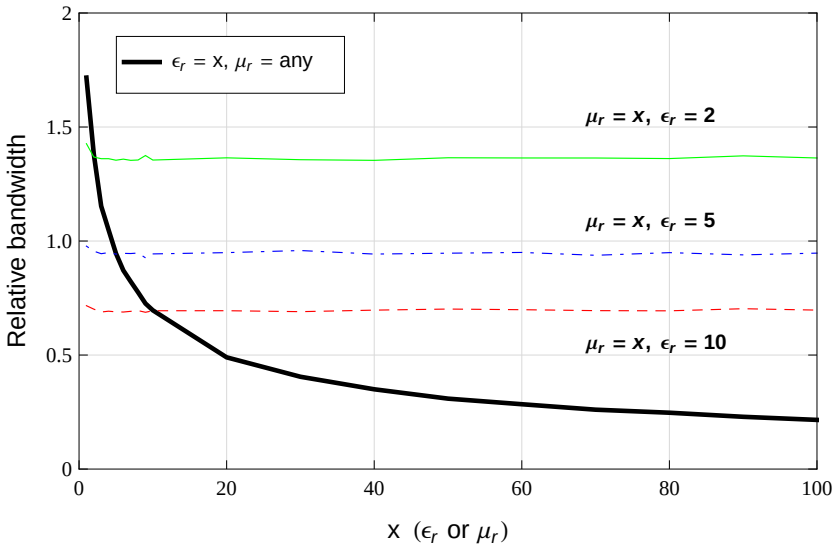

Figure 2.9: Relative bandwidth for different slab properties as a function of relative permittivity or permeability up to 100. The solid, dot dashed and dashed lines are for swept relative permeability with the fixed permittivity of 2, 5 and 10. The thick solid line represents a swept relative permittivity with a permeability of 10.

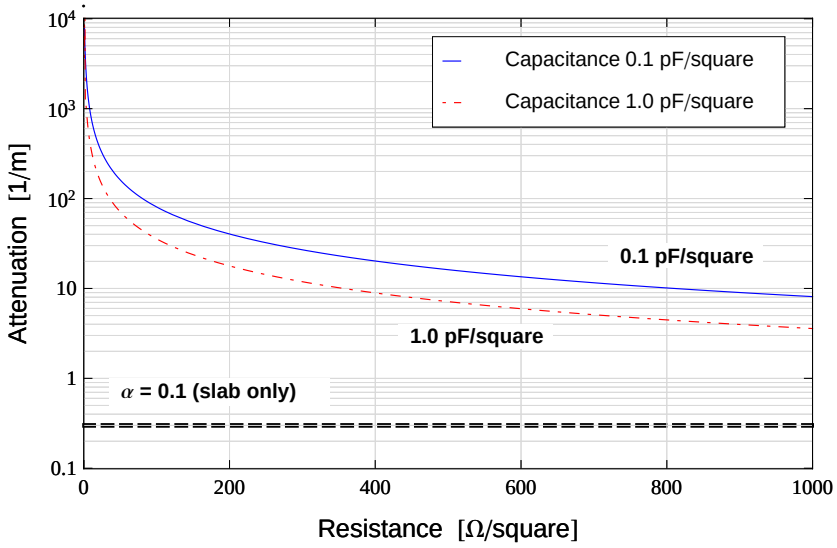

Figure 2.10: Peak attenuation values as a function of resistance of the impedance sheet, which is represented by a parallel RC circuit. The solid and dot dashed lines represent different capacitances, 0.1 and 1.0 $pF/square$, respectively. The dashed line represents the envelope limit line for the slab alone.

Here, f and c represent frequency and speed of light in free space, and loss tangent, $\tan\delta$ expressed in (2.49) [38], represents the combined dielectric and magnetic loss properties. In (2.48), there is a factor, U, which has a value that is approximately unity for a wide range of material properties, and can be considered to be unity as a simple guideline for estimating attenuation.

Even under a broad range of loss tangents from 0.001 to 1.0, U is still within this range. When the slab is electrically thick, the attenuation deviates from (2.48), but only by a small amount. Thus, (2.48) provides a valuable guideline for estimating attenuation. It is noteworthy that the thickness does not affect the slope of the envelope limit line, although the thickness does determine the frequency of the first mode, and the frequency spacing of the modes.

If an impedance sheet is added to the slab, the attenuation can be substantially greater than the envelope limit line as shown in Fig. 2.5, but over limited bandwidth. The peak frequency is determined by the capacitance of the sheet and thickness of the slab, as shown in Fig. 2.6 and 2.7, while the maximum attenuation value is determined by the resistance of the sheet, and the thickness and loss parameters of the slab. Increasing the slab thickness reduces the peak frequency, but also reduces the absolute bandwidth of the peak, as shown in Fig. 2.7, as measured by the full width at half maximum (FWHM).

Thus, the relative bandwidth, as determined by the absolute bandwidth at the FWHM divided by the peak frequency, is essentially independent of the slab thickness and the properties of the sheet, as shown in Fig. 2.8. The permeability and permittivity of the slab affect the relative bandwidth in different ways, as shown in Fig. 2.9.

Increasing either of these parameters will reduce the peak absorption frequency. However, increasing permeability does so without affecting the relative bandwidth, which

increasing permittivity substantially reduces relative bandwidth. This is consistent with previous studies of absorption of normally incident waves [33], where permeability has a beneficial effect on bandwidth, but permittivity does not.

Although the resistance of the sheet does not significantly affect the peak frequency or bandwidth, it does affect the maximum attenuation value. The attenuation values of the peak of the first curve are related to the resistance of the impedance sheet as shown in Fig. 2.10. In the plot, the value of the attenuation decreases with increasing resistance. Additionally, the curves for the attenuation values with the impedance sheet are compared to a dashed straight line corresponding to the envelope limit line of the slab only. Thus, the impedance sheet can enhance the attenuation compared to the slab alone, but at the expense of bandwidth.

2.5 Conclusion

We have developed an analytical model for TM surface wave attenuation by grounded lossy slabs including both dielectric and magnetic losses. Using the transverse resonance method we have extended the solution to include an impedance sheet which may represent a FSS, metasurface or other periodic structure. We find that for the case of the bare slab, the attenuation can be approximated by a simple formula for a wide range of material properties. By making practical assumptions about available materials, this formula can be used to estimate the limits on absorption for homogeneous linear lossy slabs. We have also found that the use of an impedance sheet can provide substantially greater attenuation than what is possible with a simple lossy slab, but with limited bandwidth. For an impedance sheet that can be described in terms of effective sheet capacitance and sheet resistance, the capacitance and the slab thickness primarily determine the frequency of the attenuation peak,

and the resistance determines the maximum value of attenuation. Although the absolute bandwidth is determined by both the capacitance of the sheet and the thickness of the slab, the relative bandwidth is nearly independent of all of these parameters. Furthermore, increasing permittivity to reduce the peak absorption frequency also reduces relative bandwidth, whereas increasing permeability does not. These results can be used as a guideline for the development of broadband or narrowband coatings for attenuation of TM surface waves.

Chapter 2 is based on and is mostly a reprint of the following paper: **S. Kim**, D. Sievenpiper, "Theoretical Limitations for TM Surface Wave Attenuation by Lossy Coatings on Conductive Surfaces", *IEEE Transactions on Antennas and Propagation*, vol. **62**, no.1, pp.475-480, January 2014. The dissertation author was the primary author of the work in this chapter, and the co-author has approved the use of the material for this dissertation.

Chapter 3

Switchable Nonlinear Metasurfaces for Absorbing High Power Surface Waves

In this chapter, a new concept of a nonlinear metamaterial surface is introduced, which provides power dependent absorption of incident surface waves. The metasurface includes nonlinear circuits which transform it from a low loss to high loss state when illuminated with high power waves. The proposed surface allows low power signals to propagate but strongly absorbs high power signals. It can potentially be used on enclosures for electric devices to protect against damage. We experimentally verify that the nonlinear metasurface has two distinct states controlled by the incoming signal power. We also demonstrate that it inhibits the propagation of large signals and dramatically decreases the field that is leaked through an opening in a conductive enclosure.

3.1 Overview of Concept

The high power surface currents are capable of leaking inside through gaps or openings in the conductive shielding. Even if an aperture is electrically small, it can effectively behave as a slot antenna that can allow radiation inside. Conventional approaches [39, 40] to inhibit such destructive interference include applying a lossy coating on the outer surface of the metallic shielding. Another method is to use a resonant absorber such as a Salisbury screen [41], Jaumann absorber [42], or metamaterial absorber [8, 43, 44, 45] to absorb incoming waves. Such conventional approaches based on linear materials absorb low power and high power signals equally. Thus, they can reduce the performance of antennas located on the surface, and can affect the operation of a low power communication system. Moreover, surface currents are not entirely suppressed, and absorbing coatings can be characterized by their attenuation rate which depends on the thickness and the materials that make up the absorber [46]. One advantage of a nonlinear absorber is that it can decouple the attenuation of potentially damaging high power signals from the attenuation of low power signals that are needed for communication.

Here, we introduce the concept of a switchable metamaterial absorber based on nonlinear circuits integrated into a high impedance surface [6]. These surfaces are electrically thin, typically $\leq \lambda/10$ where λ is the free space wavelength.

Nonlinear metasurfaces which respond to the waveform and power of the incoming wave have previously been demonstrated [47, 48, 49]. Compared to prior works, this structure provides high power absorption regardless of the incoming waveform using a much simpler circuit, requiring only a single diode per cell, and no reactive components. Furthermore, we demonstrate nonlinear attenuation of surface waves over a large area, and suppressed leakage of high power signals through a narrow gap by surrounding it with a

nonlinear coating. We demonstrate this nonlinear absorber through electromagnetic/circuit co-simulation, validated by measurements of small samples inside waveguides, followed by large-area field measurements, and finally a measurement of the reduction of electromagnetic fields entering an enclosure. Our measurements show surface wave attenuation that exceeds that of a conventional linear absorber, and the use of such a surface for practical applications.

3.2 Mechanism of Switchable Metasurface

The main mechanism of the switchable metasurface is that a metallic structure embedded with nonlinear devices such as diodes will change its conductive topology, and thus its absorbing properties, as a function of the incident power level. The structure shown in Fig. 3.1 (a) is based on the high impedance surface [6], which consists of conductive patches connected to a ground plane by vertical conducting vias. A pair of diodes is located at each vertical via, and a network of resistors is interconnected between the patches. Because of the nonlinear diodes, the metasurface transforms from one state to another depending on the power level, shown as the insets to Fig. 3.1 (a). In other words, the diagram of the metasurface with two distinct states defined by a threshold power. Insets (Fig. 3.1 (a)) of dispersion diagrams for the off- and on-states. In order to facilitate fabrication, we used a planar geometry, in which the top patches of the metasurface are each composed of an outer ring and an inner patch connected with a via. Two diodes are connected in opposite polarity between the ring and the inner patch so that the surface will respond to both positive and negative portions of the RF cycle.

Surface waves generate currents in the patches, as well as voltages between the patches and the ground plane. At low power, the diodes appear as an open circuit. However, when the voltage exceeds the turn-on voltage of the diodes, they behave as a short circuit,

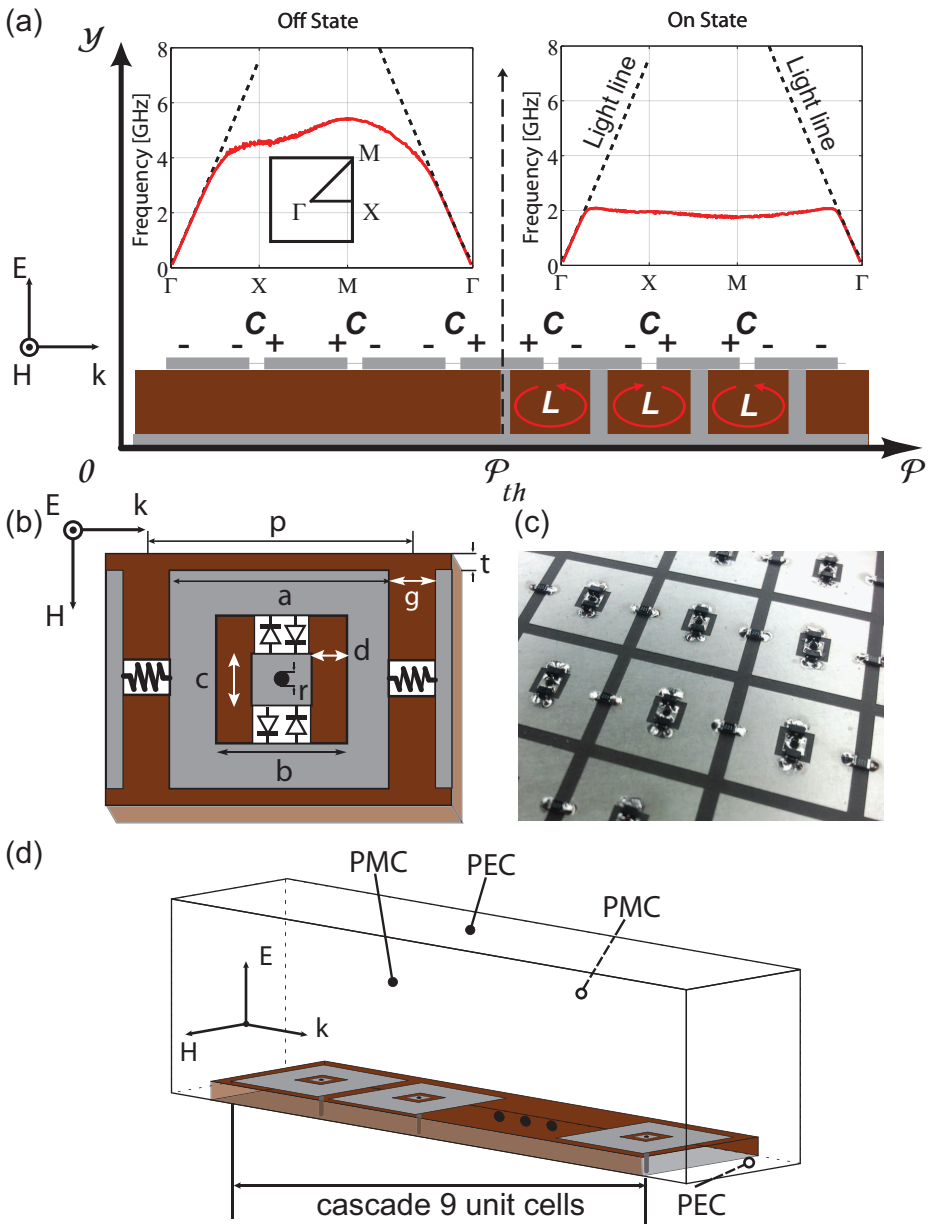

Figure 3.1: Nonlinear metasurfaces for power dependent absorption: (a) Diagram of the metasurface with two distinct states defined by a threshold power. Insets of dispersion diagrams for the off- and on-states. (b) Geometry of the unit cell $p = 17$, $t = 3.175$, $g = 2$, $a = 15$, $b = 4.49$, $c = 2.762$, $d = 0.864$, and $r = 1.0$ (all in mm). (c) A photograph of the sample with circuit components attached. (d) A simulation model with a cascade of nine unit cells in a row with perfect magnetic conducting (PMC) walls to simulate a 2-D array.

connecting the patches to the ground plane. In this state, the surface behaves as an artificial magnetic conductor, with an inductive current path (L) through the vias and a capacitance

(C) defined by the gaps between the patches. The LC resonance of the structure creates high surface impedance [6], and the dispersion curve bends over to become flat, shown as the inset of the *on-state* in Fig. 3.1 (a). Near the LC resonance frequency of around 2 GHz, the surface waves are highly confined to the surface and interact strongly with the metallic structure. Near the band edge, the surface waves are also strongly absorbed by the resistors that are connected between the patches. In contrast, if the voltage on the patches does not exceed the turn-on voltage of the diodes, the surface appears as a simple capacitive sheet on a grounded dielectric substrate, and losses in the resistors are not significantly enhanced without the LC resonance.

The nonlinear metasurface is implemented as shown in Fig. 3.1 (b). Geometry of the unit cell is shown: $p = 17$, $t = 3.175$, $g = 2$, $a = 15$, $b = 4.49$, $c = 2.762$, $d = 0.864$, and $r = 1.0$ (all in mm). Periodic conductive patterns are printed on a Rogers 5870 substrate with a 3.175 mm thickness and with a 17 mm period as shown in Fig. 3.1 (c). Eigenmode simulations of a single unit cell provide the band diagrams for the *off-* and *on-states* shown in the insets of Fig. 3.1 (a). EM/circuit co-simulation of a periodic array of cells was used to determine the absorption properties. A pair of Schottky diodes packaged together (Avago HSMS-286C with parasitic of a series resistance 6 Ω, lead frame inductance 0.2 nH, coupling capacitance 0.035 pF, bond wire inductance 0.7 nH, package capacitance 0.03 pF, and lead frame capacitance 0.01.) was attached at each via, and 220 Ω resistors were attached between the patches. In these simulations, a row of 9 unit cells was simulated inside a transverse electromagnetic (TEM) waveguide constructed with perfect electric conducting (PEC) and perfect magnetic conducting (PMC) boundaries on opposing walls of the guide as shown in Fig. 3.1 (d). The TEM waveguide measured 17 mm wide to fit one unit cell, and 54.6 mm in height.

3.3 Measurement of Nonlinear Metasurface

3.3.1 Linear Measurement in Waveguides

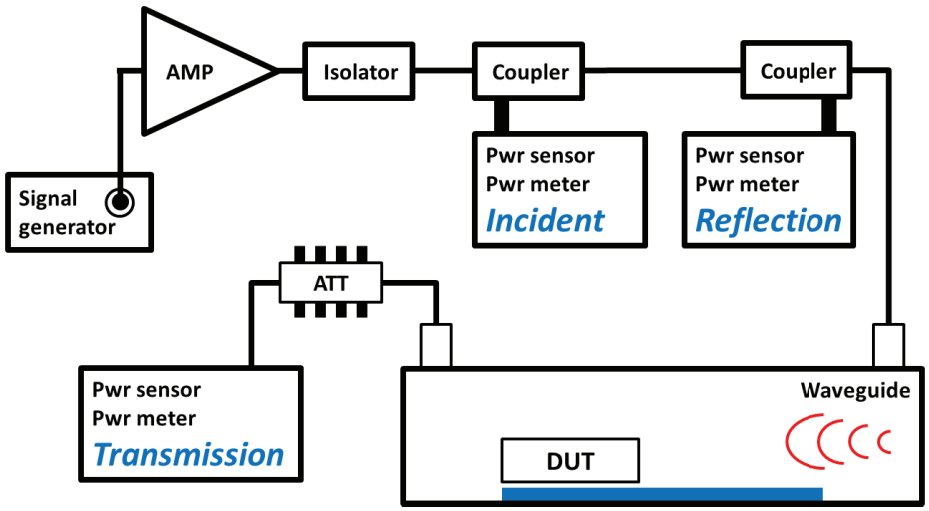

Figure 3.2: Measurement setup for linear waveguide measurement.

The measurement samples were fabricated with the same geometry as the simulation model, except with a sufficient number of lateral cells to fit within a standard rectangular metal TE waveguide. Two separate waveguide sizes (WR284 and WR430) were required to cover the frequency range from 1.7 to 4 GHz. The resulting sample sizes were 4 x 9 cells, and 6 x 9 cells. Transmission and reflection were measured using power meters (Agilent N1911A) with high power signals provided by RF amplifiers (Ophir 5022 and 5193). Note that although TEM waveguide was used in the simulation, and TE waveguide was used in the measurement, both have similar electric and magnetic field profiles, and can be expected to identify similar performance trends [47, 48]. TEM waveguide allows a much simpler simulation, but the required boundary conditions are not available for experiments. The measurement setup under the linear waveguides is shown in Fig. 3.2. The metasurface is located at the bottom of the waveguide, and the incident wave propagates from the input

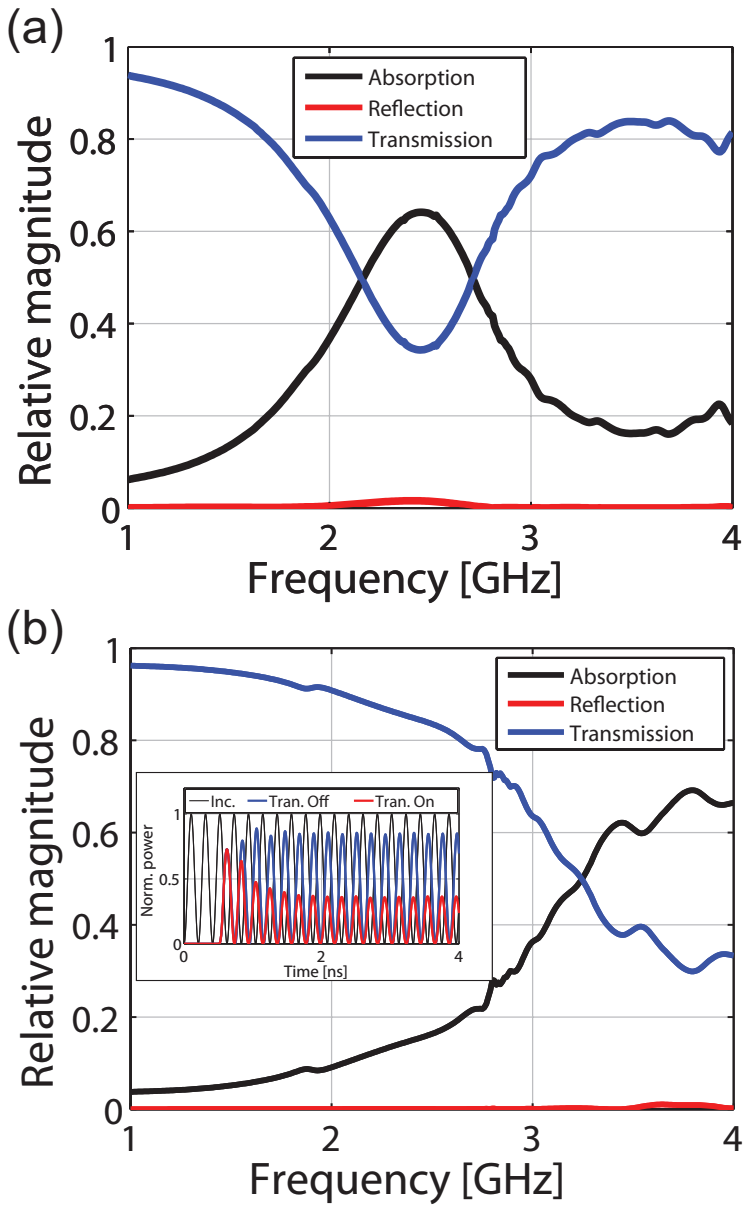

Figure 3.3: Transient simulation data, absorption (black line), reflection (red line), and transmission (blue line), are shown for (a) on-state and (b) off-state. Inset to (b) shows the comparison of normalized transmitted powers in the time domain.

port of the waveguide. The input signals are generated by the signal generator and amplified to the high power microwaves.

The simulation and measurement results are shown in Fig. 3.3 and 3.4, respectively. Absorption was calculated as $A(\omega) = 1 - T(\omega) - R(\omega)$ ($A(\omega)$: absorption, $T(\omega)$: transmission,

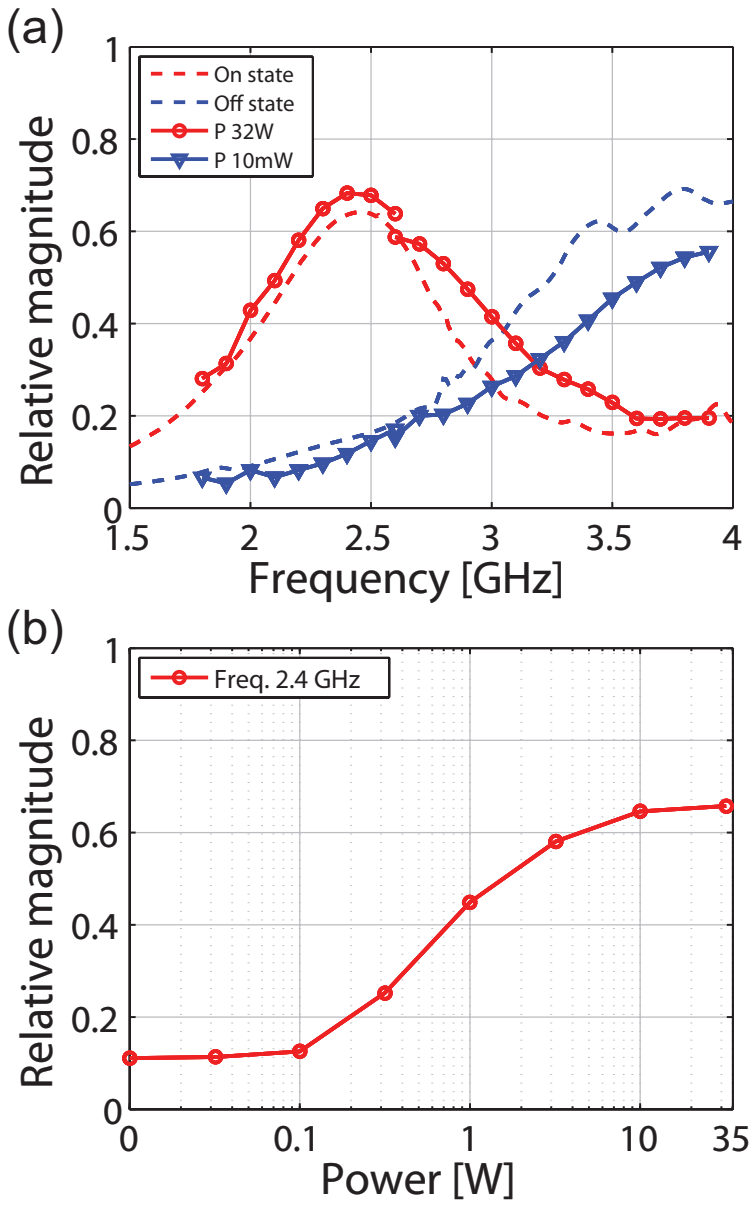

Figure 3.4: Simulation and measurement of the nonlinear metasurface inside the waveguides. The surface demonstrates two distinct states for low and high power conditions. (a) Dashed and solid dotted lines represent transient simulation and measurement data, respectively. (b) Absorption at 2.4 GHz versus incoming power levels.

and R(ω): reflection with frequency dependence (ω)). Note that reflection is negligible in all cases. Additionally, parasitic parameters of the circuit components (specifically in the diodes) contribute to a small frequency shift, so the parasitic values of the circuit components

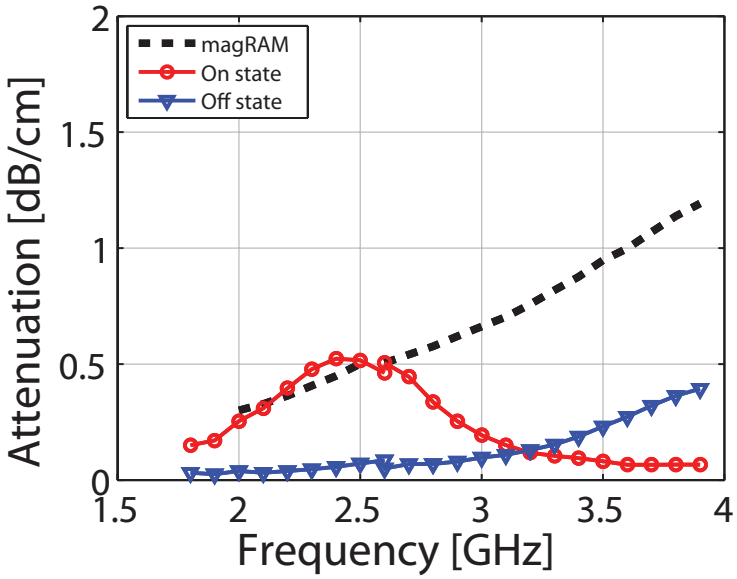

Figure 3.5: Comparison of the absorbing profiles with a typical magRAM.

were also considered in the simulations. At the design frequency of 2.4 GHz, the lower power absorption is about 10 %. With increasing power, the surface becomes resonant at 2.4 GHz, and the absorption increases to a maximum of 70 % as shown in Fig. 3.4 (a). The surface demonstrates two distinct states for low and high power conditions. In Fig. 3.4(a) dashed and solid dotted lines represent transient simulation and measurement data, respectively. The full width at half maximum (FWHM) absorptivity of the metasurface for on-state is 1.05 GHz from 1.95 to 3.1 GHz at the center frequency. The attenuation rate at 2.4 GHz is shown in Fig. 3.4 (b) as a function of the incident power level. Below 100 mW, the surface is in the off-state. Above 10 W, the attenuation rate is saturated at 2.4 GHz versus incoming power levels.

In Fig. 3.5, we convert the attenuation rate to dB/cm, and also compare the measured performance to that of magRAM (SRC Tech. DD-11006) of the same thickness as the metamaterial surface. The magRAM has a broad absorption band, whereas the metamaterial surface absorbs primarily near its resonance frequency. The metamaterial has a maximum

absorption rate that is approximately equal to that of the magRAM in the waveguide measurement. However, it performs better in measurements of surface waves on open surfaces, as discussed in the next sections.

3.3.2 Surface Wave Measurement

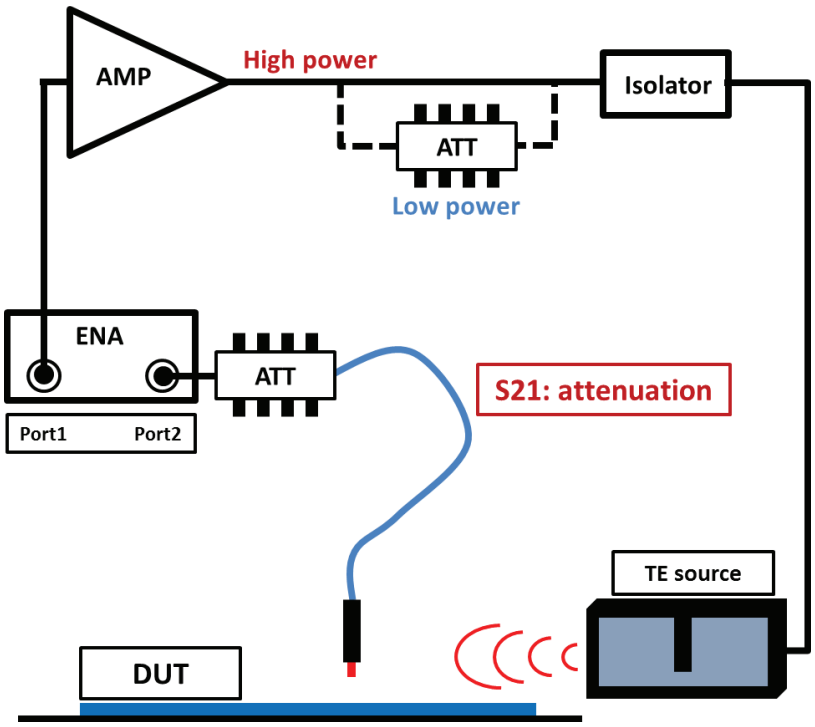

Figure 3.6: Measurement setup for surface field suppression.

To study the effect of surface waves in an open environment, we constructed a large area of the nonlinear metasurface, measuring 391 mm by 527 mm, and 23 x 31 unit cells. The measurement environment is shown in Fig. 3.6. Fig. 3.7 shows the geometry of the measurement, as well as low and high power field plots for the nonlinear metasurface. We also measured the field profile on standard magnetic radar absorbing material, magRAM (SRC Tech. DD-11006) of the same thickness. We excited surface waves by launching them from an open-ended waveguide placed adjacent to one edge of the surface. The measurement

setup with planar near field scanner, network analyzer (Agilent E5071C), and amplifier. A wave is launched near the center left edge of the surface. The surface was placed in our near-field scanner, which consists of two linear position controllers arranged to provide x-y scanning over a 1 square meter area shown in Fig. 3.7 (b).

We scanned a small coaxial probe over an area 2 mm above the surface to measure the electric field as a function of position for various power levels shown in Fig. 3.7 (c)-(f). The power levels of each figure are in Fig. 3.7 (c) metasurface at 4.8 mW, Fig. 3.7 (d) metasurface at 34 W, Fig. 3.7 (e) magRAM at 4.8 mW, and Fig. 3.7 (f) magRAM at 34 W, respectively. The waveguide excites a surface wave that spreads out over the surface, and is also attenuated by losses in the surface. As the power level is increased, the nonlinear metasurface shows increasing absorption, seen as reduced relative field strength from Fig. 3.7 (c) to Fig. 3.7 (d). A transition to the highly absorbing state occurs at approximately 10 W of input power, although the two plots represent two extremes of a continuous variation in absorption. The magRAM shows the same field profile for low and high field strength in Fig. 3.7 (e) and Fig. 3.7 (f), respectively. This is expected because it is a linear absorber. Unfortunately, it was not possible to extract the attenuation rate from these data because the reduction in field strength occurs due to both diffraction from the source, and also attenuation, with different regions of the surface having different attenuation rates. The surface field transitions of the metasurface and magRAM under off- and on-states depending on the input powers are shown in Fig. 3.8, 3.9, 3.10, and 3.11, respectively.

3.3.3 Leakage Field Measurement

In order to demonstrate the use of our nonlinear metasurface in a practical application, we constructed a metallic box with a narrow opening shown in Fig. 3.12 (a). This would

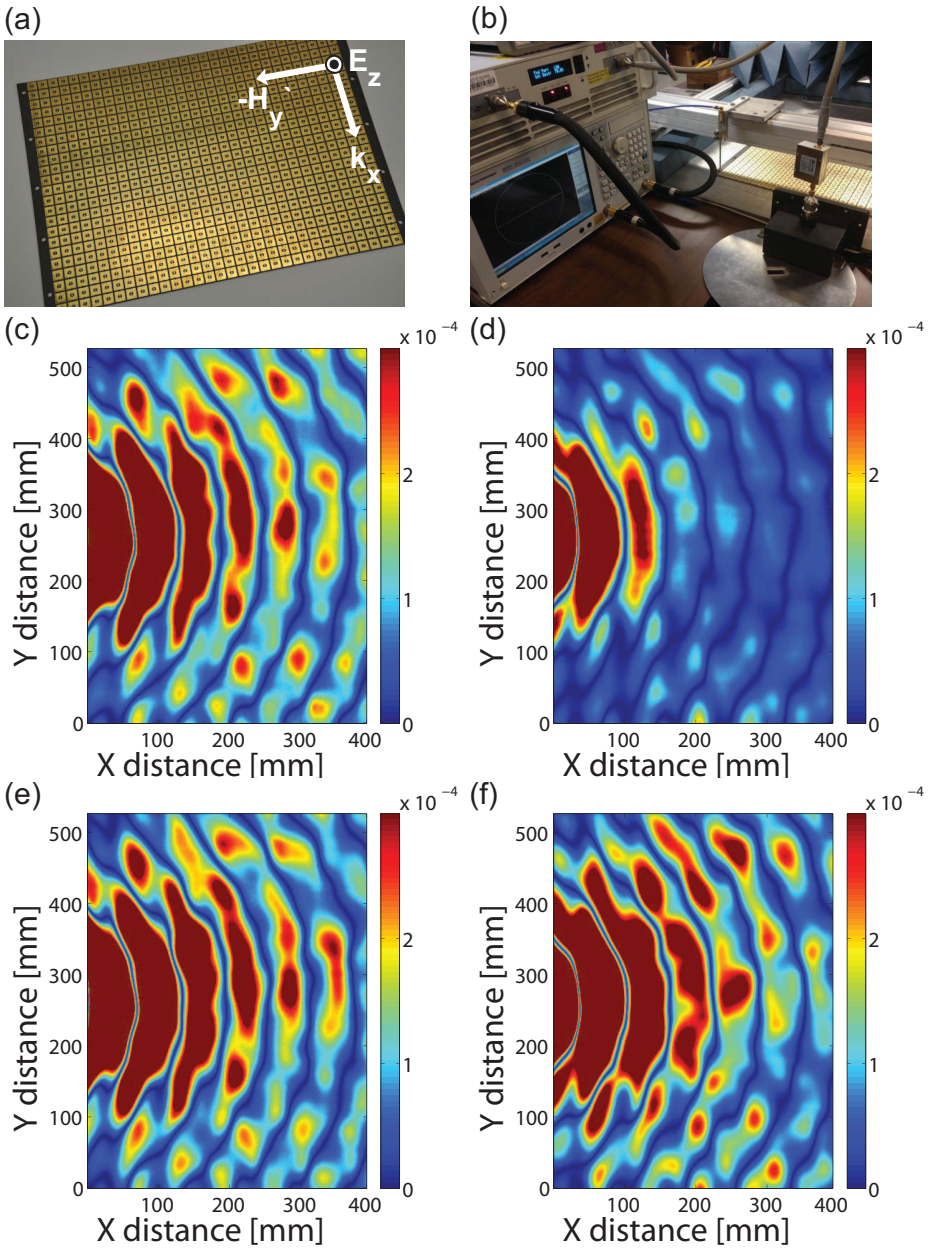

Figure 3.7: Measurement of the surface field profiles under different power levels. (a) A large nonlinear metasurface, 391 x 527 (in mm). (b) The measurement setup with planar near field scanner, network analyzer (Agilent E5071C), and amplifier. A wave is launched near the center left edge of the surface. (c) Metasurface at 4.8 mW, (d) metasurface at 34 W, (e) magRAM at 4.8 mW, and (f) magRAM at 34 W.

represent, for example, a piece of sensitive electronic equipment, a metallic shell of a vehicle, or some other conductive enclosure. Our assumption is that the enclosure may

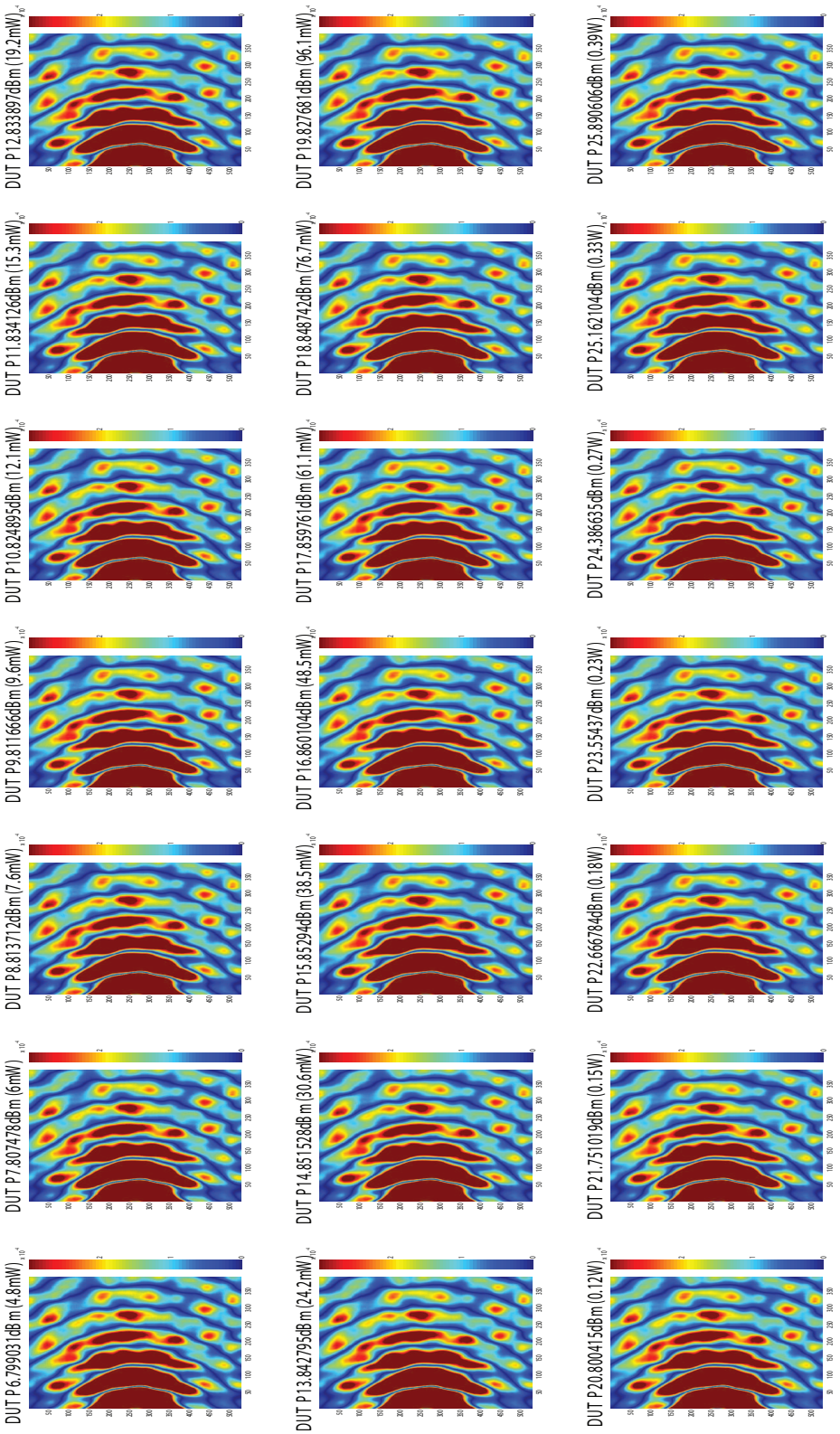

Figure 3.8: Off-State surface field profiles of the metasurface

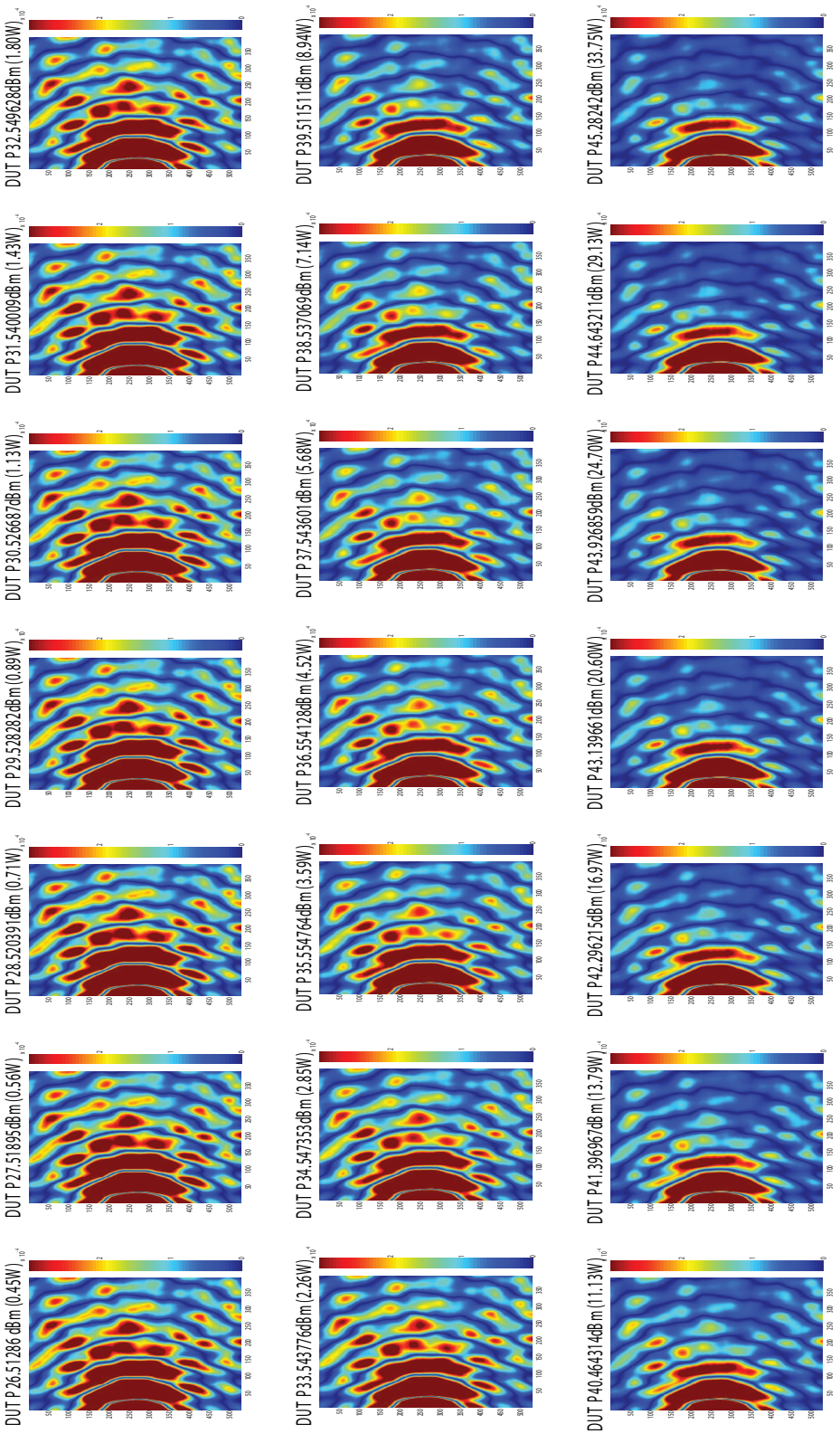

Figure 3.9: On-State surface field profiles of the metasurface

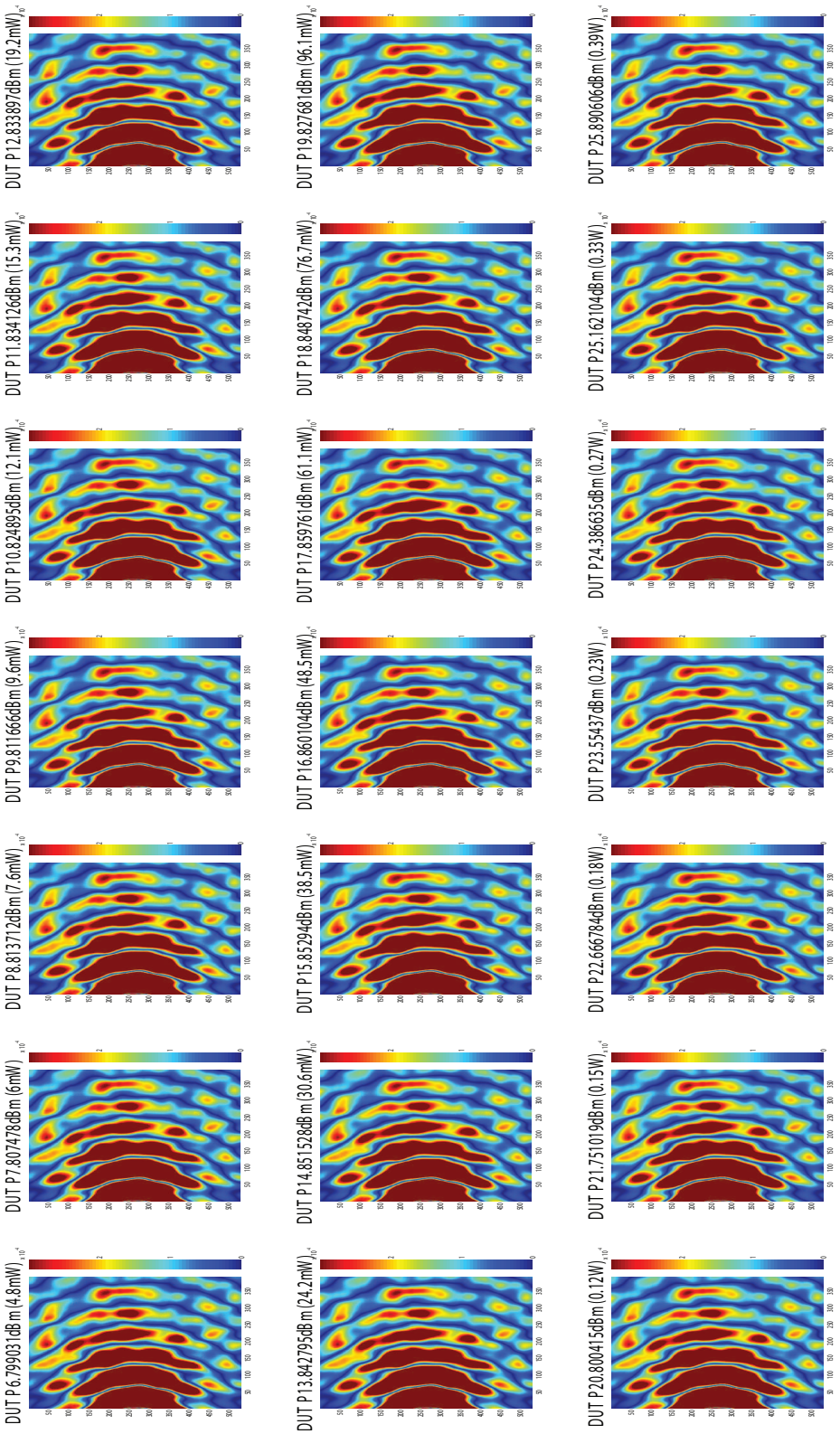

Figure 3.10: Off-State surface field profiles of the magRAM

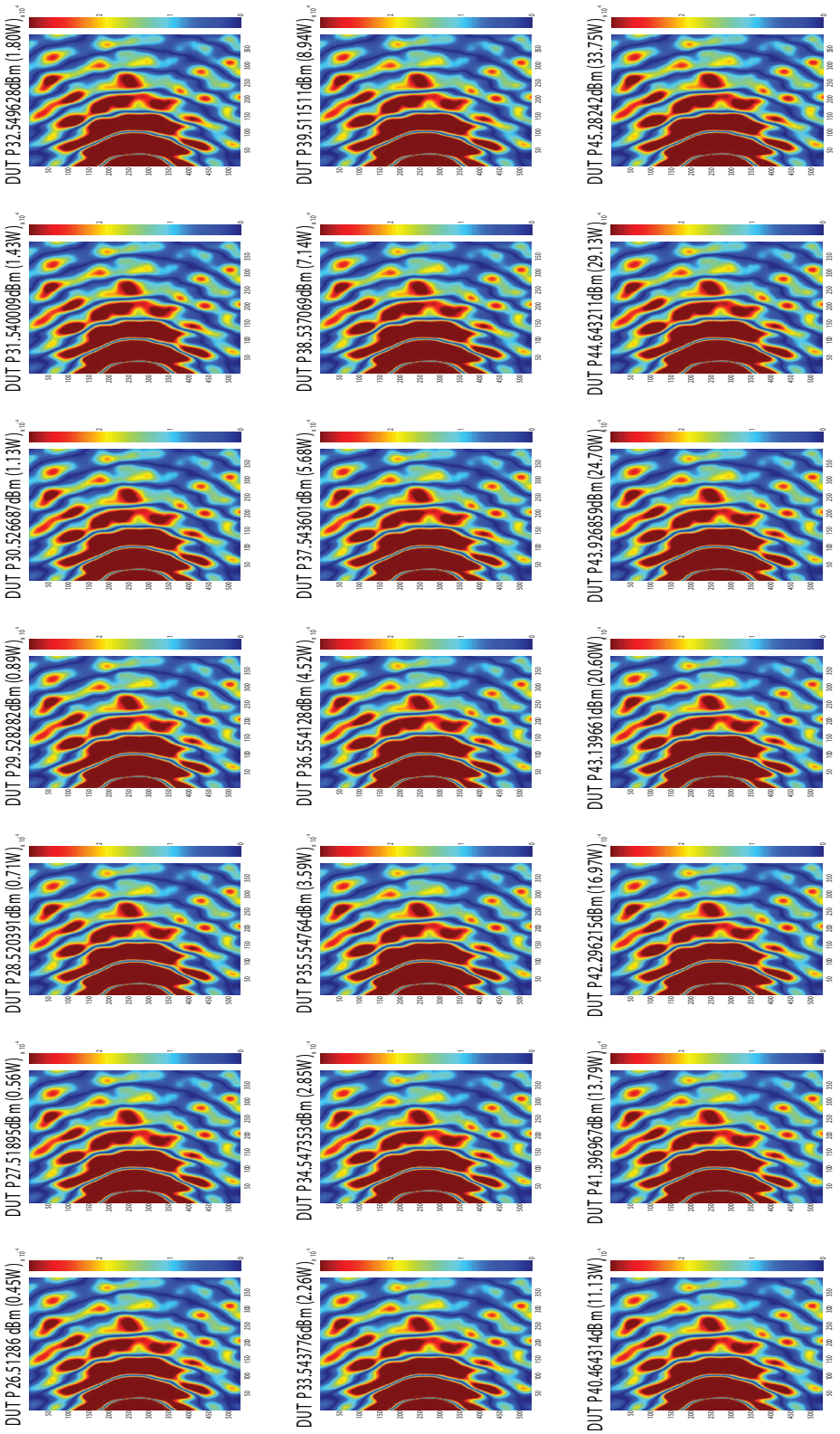

Figure 3.11: On-State surface field profiles of the magRAM

not be perfectly sealed, and external fields can leak in through small gaps, seams, or other openings. By covering the area around the gaps with a nonlinear absorber, one can limit the field level that is allowed to penetrate the box. For the following experiments, the box measured 560 x 910 x 100 (in mm), and a 9 mm wide opening was located on one face. We developed an experimental approach to measure the field leakage into the enclosure through the narrow opening and determined the effect of the nonlinear metasurface coating compared to a conventional magRAM coating as well as a bare metal surface. The metal box was placed in an anechoic chamber, and illuminated by 2.4 GHz waves from a horn antenna located on one wall of the chamber, 2.5 m away from the box as shown in Fig. 3.12 (b). The signals from the network analyzer were amplified to as much as 150 W by a high power amplifier (Ophir 5265) and they impinged upon the box at a grazing angle relative to the face which contained the opening. The waves were vertically polarized relative to the top surface, and propagated perpendicular to the gap in that surface. We used this geometry in order to efficiently excite transverse magnetic surface waves which could penetrate the gap.

We placed a small electric field probe inside the box below the opening, and measured the field strength inside the box for various surface coatings. The field probe was calibrated by placing it at the same location without the box, and using the Friis transmission equation. The field level inside the box is shown in Fig. 3.12 (c) as a function of the impinging field strength for the nonlinear metasurface coating, compared to the conventional magRAM coating, and to the bare metal surface. For both the metal surface and the magRAM, the field strength inside the box is a linear function of the external field strength, as expected because these are both linear materials. The magRAM shows a reduction in internal field strength relative to the bare metal case because of its absorption. However, the metasurface

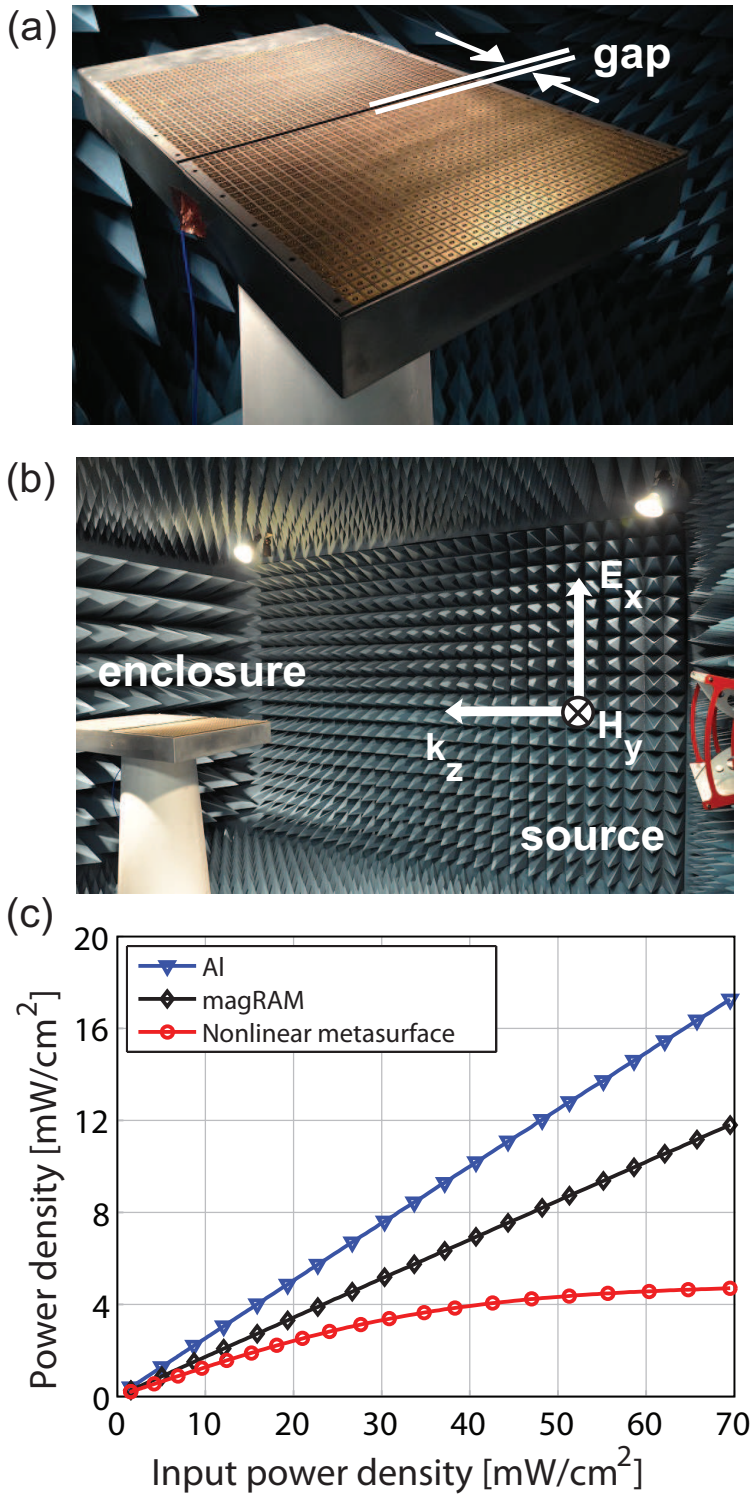

Figure 3.12: (a) The metal enclosure with a gap in one face, surrounded by the nonlinear metasurface and compared to conventional magRAM and bare metal. (b) The measurement setup inside the anechoic chamber. (c) The field inside the enclosure as a function of the impinging field strength. The nonlinear metasurface demonstrates a saturation effect, limiting the field leakage into the enclosure.

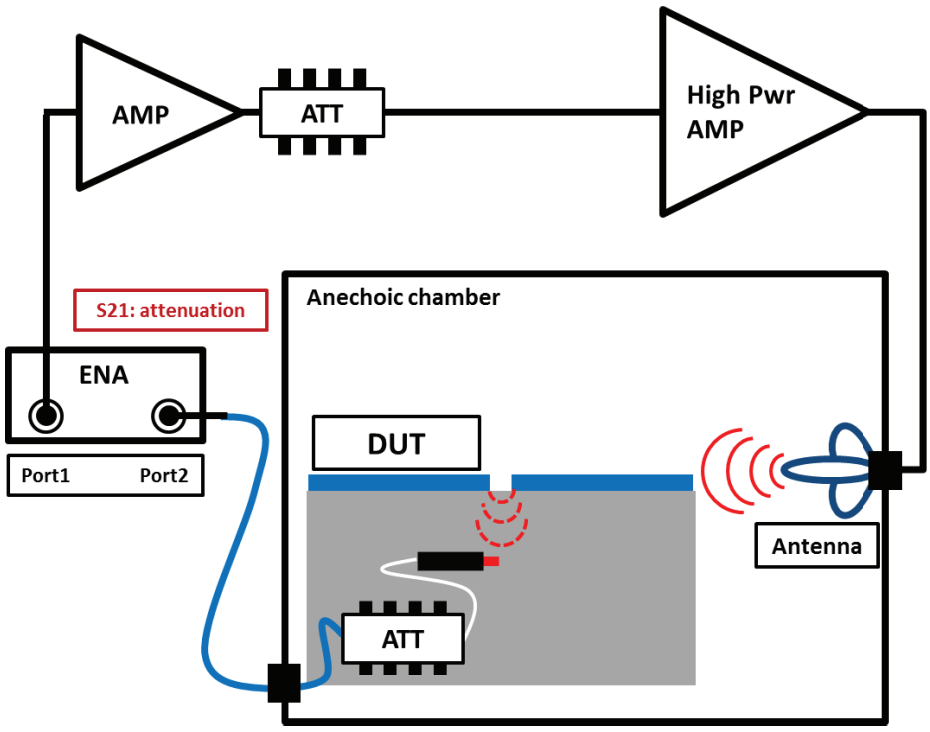

Figure 3.13: Measurement setup for leakage fields through the conductive enclosure.

shows nonlinear absorption, and exhibits a saturation effect whereby the field inside the box is limited to roughly 4 mW/cm^2, regardless of the external field strength. Note also that the nonlinear metasurface coating provides substantially greater suppression of leakage than the magRAM coating, and its advantage increases with higher signal levels. The brief measurement scheme is shown in Fig. 3.13.

We also measured the signal strength for various gap sizes, and for various probe positions inside the enclosure. In general, larger gaps allowed greater leakage for all three surfaces, as expected. Also, the field strength varied with a position inside the box due to standing waves formed in the metal cavity, and it was generally reduced toward the back wall of the metal box. These variations may be reduced in future measurements by designing the box to be a single mode cavity at the frequency of interest. Nonetheless, the plot in Fig. 3.12 (c) is representative of the trends seen in all cases, and we can conclude that the

nonlinear metasurface coating provides not only an absorption advantage at its resonant frequency relative to a conventional magRAM, but also a nonlinear saturation effect, limiting the field penetration through a gap in a metal enclosure.

3.4 Conclusion

In this chapter, we have demonstrated a kind of nonlinear metasurface coating that changes its conductive topology in response to the power of the incoming wave. It converts from behaving as a simple capacitive sheet over a ground plane into a high impedance surface when the signal level surpasses the turn-on voltage of diodes at the vertical vias, and they become conductive. Resistors between the patches provide substantial absorption near the LC resonance frequency, which may be set by the appropriate choice of the patch shape and substrate thickness. We have designed the surface to provide a significant absorption contrast at 2.4 GHz, and have demonstrated a change from 10 % to 70 % absorption with increasing power level, for small samples inside waveguides. Furthermore, we have performed planar near-field scans on electrically large surfaces. We have shown that at high power levels, the nonlinear metasurface can provide greater attenuation than a conventional magRAM coating near its design frequency. We have also shown that it can limit the amount of electromagnetic leakage through a gap in a metal enclosure, demonstrating that it can be used for practical applications.

Chapter 3 is based on and is mostly a reprint of the following papers: **S. Kim**, H. Wakatsuchi, J. Rushton, D. Sievenpiper, ”Switchable Nonlinear Metasurfaces for Absorbing High Power Surface Waves”, *Applied Physics Letters* **108**, 041903, 2016.; **S. Kim**, H. Wakatsuchi, J. Rushton, D. Sievenpiper, ”Nonlinear Metamaterial Surfaces for Absorption of High Power Microwave Surface Currents”, IEEE Antennas and Propagation Symposium

Digest, Orlando, FL, USA, July 8-14, 2013. The dissertation author was the primary author of the work in this chapter, and the co-authors have approved the use of the material for this dissertation.

Chapter 4

Self-Tuning Metamaterial Surfaces

Conventional absorbers of resonance type offer various implementations due to their thin and lightweight characteristics. There is, however, a fundamental relationship between the electrical thickness of the absorbing materials or structures and their absorption capability. Thus, compatibility between the thinner absorber and the broader absorbing properties is not easily available by linear and passive methods, even though the instantaneous bandwidth is still limited. In this chapter, a new concept of an electromagnetic absorber has been addressed with a nonlinear and active feedback circuit, and eventually gives a broadband tunability, which is greater than the instantaneous bandwidth for any of the individual tuning frequencies.

4.1 Concept and Mechanism

4.1.1 Background and Motivation

In general, reactive surfaces used as a resonant absorber have limitations in their narrow bandwidth, which is determined by the relationship between the bandwidth and the

thickness. Thus, it is not available from a wide bandwidth absorbing structure, which has a relatively thin thickness, even metamaterial, or matasurface absorbers, which was discussed in previous chapters. For an instant, the bandwidth of the conventional high impedance surface has been determined by a thickness of the dielectric substrate.

$$B = \frac{2\pi\mu_r t}{\lambda_0} \tag{4.1}$$

Here, the μ_r is the relative permeability of the substrate, λ_0 is the wavelength of the center frequency at the electromagnetic band gap (EBG) of the high impedance surface, and t is the thickness of the substrate. For example, a reactive coating surface built for 1-2 GHz range has around 4% of bandwidth. There are several approaches to achieve broad bandwidth performances in applying a multi-resonant structure such as a different size of unit cells or multilayers with different unit cell geometry. As with other methods, the Q-factor can be manipulated by adding a loss (4.2) to the lower Q-value for the broader bandwidth. Nevertheless, the linear and passive techniques to achieve the wide bandwidth have restricted its use in practical implementations.

$$Q = \frac{X}{R} = \frac{B}{G} = \frac{Engergystored}{Energydissipated} \tag{4.2}$$

Metamaterials with nonlinear circuit components can give an additional degree of freedom to help manipulate unique characteristics in the limitation of linear approaches. The unit cells constructed in metamaterials display a periodic array on a sub-wavelength scale, and behave like an electrically effective medium, including effective permittivity ε_{eff} and permeability μ_{eff}, which properties can be determined by the deployed nonlinear circuits. To achieve a broad bandwidth over the linear limitation, we suggest a novel concept of

nonlinear active metamaterial surfaces.

4.1.2 Mechanisms for Self-Tuning Metasurfaces

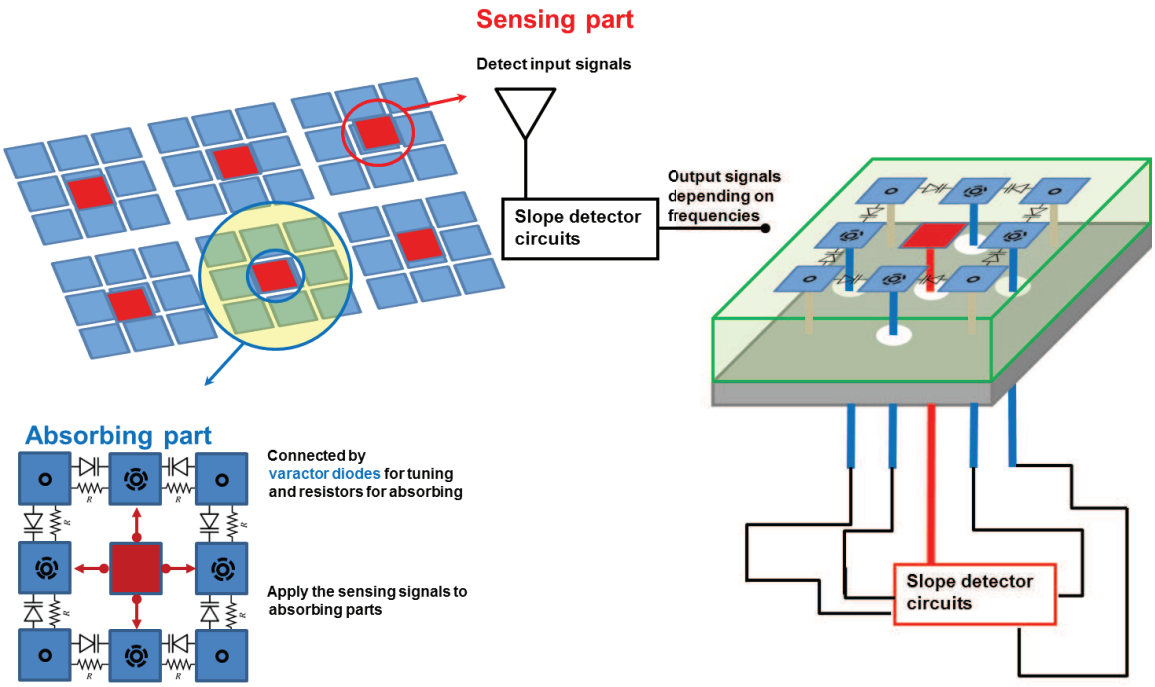

Figure 4.1: Mechanism diagram for the self-tuning metasurface

The main mechanism of the self-tuning metasurface is basically based on the tuning methods. In general, metamaterials are passive and linear mediums with fixed resonant frequencies. Thus, the tunability of the metamaterials is conducted by populated circuit components and external devices in order to tune the resonant frequencies. Previously, the tunable mechanism works are carried out by diodes electrically [50, 51, 52], MEMS devices mechanically [53], and transistors [54]. In particular, the electrical tuning methods by diodes required external DC bias to transit the impedance of the diodes. Most of the tuning systems needed an external source, extra controller, computer-based tracking systems, and manual calibration. Additionally, the tuning system is independent of the incident signals.

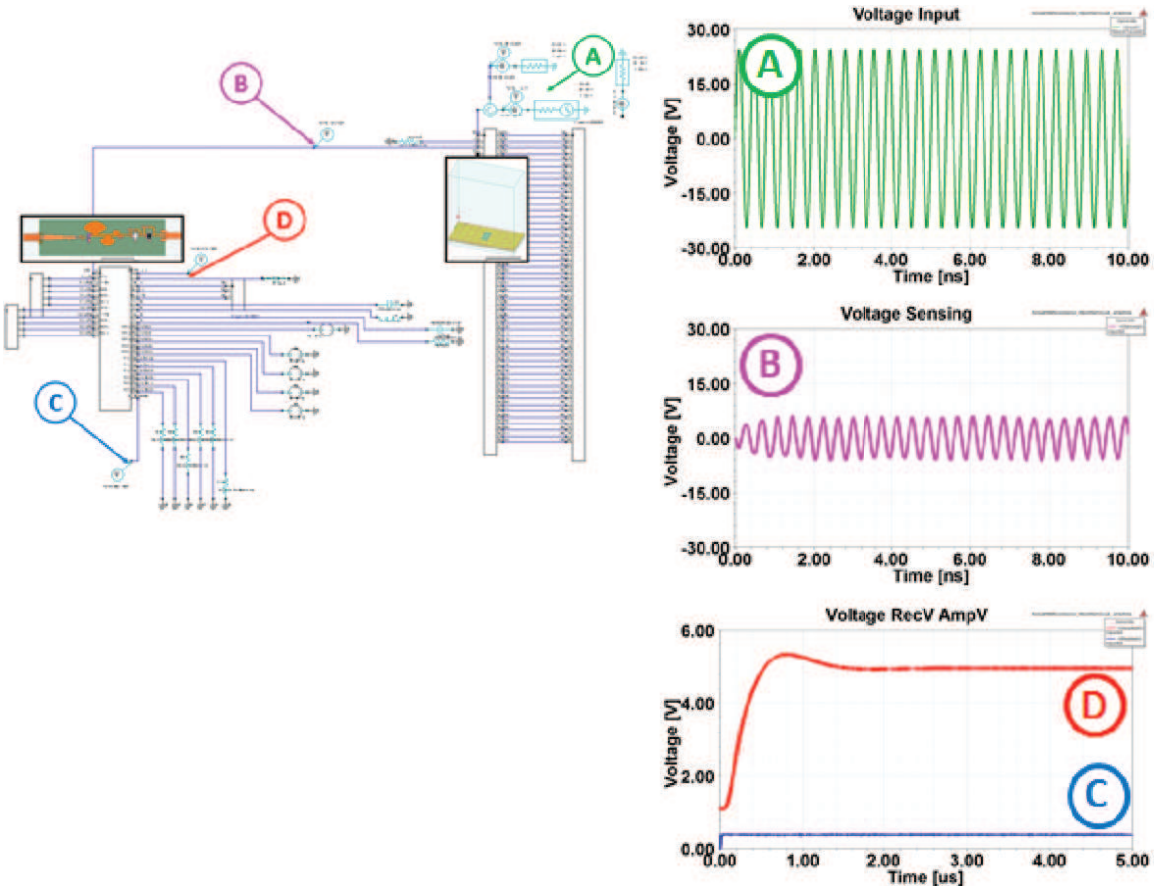

Figure 4.2: Scheme of the co-simulation

Here, the proposed active metasurface induces a unique tuning system, which results in adaptive tunability that depends on incoming frequencies. In other words, the tunable metasurface is able to sense a frequency of an incident signal, and then alters to match the frequency, called *self-tuning*. To achieve this newly tuned mechanism, the self-tuning metasurface involved two states: sensing and responding parts as shown in Fig. 4.1. The responding part was constructed from the high impedance surface and varactor diodes embedded in the gap between the periodic metallic patches on the metasurface. The sensing part was basically based on an RF-DC rectifier, which consists of a slope detector and a diode rectifier circuit to generate DC voltages to assign bias to varactors on the responding part.

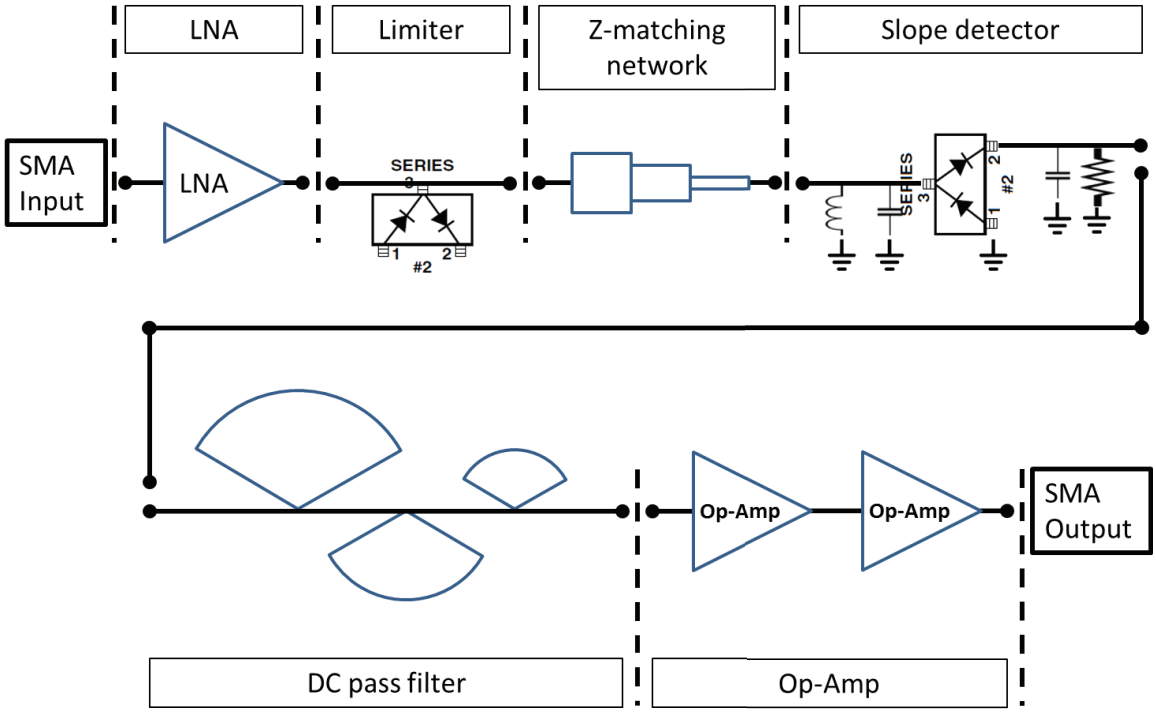

Figure 4.3: Overall scheme of the self-tuning circuit board.

To verify the rectified DC voltage, we carried out a co-simulation of full wave EM simulation and circuit analysis under a time transient as shown in Fig. 4.2. In the co-simulation, transient voltage data are checked at four steps: Ⓐ represents input RF signals at 3 GHz with 1 W as a source power to the metasurface in the normal direction of incoming waves, Ⓑ represents sensing voltages after the sensing unit cell, Ⓒ shows rectified DC voltages through the self-tuning circuit, and Ⓓ exhibits the amplified DC bias with the gain of 10 and DC offset of 1 V from the rectified voltages at the output of the self-tuning circuit board. Therefore, we verified total co-simulation can generate a proper DC bias to tune the varactors on the surface for the nonlinear active metasurface.

4.2 Self-Tuning Circuit Board

The overall scheme of the self-tuning circuit board is shown in Fig. 4.3. The designed circuit board has a broadband frequency response from 1 to 4 GHz. The circuit board has consisted of an LNA to amplify input powers, a limiter to only depend on incoming frequencies, a Z-matching network for broadband frequencies, slope detector to response input frequencies, DC pass filter for the generated DC, and op-amps to match the desired control bias to the varactors on the self-tuning metasurface. The input and output ports are matched to 50Ω. The input port is directly connected to the sensing cell of the metasurface. The LNA is used to amplify input signals through the sensing cell on the metasurface. The efficiency of the RF-DC rectification is determined by input powers toward to the rectifying diode.

$$\eta_{RF-DC} = \frac{P_{DC}}{P_{RF}} = \frac{V_{DC}^2/R_L}{P_{RF}} \tag{4.3}$$

Here, V_{DC}^2 represents the rectified DC voltages at the output, R_L, which represents a load resistance, $700k\Omega$, and P_{RF}, which represents an input power to the rectifying diode. A RF limiter is used to assign stable input powers to the diode for an interesting frequency band. The characteristic impedance is 50Ω, and the input impedance of the diode is $(67.4+j9.2)\Omega$. Thus, impedance matching network is applied to transfer between the different impedances to avoid impedance mismatch. The slope detector is designed with a lumped LC component in a parallel connection and a rectifying diode. After the slope detector, three cascade radial stubs were used as RF harmonic filters. The rectified DC voltages are required to match the desired DC bias to control the varactor diodes in the responding part.

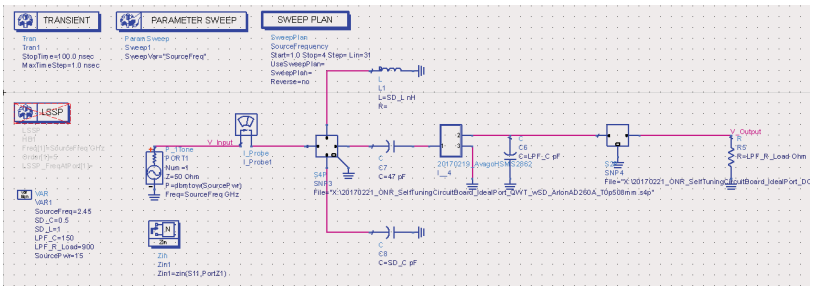

Figure 4.4: ADS circuit scheme for the rectifying diode

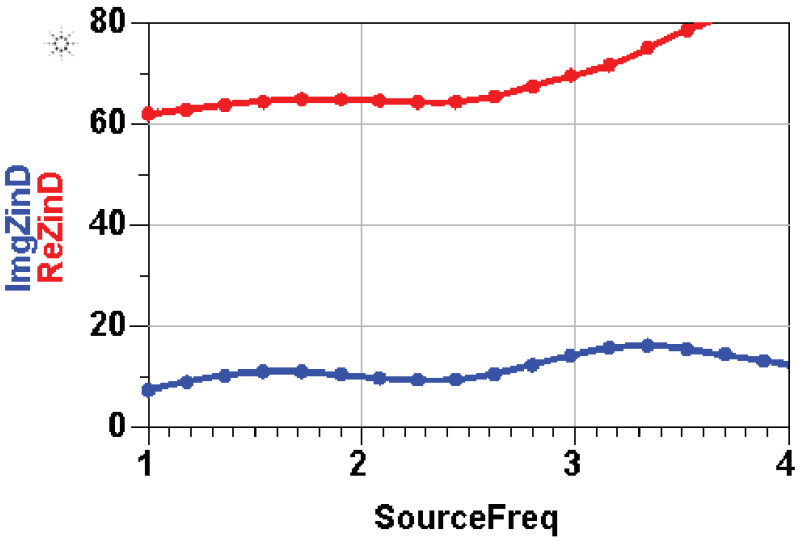

Figure 4.5: Input impedance of the rectifying diode

4.2.1 Rectifying Diode

With the rectifying diode, the packaged Schottky diode Avago Tech. HSMS-2862 adopted. Two diodes were in series connection in the package. From a manufacturer data sheet of the diode, the equivalent circuit parameters were derived: $V_F = 0.3V$, $R_s = 6\Omega$, $C_{j0} = 0.18pF$, and $V_B = 7V$. The voltage doubling rectified circuit model in ADS is shown in Fig. 4.4. The input impedance of the diode is also shown in Fig. 4.5. The input impedance of the diode was simulated to $(67.4 + j9.2)\Omega$ when the input power was 15 dBm. In Fig. 4.5, the variation of the impedance is small in a relatively broad bandwidth.

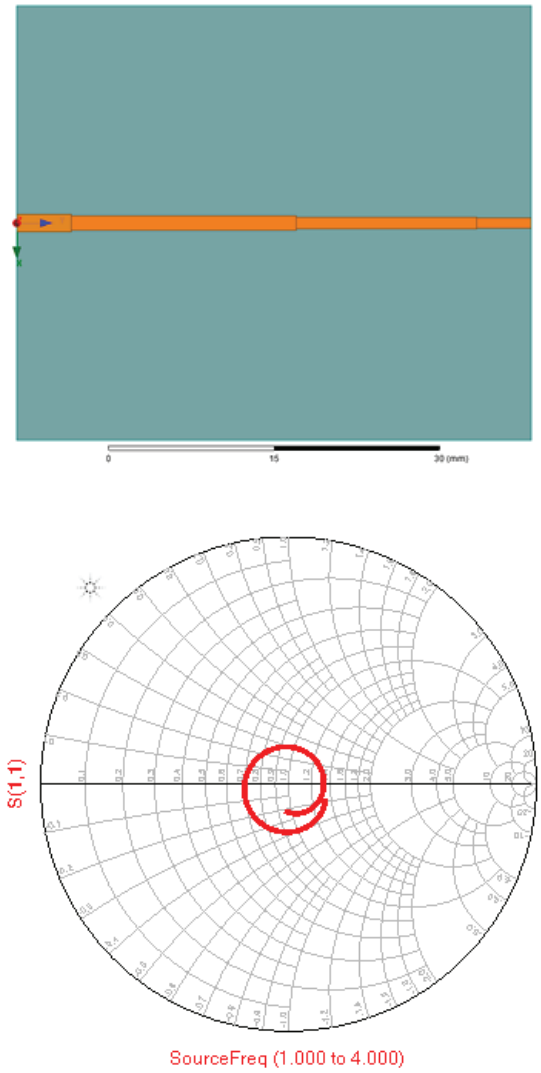

Figure 4.6: Model and simulation data of impedance matching network

4.2.2 Impedance Matching Network

The rectifying circuit had an impedance mismatch between input impedance and the input diode impedance, so three cascaded sections of a quarter wavelength transformer were used, which helped to enhance the bandwidth. The impedance for broadband frequencies was properly matched as shown in Fig. 4.6.

4.2.3 DC-Pass Filter

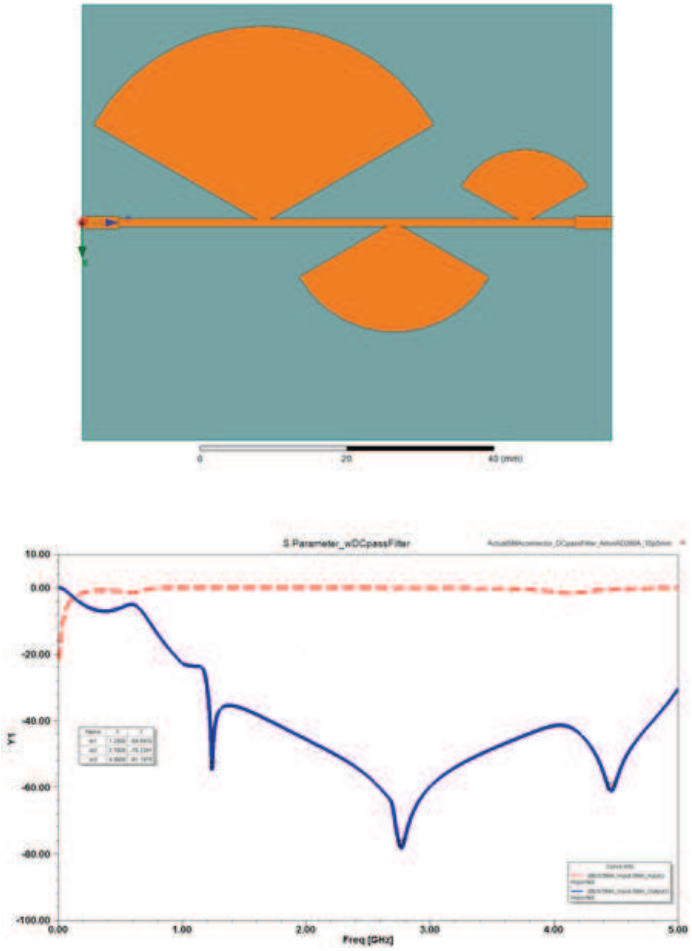

Figure 4.7: Model and simulation data of DC-pass filter

From the output of the rectifier, three radial fan stubs with different radii were attached to block the fundamental frequency and higher harmonics generated by the diode as shown in Fig. 4.7. According to the different radii, the first radial stub with the longest radius inhibited the fundamental mode. Similarly, the second and third radial stubs prohibited the second and third order harmonics, respectively. Moreover, the fourth harmonic is relatively very low, so additional fan shape stubs were not designed. From the simulation data, it can be observed that the magnitude of S11 was under 20 dBm within the desired frequency band

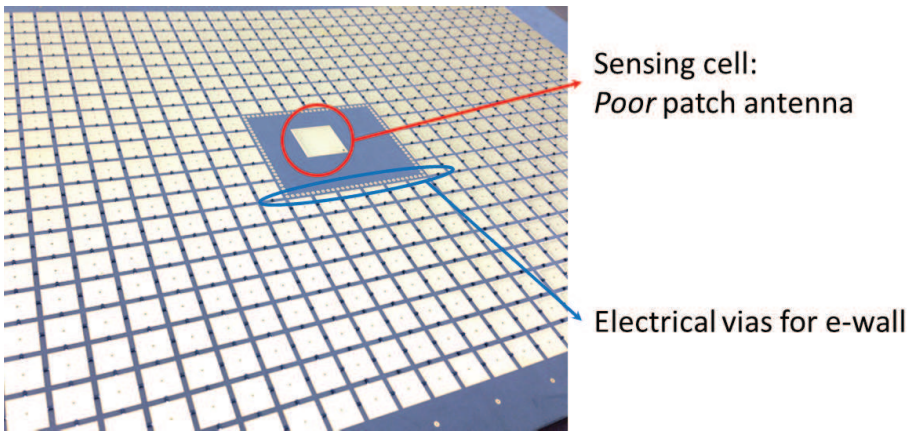

Figure 4.8: Fabricated sample of the self-tuning metasurface

from the fundamental, 2.45 GHz, to the third order harmonic, 7.35 GHz. Therefore, the radial stubs effectively suppressed the fundamental and higher harmonic modes.

4.3 Responding Part of Self-Tuning Metasurface

The self-tuning metasurface was planned to fabricate with the optimized sensing cell. The built metasurface was 25 x 40 cm with three Cu cladding layers including two dielectric layers. The top surface is shown in Fig. 4.8, and each unit cell has a 10 mm as period and a 1.4 mm as the gap distance. The first dielectric material is RO5880 with a 1.575 mm thickness, and the second one was on FR4 for the circuits, such as buffers and resistors, to protect the varactors. On the bottom surface, a physical hole is used to deploy a SMA connector to receive incoming powers through the sensing unit cell.

4.4 Measurement and Results

The closed-loop measurement setup under a high power system as shown in Fig. 4.9. In Fig. 4.9, the measurement setup is constructed with a VNA, two antennas, a self-tuning

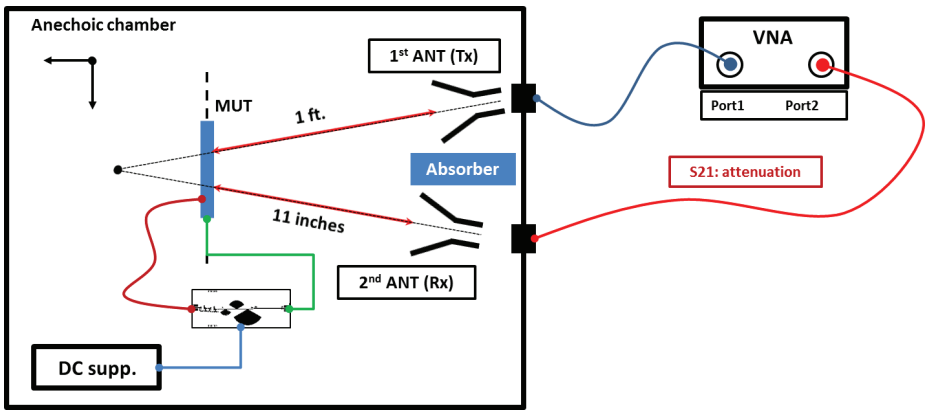

Figure 4.9: Scheme of the measurement setup

metasurface, a self-tuning circuit board, and DC suppliers to the op-amps of the circuit board. The first and second antennas were used as a transceiver (Tx) and a receiver (Rx), and placed away from the metasurface, 1 ft and 11 inches, respectively. Also, the angle between the two antennas was 20 degrees. The measurement scheme of the closed loop system is shown in Fig. 4.10. From the sensing cell of the metasurface, the input signals were amplified by the LNAs because the input signals were too low to activate the rectifier circuits on the self-tuning circuit board. The diode, which was used on the self-tuning circuit to show the stable rectifier performance under 15 dBm input power, also showed stable inputs in the self-tuning board will generate stable rectified DC voltages to tune the metasurface. The measurement data from the absorption under the high power closed loop system is shown in Fig. 4.11. The input power to the metasurface was 30 dBm, and frequencies were swept from 2 to 4 GHz. The thin solid lines represent a linear absorption while applying the DC bias from 1 to 14 volts to the metasurface directly. The blue dotted line represents a nonlinear absorption from the closed loop measurement, and the absorption band that appeared from 2.2 to 3.2 GHz. Some of the points showed unstable absorptivity because of the fluctuation input powers in the self-tuning circuit board. The unstable input powers were from the near-field effect between the source antenna and the metasurface. To

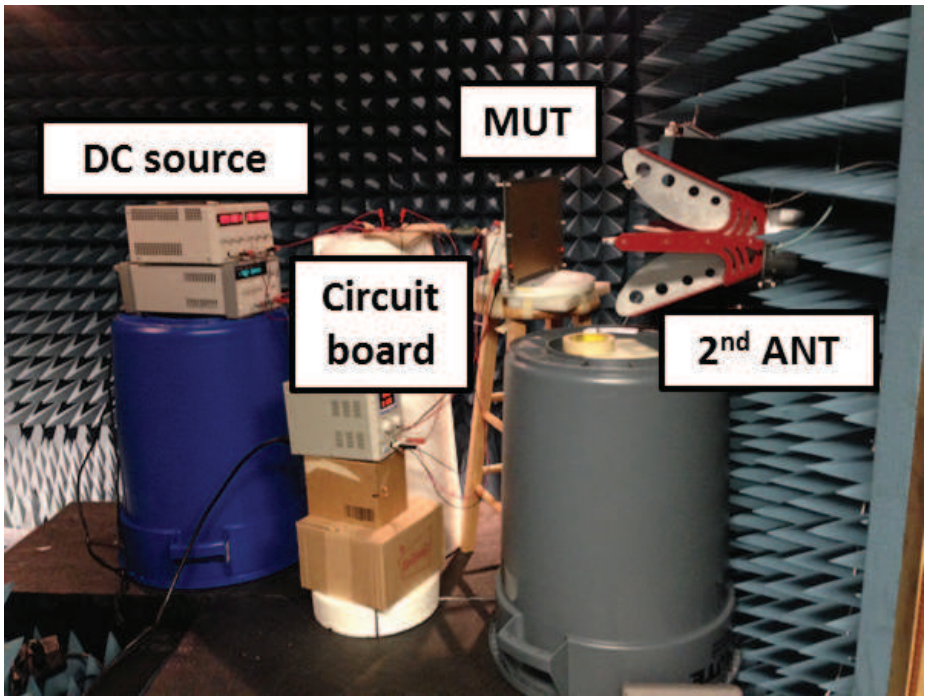

Figure 4.10: A photo of the measurement setup in the anechoic chamber

assign stable input powers to the self-tuning board, we first applied a coaxial limiter, but the limiter performed poorly in the broadband frequency range. In other words, we needed to manipulate the input powers so that they were matched to 15 dBm by controlling the source powers of the first antenna. Therefore, we needed to apply different input powers to the source antenna, so that it would give broader and better absorption data.

4.5 Conclusion

In this chapter, we introduce the self-tuning metasurface with a feedback circuit to operate as a relatively broadband absorber. The metasurface is divided into states. The self-tuning circuit part can first detect a frequency of an incoming wave, and then generate a DC bias to control the varactor diodes on the metasurface. Therefore, the metasurface can be tuned to its resonance frequency to match the frequency of the incoming wave. Eventually,

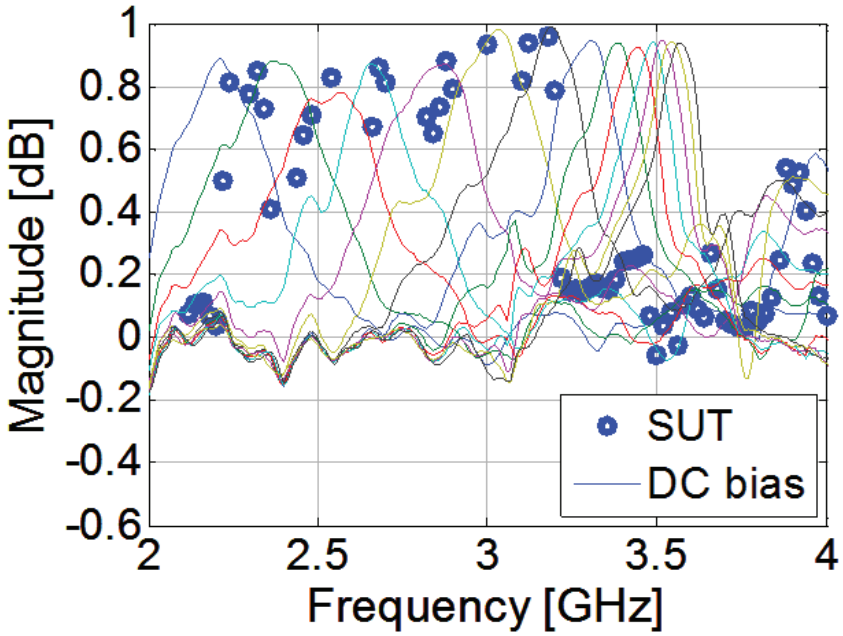

Figure 4.11: Measurement data from the self-tuning metasurface

the tunable range of the metasurface can be extended over the limitation of the linear and passive metasurfaces.

Chapter 4 is based on and is mostly a reprint of the following paper: **S. Kim**, A. Li, D. Sievenpiper, ”Self-Tuning Metamaterial Surfaces”, in preparation. The dissertation author was the primary author of the work in this chapter, and the coauthors have approved the use of the material for this dissertation.

Chapter 5

Reconfigurable Impedance Ground Plane

In this chapter, a reconfigurable impedance ground plane is addressed for broadband antenna array systems. The reconfigurable elements need an adjustment of the local reflection phase to operate over a broadband frequency range. The proposed reconfigurable array is constructed based on high impedance surfaces with RF metal-oxide-semiconductor field-effect transistors (MOSFETs) populated at the gaps between the patches. The transistors play the role of RF switches to manipulate the surface topology by connecting or disconnecting nearby periodic patches. We numerically demonstrate the novel tunable ground plane and simulation results to show the extreme tuning range from 2 to 17 GHz by using ideal transistor switches, while maintaining the artificial magnetic conductor properties of the high impedance surface. The invented reconfigurable ground array can be extended to the low frequency performance by enabling the array to operate efficiently, even when electrically near to the ground plane, and by enabling the elimination of scanned blindness even over multiple octaves of frequency scanning by controlling the coupling between elements, as

mediated by the ground plane.

5.1 Background and Motivation

Low profile reconfigurable and phased array antennas for broadband frequency range have widely attracted interests for wireless and satellite communications, as well as other applications. In general, an antenna located parallel to and with a fixed distance near a conducting surface is expected to operate at a resonance frequency. The distance has a fixed delay, which determines the reflected phase at the resonance frequency. The reflected waves from the ground undergo phase reversal upon reflection, and thus, they will have destructive interference unless the antenna is placed $\lambda/4$ distance from its conductive ground plane. A high impedance surface [6, 55] has already been shown to enable a low profile ground plane less than $\lambda/4$ due to its behavior as an artificial magnetic conductor [56], which provides in-phase reflection and constructive interference across a limited bandwidth. The broadband tunable antenna placed adjacent to the ground has a fixed distance between them, so the reflected phase varies with frequency across a broad bandwidth. Thus, if the broadband reconfigurable antenna is required to have a low profile and to operate in the broad frequency band, the ground plane must be tunable or reconfigurable.

Tunable impedance surfaces have been previously studied using varactor diodes [50]. In these structures, the resonance frequency of the surface has been electrically tuned by varying capacitance values of the varactors by assigning various bias voltages. The tuning range of the surface has been limited, however, based on the varactor properties itself. Additionally, varactors have a relatively narrow tuning range, and a high non-linearity at the lower end of their bias range.

Therefore, we propose a novel impedance ground plane based on RF transistors for a

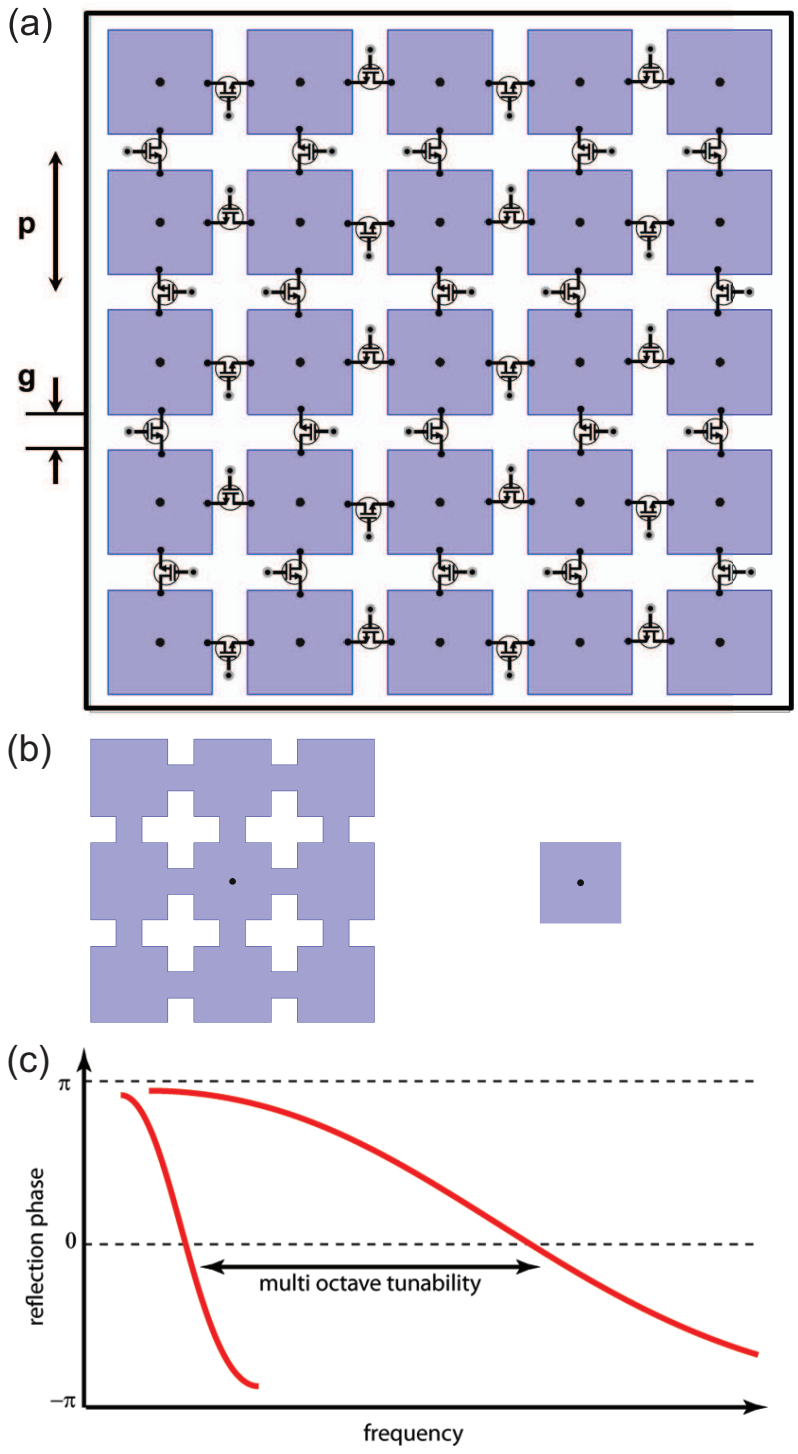

Figure 5.1: A diagram and mechanism of the reconfigurable impedance ground plane. (a) The top view of the reconfigurable metasurface with RF switches. (b) The configured surface topology to 3 x 3 and 1 x 1. (c) The reflection phase curves with multi-octave tunability.

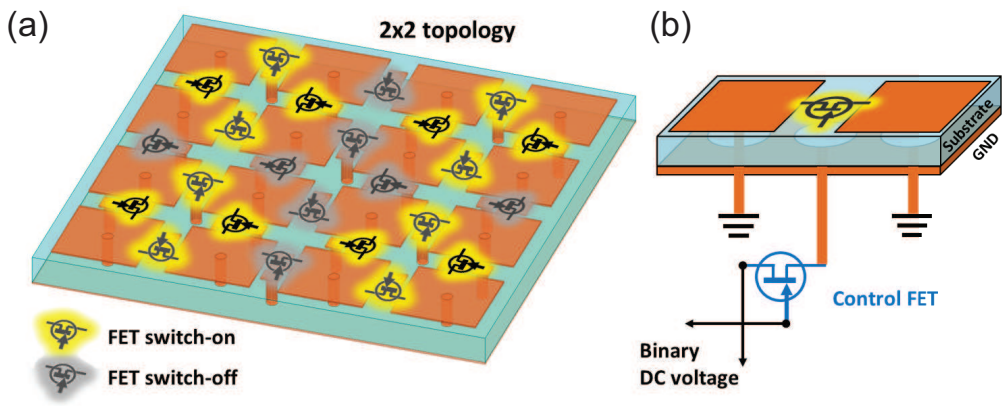

Figure 5.2: A scheme of the reconfigurable surface topology. (a) An example of 2 x 2 surface topology. (b) A brief circuit scheme on the metasurface to control the RF MOSEFET switch.

wideband tunable surface, as shown in Fig. 5.1 (a). The reconfigurable structure consists of two-dimensional metallic patches connected by RF MOSFETs. The patch has $p = 3.2mm$ as a period and $g = 0.81mm$ as a gap distance. By applying transistors to the impedance surface rather than varactors, they exhibit high linearity due to their discrete on/off states and their extreme wideband tuning performance by manipulating the surface topology as shown in Fig. 5.1 (b). For instance, manipulated reconfigured schemes of 3 x 3 and 1 x 1 are shown for low and high resonance frequencies, where the reflection phase crosses through zero, respectively. This is also the frequency where antennas located near the surface will operate efficiently. The reflection phase curves for two different high impedance surfaces with the different resonance frequencies are shown in Fig. 5.1 (c). By reconfiguring the surface between these two states, or any state in between, we can tune the antenna response over a wide range of frequencies. In other words, the MOSFETs based reconfigurable plane can form N x N configurations by shorting adjacent patches, and thus, it is tuned in a digital manner to show multi-octave tunability from a single patch to the larger patches. For example, the manipulation of the 2 x 2 configuration has been done to turn on/off the RF

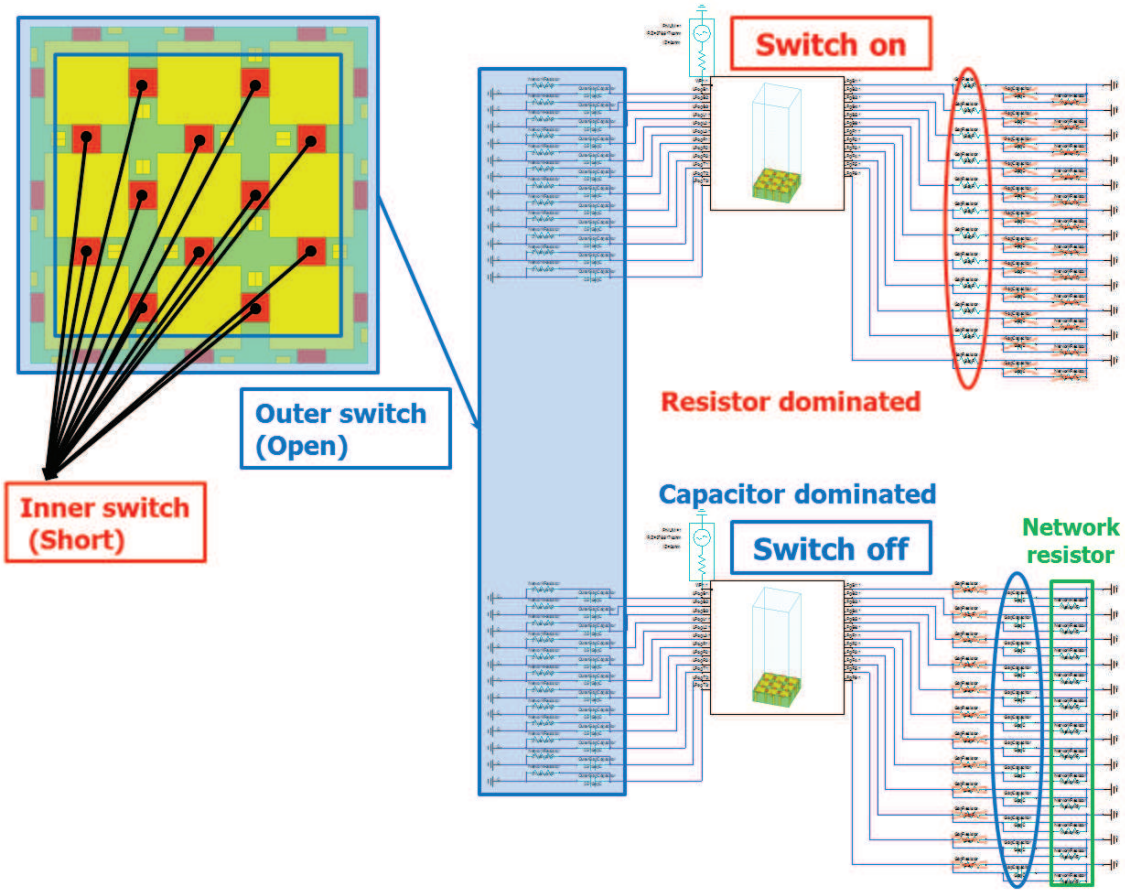

Figure 5.3: A circuit scheme of the co-simulation for the switch on/off states.

MOSFET switches of inner/nearby patches as shown in Fig. 5.2 (a). The RF MOSFETs as an RF switch are used to transmit maximum power without introducing nonlinearities, and are controlled by the other FETs to assign binary DC voltages as shown in Fig. 5.2 (b). The transistors have an advantage in that they provide a discrete on or off state, within which they can be highly linear. Therefore, the tunable plane will be built using the same GaN switches used in the reconfigurable array element itself.

5.2 Simulation Results

The proposed reconfigurable ground plane has been numerically analyzed under a co-simulation method with EM simulation by AnsysHFSS and circuit analysis by Ansys Designer as shown in Fig. 5.3. For the EM simulation, an N x N unit cell structure is constructed with infinite boundary conditions and lumped ports between patches for the ideal RF MOSFETs, which act as the switches. The patch of the single unit cell has a period of 3.2 mm and a gap distance of 0.81 mm on a dielectric substrate, RO5880 ($\varepsilon_r = 2.20$ and $tan\delta = 0.0009$), with a thickness of 2.87 mm. For the circuit simulation, the ideal N-channel RF MOSFETs are controlled by network biasing to provide open and short channels between the patches. For instance, from Fig. 5.3, the 3 x 3 manipulated array has the shorted inner switches to connect the patches for the array and the opened outer switches to isolate the nearby array. When the switches are turned on, an internal resistance of the transistor is dominant, called insertion loss. Similarly, a parasitic capacitance of the FET is dominant, while the switches are turned off. Therefore, the transistor based metasurface can be reconfigured by arranging groups of the cells into clusters. The metallic lattice of patches are arranged into groups of 2 x 2 through 11 x 11 or simply as all disconnected cells, specifically for the 1 x 1 case. Reflection phases, $\angle S11$, are compared in each different topology. In the 1 x 1 case, all of the patches are disconnected, so the surface creates an ordinary high impedance surface with a resonant frequency of 11.86 GHz defined by the single unit cell geometry.

As increasing the number of connected channels to form N x N surfaces, the capacitance between patches and inductive path increase as they follow the expanded effective patch size, so the resonance frequencies are moved to a lower frequency range as shown in Fig. 5.4 (a), which varies reflection phase curves from 1 x 1 to 11 x 11 reconfigured

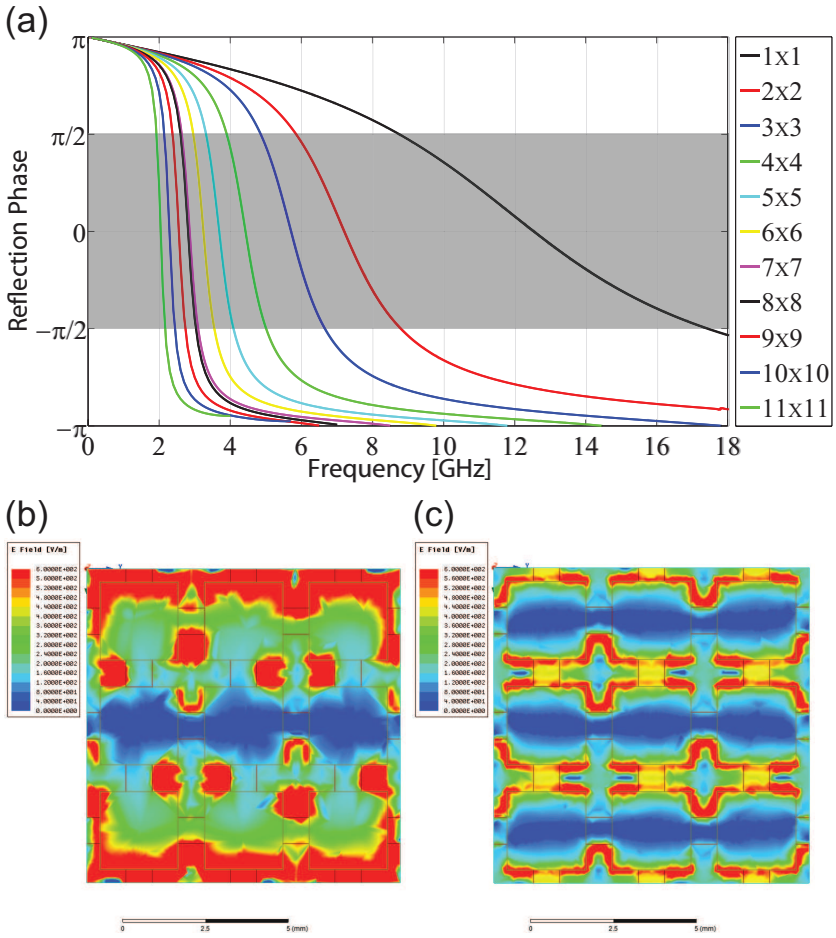

Figure 5.4: Simulation results of the reconfigurable ground plane with the ideal RF switches. (a) Reflection phase of N x N surface topology. E-field profiles of (b) 3 x 3 and (c) 1 x 1 configurations.

impedance ground plane. The reflection phase bandwidth determined from $-\pi/2$ to $\pi/2$ in each configured surface is slightly overlapped by neighboring bandwidth. For example, the tuned surfaces of 1 x 1 and 2 x 2 patterns have the bandwidth of 8.75 - 17.4 GHz and 5.85 - 8.8 GHz, respectively, so the bandwidth of the lower edge of 1 x 1 and the upper edge of 2 x 2 is superposed at 0.05 GHz. Therefore, the reconfigurable plane can operate as an artificial magnetic conductor across the tunable frequency range from 2 to 17 GHz within the shaded region as shown in Fig. 5.4 (a). E-field profiles on the surface for different arrangements of the unit cells are plotted under the same scale as shown in Fig. 5.4 (b) and (c). Fig. 5.4 (b)

shows the E-field magnitude of the 3 x 3 topology at the resonance frequency 5.19 GHz, while Fig. 5.4 (c) represents the 1 x 1 pattern at 11.85 GHz. The surface field profiles verify that the surfaces configured by applying the network bias have tunable reflection phase states.

5.3 Prototype Reconfigurable Surface

The proposed reconfigurable metasurface with the ideal RF MOSFETs enables covering the extreme frequency band from 2 to 17 GHz. The parasitic values such as an internal resistance, capacitance, and inductance, however, can affect the desired performance. Therefore, a prototype board was built to verify the operation of the impedance manipulation by changing the configuration of the network RF transistors. The fabricated board consists of 6 x 6 array and the geometry of the unit cell patch of the sample is 18 mm of the period and 2.5 mm of the gap distance on the RO5880 material with 3.175 mm thickness. The operation frequency in maintaining the artificial magnetic conductor is from 1.5 to 5 GHz.

5.3.1 Simulation Data of Prototype Sample

The co-simulation data of the fabricated prototype metasurface is shown in Fig. 5.5. The reflection phase of the prototype structure has three different states of 1 x 1 to 3 x 3 configurations which were designed to operate over several waveguide bands, WR650 (1.15 - 1.72 GHz), WR430 (1.72 - 2.60 GHz), and WR284 (2.60 - 3.95 GHz), for measurement. Fig. 5.5 (a) represents the reflection phases with the ideal switches, while Fig. 5.5 (b) shows the simulation data with parasitic values of the RF switch, Skyworks SKY13347-360LF. The values of the parasitic are $R_on = 3\omega$ and $C = 0.1pF$, respectively. The reflection phases

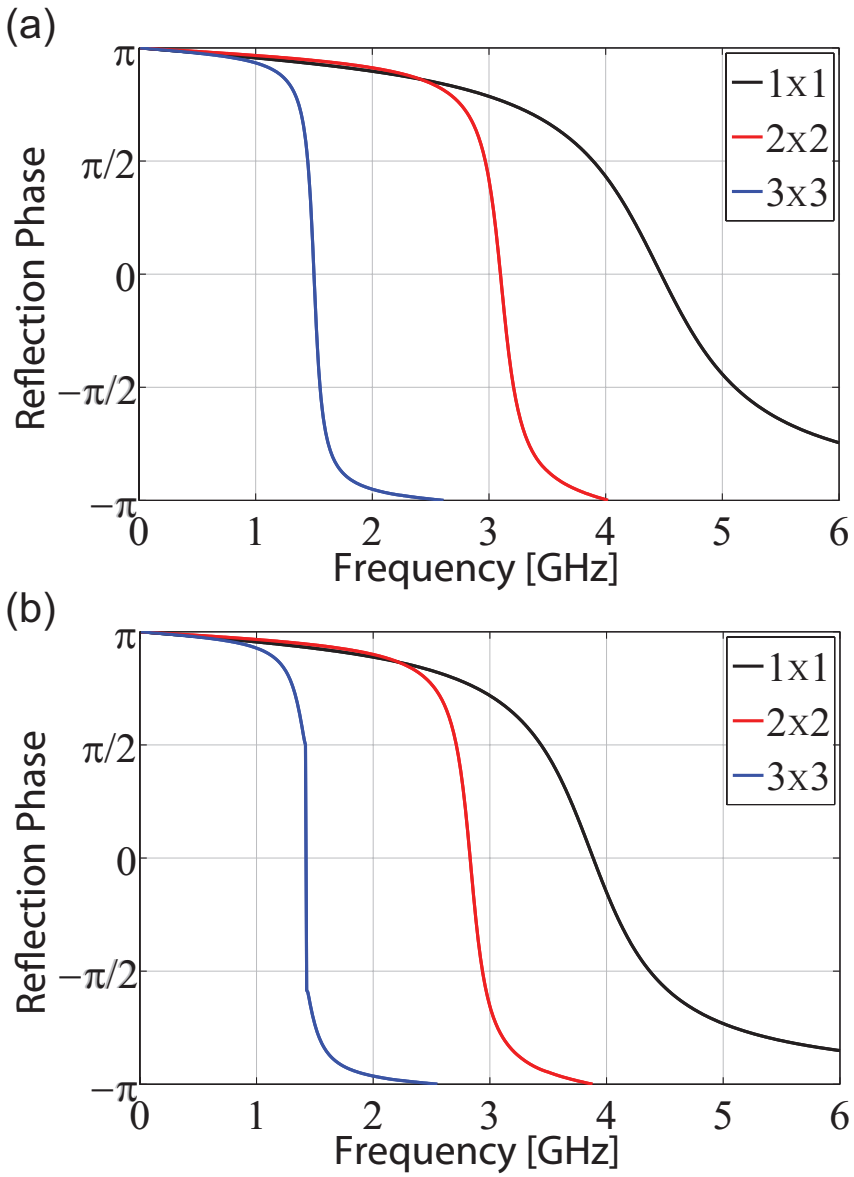

Figure 5.5: Simulation results of the prototype structure. Reflection phase with (a) the ideal RF switches and (b) the actual RF MOSFET including parasitic values.

with the actual SPICE model of the RF switch are shown of the shift to the lower frequency due to the parasitic effects.

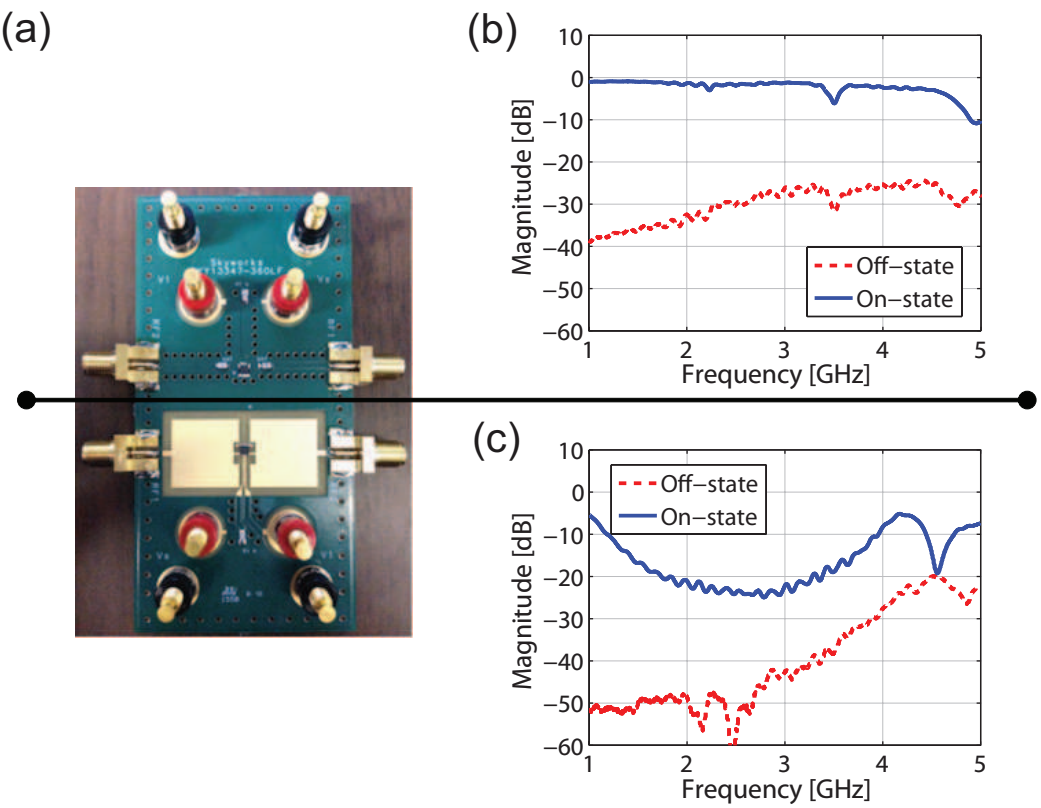

Figure 5.6: Test results of the candidate RF switch (SKY13347-360LF). (a) The fabricated test board. S21 data of on/off states (a) with and (b) without the 50 Ω impedance matching.

5.3.2 RF Switch

In order to identify appropriate switches for the initial prototype, we built a test board to evaluate the switch shown in Fig. 5.6 (a). This evaluation board contains four ports, which are connected by a pair of switches. The evaluation experiments involved both transmission through lines, and through pairs of patches identical to those that we intended to use in the prototype array. This approach has been allowed to test the basic switch properties and to verify its behavior in the intended electrical environment. Fig. 5.6 (b) shows the performance of the selected switch we used, which provided a high degree of isolation in the off-state, and a low insertion loss in the on state, and Fig. 5.6 (b) exhibits the

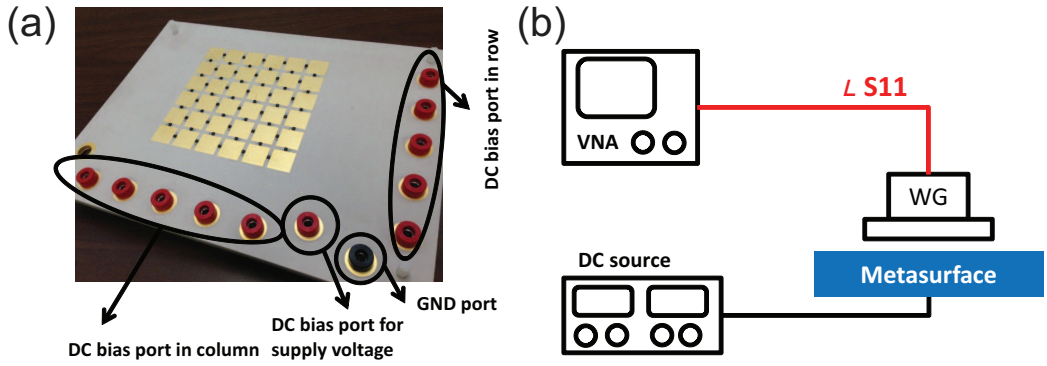

Figure 5.7: Measurement setup of the prototype reconfigurable impedance plane. (a) A photo of the prototype sample. (b) A brief scheme of the measurement system.

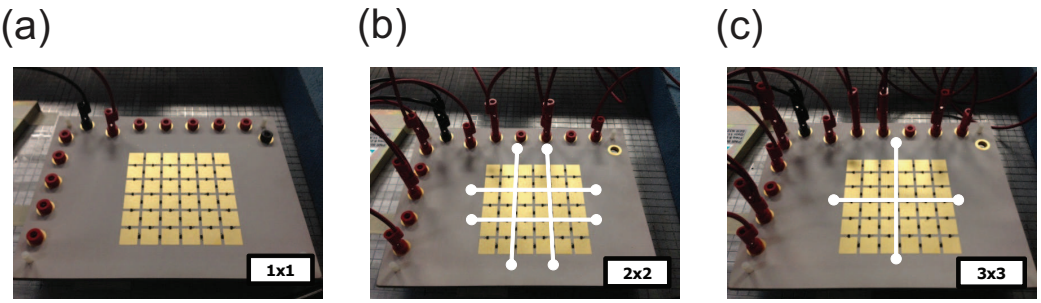

Figure 5.8: Photos of the reconfigured surface topology by assigning DC bias to (a) 1 x 1, (b) 2 x 2, and (c) 3 x 3.

S21 of on-off states while connecting to the actual patches. Thus, this switch was eventually selected for the initial prototype tunable ground plane after verifying the performance of the switch compared with the specifications described by the manufacturer.

5.3.3 Measurement

After selecting the transistor that provided the best performance, the test board which consisted of a 6 x 6 array of patches, has been fabricated, and each patch is connected to its neighbors by transistors with control lines arranged around the outside edge as shown in Fig. 5.7 (a). The measurement setup for the prototype sample is shown in Fig. 5.7 (b) including VNA to measure reflection phase, $\angle S11$, and DC source to control the RF

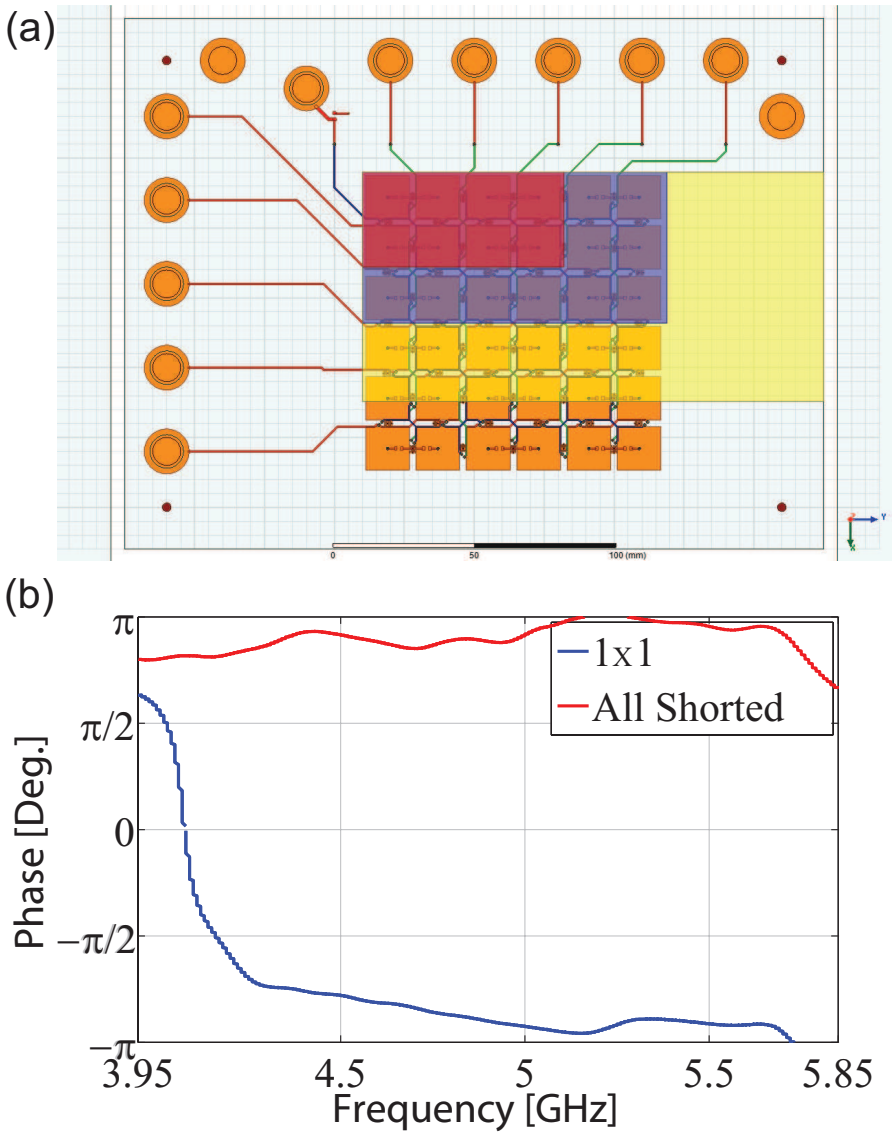

Figure 5.9: Measurement data of the prototype reconfigurable impedance ground plane. (a) The area of the switchable ground plane compared to various waveguide sizes that are indicated by red, blue, and yellow colored rectangles. (b) The blue and red lines represent the reflection phase of the 1 x 1 configuration and all shorted large patch such as a PEC.

MOSFETs. The board contained the dielectric substrate for the patches, as well as several other layers for the control lines, which were fed through the ground plane using vertical vias. The vias provide the gate contacts for the transistors.

By assigning DC voltages to the control lines in a row and column format, the tunable ground plane is capable of connecting or disconnecting various groups of patches by turning on or off the appropriate transistors. Fig. 5.8 shows the board tuned to the simple (a) 1 x 1 configuration, in which all transistors are off, and the (b) 2 x 2 and (c) 3 x 3 configurations, in which the transistors are turned off in every alternate row and every alternate column. Because of the control scheme we developed, only 2N control lines are required to address an N x N array of cells. The surface was initially tested to determine if the transistors were properly adjusting the conductivity between the plates. It was easily verified that the plates could be connected or disconnected row by column as intended. By connecting the appropriate bias lines, the plates could be arranged in 1 x 1, 2 x 2, or 3 x 3 clusters.

From the measurement, the ordinary open-ended waveguides have been used to measure the reflection phase. First, the waveguide against a flat metal surface is placed for calibration, and then the open ports were placed above the tunable metasurface to measure the switching between various states. Note in Fig. 5.9 (a) that each waveguide cross-section, indicated by various colored rectangles, covers only a small number of unit cells. In the highest band, the waveguide only covers eight cells in the 1 x 1 configuration, whereas in the lowest band, the waveguide is only partially filled by the tunable surface. Only in the mid-band, the waveguide can completely cover the tunable surface, but even in that instance it only covers 24 cells in the 1 x 1 case, and only six cells in the 2 x 2 case. With such a small prototype sample, the area is hardly enough to obtain a good measurement of the

reflection phase. Nonetheless, the measurement enables to successful detection of the phase differences between various states. Fig. 5.9 (b) shows the comparison of two cases, in which none of the switches are closed, corresponding to the 1 x 1 case, and in which all of the switches are closed, corresponding to a fully conducting surface. A resonance is seen at around 4 GHz, which can be switched on and off electronically by changing the switch states. Unfortunately, for larger cell cluster the resonance frequencies are even lower, and we are not able to obtain reliable measurements below this frequency band due to the size of the surface.

5.4 Conclusion

In this paper, we demonstrate a novel transistor based metasurface for the reconfigurable impedance ground plane. By connecting the multiple metallic patches together, the surface can be tuned to cover a wide range of the different resonance frequencies. The tuning range of the surface is from 2 to 17 GHz. From the prototype sample of the reconfigurable ground plane, the configuration enables the tunable impedance topology by manipulating the RF switches. Thus, the reconfigurable surface will provide advantages to broadband tunable antenna systems by tuning the ground plane itself.

Chapter 5 is based on and is mostly a reprint of the following paper: **S. Kim**, A. Li, D. Sievenpiper, ”Reconfigurable Impedance Ground Plane for Broadband Antenna Systems”, 2017 IEEE Antennas and Propagation Symposium, San Diego, CA, July 9, 2017. The dissertation author was the primary author of the work in this chapter, and the co-authors have approved the use of the material for this dissertation.

Chapter 6

Omni-Directional Metamaterial Surface

In previous chapters, the proposed metamaterial surfaces had a specific direction preference, such as the switchable absorbing metasurface responding to an incident wave in a parallel direction. Similarly, the self-tuning metasurface and reconfigurable ground plane can react to an incoming wave in a normal direction. In practical applications, the direction of incoming waves does not specify the ideal cases, in both normal and parallel directions. Therefore, there is the demand to consider a new type of metasurface to absorb illuminated microwaves, which are incoming toward the metasurface in arbitrary angles. Therefore, the new metasurface is applicable in all directions, including for the azimuthal ($\varphi : 0 - 2\pi$) and elevation ($\theta : 0 - \frac{\pi}{2}$) angles as shown in Fig. 6.1.

6.1 Background and Motivation

The metasurfaces used in this thesis are based on the high impedance surface, and the reflection phase shifted to a lower frequency as a result of increases in the incident angles from 0 (normal) to 2π (parallel) [50, 57, 58]. In practical use of the metasurface,

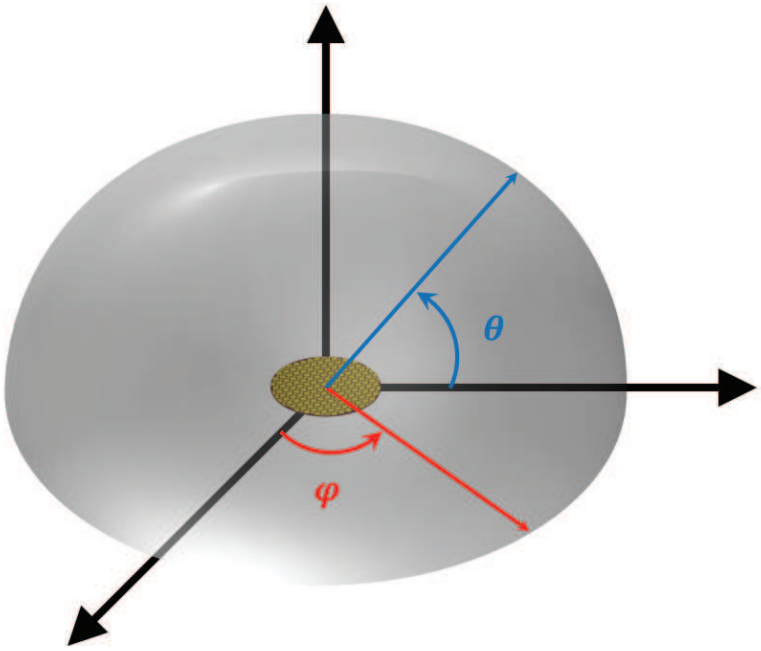

Figure 6.1: Concept of omni-directional metasurface

which was based on the high impedance surface as the microwave absorbing structure, there was an issue with the obliquely incoming waves that were effectively absorbed rather than the normal or parallel incident plane waves. The tangential wave vector component on the interface excited by an external plane wave is described as k_t. The propagation constant of the surface component to the normal is

$$\beta = \sqrt{k^2 - k_t^2}, where k = \sqrt{\varepsilon\mu} \tag{6.1}$$

The ε and μ represent the material properties of the absorbing structure. The tangential propagation constant for the plane wave with arbitrary angles in free space has an angle dependence.

$$k_t = k_0 \sin\theta k_0 = \omega\sqrt{\varepsilon_0\mu_o} \tag{6.2}$$

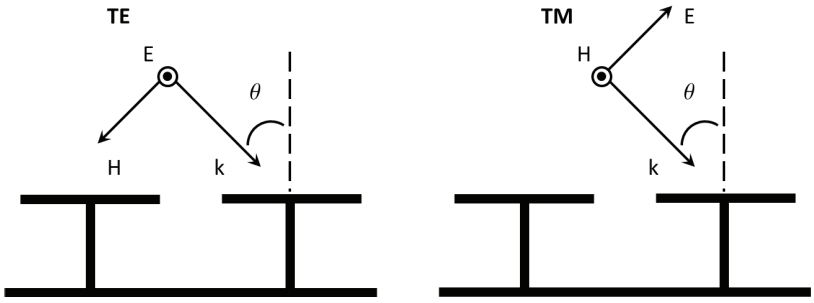

Figure 6.2: TE and TM polarization plane waves to high impedance surface

Therefore, if the incident angle of the plane wave is increased, the β is decreased. In other words, the electrical thickness of the absorbing surface is also decreased, so the resonance absorber like the Salisbury screen with the quarter wavelength distance from the grounded planes exhibits different resonance frequencies depending on the different incident angles.

With the conventional high impedance surface, the unit cell is consisted of a periodic metallic patch and conducting via shorted to the grounded plane. With the incident plane waves with oblique angles to the surface, we have to distinguish between the two different polarizations, the transverse electric (TE) and transverse magnetic (TM) polarized waves as shown in Fig. 6.2. The electric field of the TE polarized plane wave to the surface is orthogonal to the conducting via of the high impedance surface. When the TE waves are incident in the normal direction of the surface, the result is a no-current flow. In other words, the characteristics of the high impedance surface are same, even on a structure without vias. In Fig. 6.2, the surface impedance of the TE and TM polarized waves with the oblique angles are derived below.

$$Z_s^{TE} = \frac{\eta_0}{j\alpha(\varepsilon_r + 1)\cos^2\theta} \tag{6.3}$$

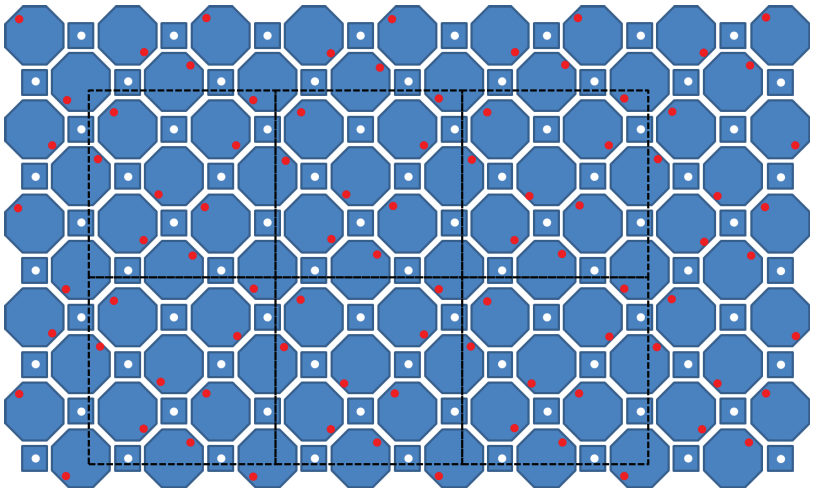

Figure 6.3: Brief scheme of the omni-directional metasurface

$$Z_s^{TM} = \frac{\eta_0}{j\alpha(\varepsilon_r + 1)} \tag{6.4}$$

$$\alpha = \frac{k_0 P}{\pi} \log\left(\frac{2P}{\pi g}\right) \tag{6.5}$$

Here, $\eta_0 = \sqrt{\frac{\mu_0}{\varepsilon_0}}$ is characteristic impedance in a free space, where α is a grid parameter including periodicity, p, and gap distance, g.

6.2 Mechanism of Omni-Directional Metasurface

The existence of the conductive vias shows different wave impedance to the TE- and TM-polarized plane waves. Eventually, the absorption performance is dramatically changed by the oblique angles of the plane waves. The proposed metasurface has been considered to exhibit this drawback in the microwave absorbing structure based on a high impedance surface. The isotopic patterning topology and offset vias are applied to achieve the desired characteristics as shown in Fig. 6.3. The isotropic surface consists of the nearby octagon

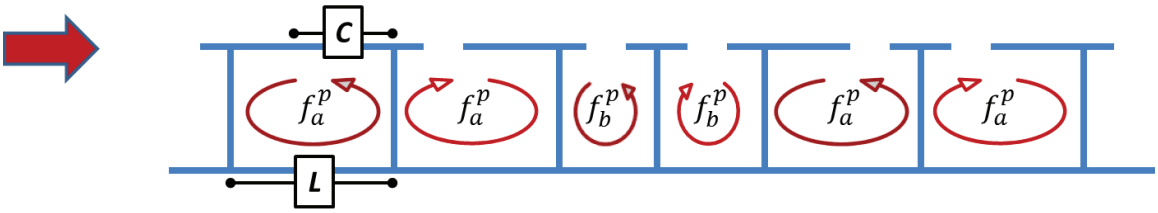

Figure 6.4: Scheme of the omni-directional metasurface in a parallel incident.

and square patches. At the metallic octagon patch, a position of the conductive via has offset from the center of the patch, whereas other vias at the square patches are located at the center. This anisotropic topology offers unique electromagnetic properties to be adapted into the incoming plane waves with the oblique angles in the azimuthal and elevation planes.

The mechanism of the omni-directional metasurface is based on an asymmetric induced current flow through the vias. When the parallel incident plane wave propagates to the metasurface, the resonance frequencies of the metasurface have occurred as shown in Fig. 6.4.

$$f_r^p = f_a^p + f_b^p \tag{6.6}$$

$$Here, f_a^p = \frac{1}{2\pi\sqrt{LC}} \tag{6.7}$$

Similarly, when the normal incident plane waves meet the metasurface, the induced currents through the via of the small patch, a square shape, canceled out each other on the conventional high impedance surface. The inductive currents, however, flow through the offset vias of the large patch, an octagon shape, because the asymmetrical currents due to the offset via allow to make the inductive current path between the large patches, instead of a small patch as shown in Fig. 6.5. Unlike the parallel incident case, the first term (6.8) is dominant in the normal case of the resonance frequency. Moreover, the first term of

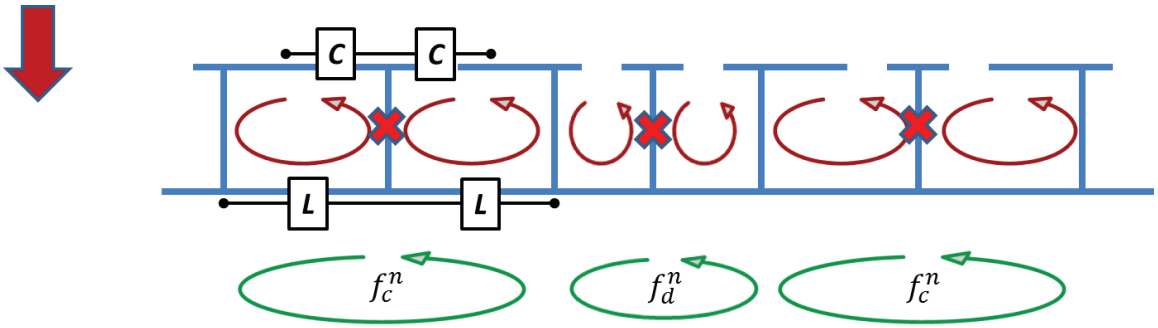

Figure 6.5: Scheme of the omni-directional metasurface in a normal incident.

the normal resonance frequency coincides as the the first them of the parallel resonance frequencies of (6.9) , (6.10), and (6.11)

$$f_r^n = f_c^n + f_d^n \tag{6.8}$$

$$Here, f_c^n = \frac{1}{2\pi\sqrt{2L(C/2)}} = \frac{1}{2\pi\sqrt{LC}} \tag{6.9}$$

$$f_c^n = f_b^p \tag{6.10}$$

$$f_r^n = f_c^n + f_d^n \cong f_b^p \tag{6.11}$$

Therefore, the overall resonance frequencies in the extreme cases, both parallel and normal incidents, have coincidences, that can be applicable to the adaptive oblique incident angle cases.

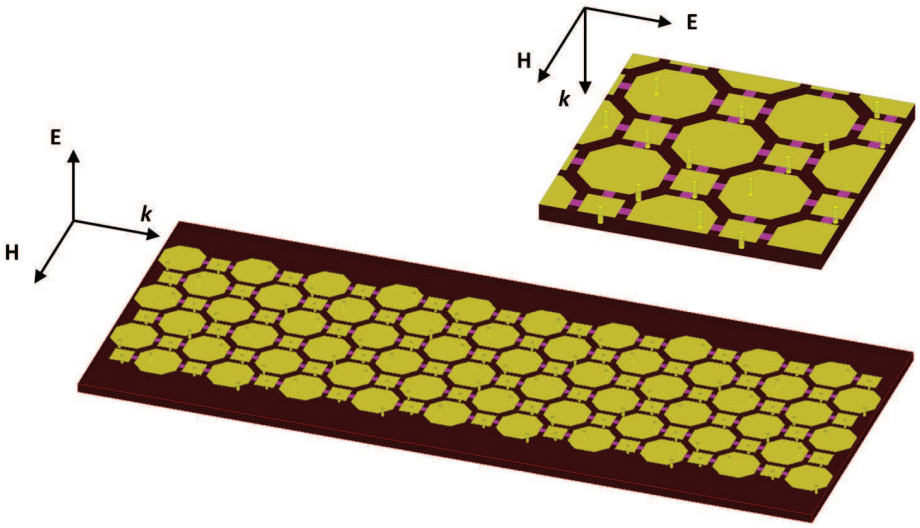

Figure 6.6: EM simulation models against the parallel and normal incidents

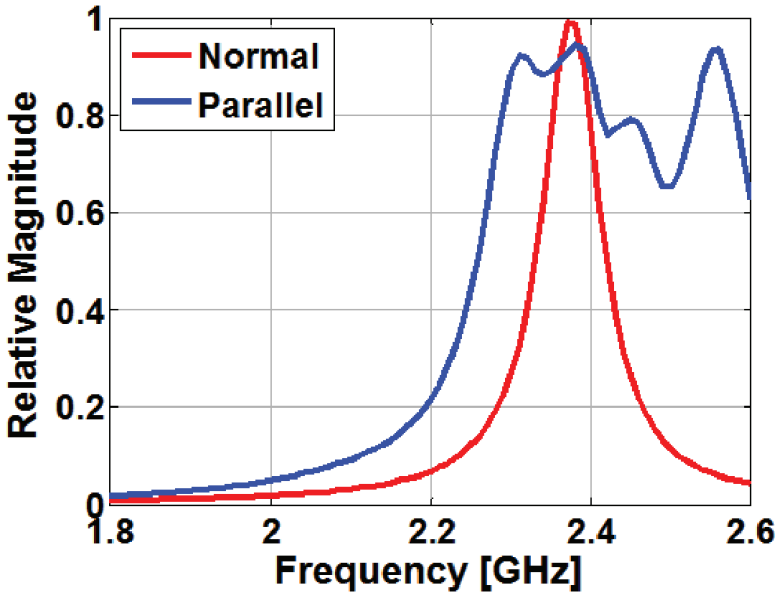

Figure 6.7: Simulation results of absorption in the parallel and normal incidents

6.3 Simulation and Measurement of Omni-Directional Metasurface

The simulation models have constructed two different cases, which include the parallel and normal incident waves to the metasurface as shown in Fig. 6.6. The periodicity

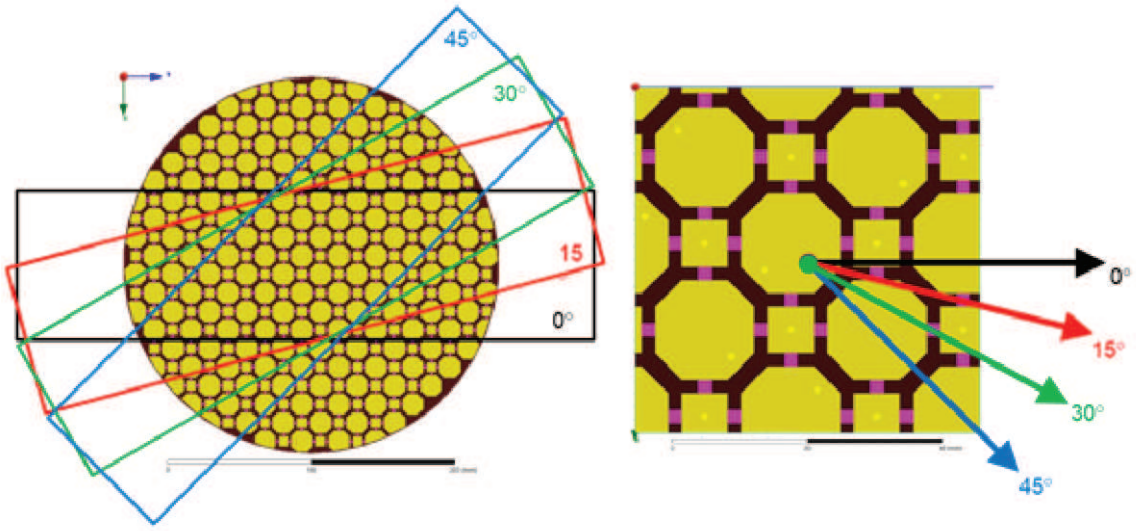

Figure 6.8: Simulation models with parallel and normal incidents on the azimuthal plane.

of the octagon and square patches are 17 mm and 6 mm, respectively, and the offset distance from the center point of the large patch is 7.5 mm. In the parallel incident model, the metasurface was built to fit in a waveguide, the WR430, with 6 x 20 unit cells. In the normal incident model, a single asymmetry unit cell simulated with periodic boundaries, a master and slave one. The simulation results of the omni-directional metasurface are shown in Fig. 6.7. The absorption plots against the parallel and normal incidents are represented as blue and red curves. The peak of absorption appeared at 2.38 GHz in both incident cases. Specifically, the parallel plot represents dual peaks due to two nearby resonance frequencies, and the normal plot represents a single peak because of the dominant resonance frequency from the large patch.

Another advantage of the omni-directional metasurface is that the surface has a symmetry condition in the azimuthal plane of the surface. Therefore, all the incoming waves on the different azimuthal angles ($\theta : 0\ 2\pi$) have the same wave impedance, so the absorption characteristics also have maintained in every direction on the azimuthal plane.

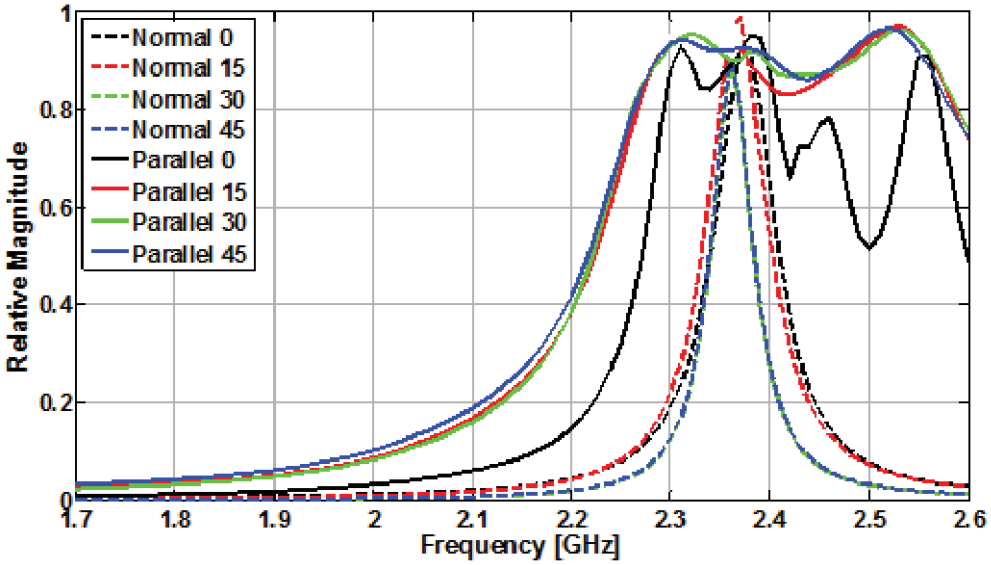

Figure 6.9: Simulation data with different azimuthal angles in parallel and normal incoming waves.

The simulation models have been constructed to adapt the parallel and normal incident waves with different azimuthal angles as shown in Fig. 6.8. For the parallel incident, a large circular surface was built symmetrically periodic impedance on the plane. The large circular panel was cut to four different sections with 0°, 15°, 30°, and 45° to cover all the possible directions in the azimuthal plane. For the normal incident, input waves in the simulation setup have assigned with the azimuthal angles the same values as the parallel case. The simulation data of the absorption peak under different azimuthal directions are shown in Fig. 6.9. From the simulation results, either parallel or normal incoming plane waves are highly absorbed around 2.38 GHz by the omni-directional metasurface.

Based on the numerical approach, the prototype omni-directional metasurfaces were built for absorption measurement as shown in Fig. 6.10. The two prototype samples were fabricated to fit into the waveguide, WR430. The large and small samples in Fig. 6.10 represent the incoming waves in the parallel and the normal directions, respectively. Re-

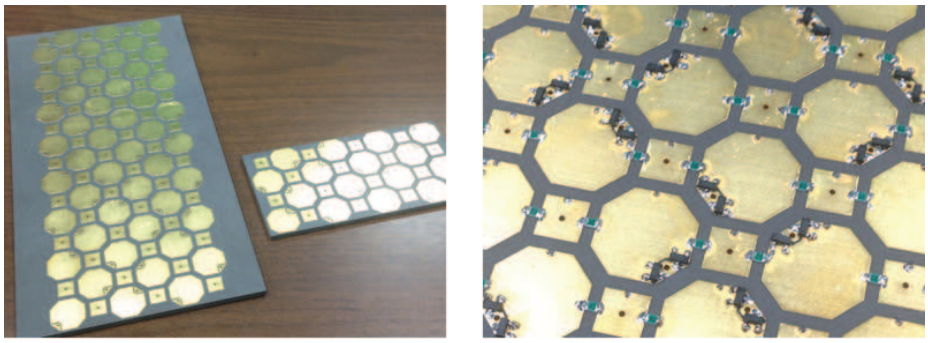

Figure 6.10: Fabrication model of the omni-directional metasurface.

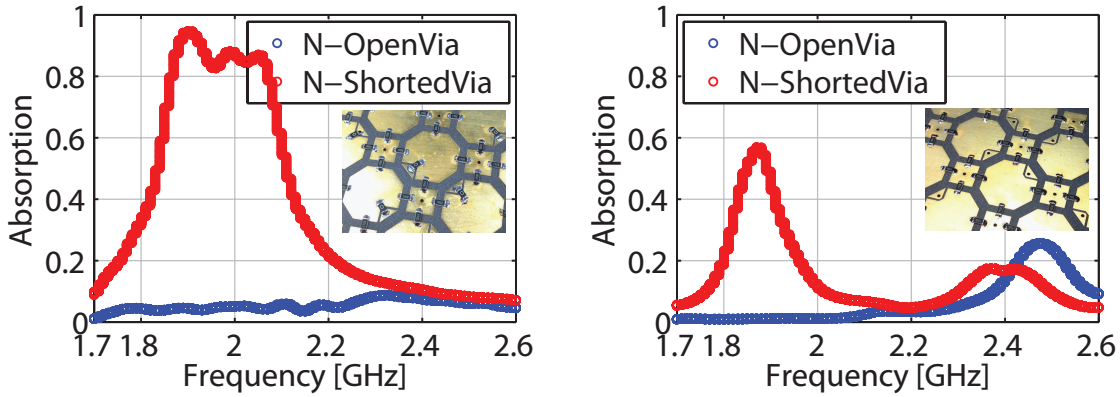

Figure 6.11: Measurement data of the omni-directional metasurface.

sistors, 2.2$k\Omega$, for the dissipation of the surface waves were deployed on the gap between the patches, and a pair of diodes or a 0Ω resistor was populated on a slot on the octagon patch to give on/off states depending on the input power levels. In the measurement, the 0Ω resistor soldered the slot of the large patches to show off/on states. From the parallel case measurement, a huge transition is verified in the short and open situations, and the high absorption magnitude is observed at 1.88 GHz. Similarly, the normal measurement data is shown in Fig. 6.11, and the absorption magnitude under the short offset via environments is shown around 60% due to a limited number of unit cells of the sample. Even though the absorption rate is smaller than the simulation data, the parallel and normal absorption peak have the maximum magnitude at 1.88 GHz.

6.4 Conclusion

In this chapter, we demonstrate a novel metasurface for adapting incoming plane waves in all directions for practical applications. By applying the anisotropic surface topology and an offset via concept, the metasurface responded to the incident waves with all oblique angles including the azimuthal and elevation planes. Thus, the proposed omni-directional metasurface can be applicable to even or curvature surfaces, advanced antenna systems to minimize the surface currents, and other possible implementations.

Chapter 6 is based on and is mostly a reprint of the following paper: **S. Kim**, A. Li, D. Sievenpiper, Omni-directional metamaterial surface, in preparation. The dissertation author was the primary author of the work in this chapter, and the co-authors have approved the use of the material for this dissertation.

Chapter 7

Conclusion

7.1 Summary of Work

This thesis presents a comprehensive overview of the advantages and implementations of the nonlinear active metamaterial surfaces.

Chapter 1 introduced the motivation of the research and the advantages of using a metamaterial surface for application in microwave absorbing structures.

Chapter 2 addressed the theoretical limitations for the TM surface wave attenuation while applying an impedance sheet on the grounded dielectric substrate. The analytical solutions derived were based on Maxwell's equations. The solutions were verified with by numerical simulation methods in Ansys HFSS.

Chapter 3 presented a power dependent metamaterial absorber. A pair of series diodes are embedded on the metasurface, and it played a role in the switch depending on input power levels. In other words, if the high power inputs were incoming to the metasurface, the surface is transformed to an absorber. On the other hand, the metallic structure worked ordinary metal sheet when low powers were illuminated on the surface.

Chapter 4 examined the theory and concept of the self-tuning metasurface. The novel metasurface is divided into parts to adapt to incoming frequencies. The sensing circuit part is a kind of feedback circuit used to generate proper DC bias to control the varactor diodes for tuning. Therefore, the self-tuning metasurface can be achievable for the broadband absorbing application.

Chapter 5 studied a transistor based ground plane. The reconfigurable surface can be manipulated by RF MOSFET switches between the patches. After modifying the impedance topology of the surface, the reconfigurable plane had an octave tunability to cover an extreme broadband frequency range. The metasurface can be applicable to broadband antenna systems and multi-antennas sharing the same ground plane.

Chapter 6 presented an omni-directional metasurface to respond to all incoming waves with oblique angles. To achieve that goal, anisotropic topology and offset vis concepts were applied to the metasurface.

7.2 Future Work

Adapting nonlinear circuit components to metamaterial surfaces can make unique electromagnetic performances possible such as the power dependent absorber, self-tunability, and all directional responses. However, most of the circuit components have internal parasitic parameters, and the parasitic values cause unexpected drawbacks, higher harmonics, and internal losses. Therefore, minimizing or canceling the parasitic circuit like a non-Foster circuit will expand the implementations into various fields.

Bibliography

[1] *Scientific American: Supplement*. Munn and Company, 1917, no. v. 84.

[2] D. F. Sievenpiper, "Nonlinear grounded metasurfaces for suppression of high-power pulsed rf currents," *IEEE Antennas and Wireless Propagation Letters*, vol. 10, pp. 1516–1519, 2011.

[3] S. W, "Absorbent body for electromagnetic waves," Jun. 10 1952, uS Patent 2,599,944. [Online]. Available: https://www.google.com/patents/US2599944

[4] R. L. Fante and M. T. McCormack, "Reflection properties of the salisbury screen," *IEEE Transactions on Antennas and Propagation*, vol. 36, no. 10, pp. 1443–1454, Oct 1988.

[5] R. Gilbert, "Thin, broadband salisbury screen absorber," Mar. 25 2003, uS Patent 6,538,596. [Online]. Available: https://www.google.com/patents/US6538596

[6] D. Sievenpiper, L. Zhang, R. F. J. Broas, N. G. Alexopolous, and E. Yablonovitch, "High-impedance electromagnetic surfaces with a forbidden frequency band," *IEEE Transactions on Microwave Theory and Techniques*, vol. 47, no. 11, pp. 2059–2074, Nov 1999.

[7] F. Costa, A. Monorchio, and G. Manara, "Analysis and design of ultra thin electromagnetic absorbers comprising resistively loaded high impedance surfaces," *IEEE Transactions on Antennas and Propagation*, vol. 58, no. 5, pp. 1551–1558, May 2010.

[8] N. I. Landy, S. Sajuyigbe, J. J. Mock, D. R. Smith, and W. J. Padilla, "Perfect metamaterial absorber," *Phys. Rev. Lett.*, vol. 100, p. 207402, May 2008.

[9] V. G. Veselago, "The electrodynamics of substances with simultaneously negative values e and u," *Sov. Phys. Uspekhi*, vol. 10, no. 4, p. 509, 1968.

[10] R. A. Shelby, D. R. Smith, and S. Schultz, "Experimental verification of a negative index of refraction," *Science*, vol. 292, no. 5514, pp. 77–79, 2001.

[11] D. Schurig, J. Mock, B. Justice, S. Cummer, J. Pendry, A. Starr, and D. Smith, "Metamaterial electromagnetic cloak at microwave frequencies," *Science*, vol. 314, no. 5801, pp. 977–980, 11 2006.

[12] M. C. K. Wiltshire, J. B. Pendry, I. R. Young, D. J. Larkman, D. J. Gilderdale, and J. V. Hajnal, "Microstructured magnetic materials for rf flux guides in magnetic resonance imaging," *Science*, vol. 291, no. 5505, pp. 849–851, 2001.

[13] D. R. Smith, W. J. Padilla, D. C. Vier, S. C. Nemat-Nasser, and S. Schultz, "Composite medium with simultaneously negative permeability and permittivity," *Phys. Rev. Lett.*, vol. 84, pp. 4184–4187, May 2000.

[14] M. Gokkavas, K. Guven, I. Bulu, K. Aydin, R. S. Penciu, M. Kafesaki, C. M. Soukoulis, and E. Ozbay, "Experimental demonstration of a left-handed metamaterial operating at 100 GHz," *Phys. Rev. B*, vol. 73, p. 193103, May 2006.

[15] T. J. Yen, W. J. Padilla, N. Fang, D. C. Vier, D. R. Smith, J. B. Pendry, D. N. Basov, and X. Zhang, "Terahertz magnetic response from artificial materials," *Science*, vol. 303, no. 5663, pp. 1494–1496, 2004.

[16] S. Zhang, W. Fan, N. C. Panoiu, K. J. Malloy, R. M. Osgood, and S. R. J. Brueck, "Experimental demonstration of near-infrared negative-index metamaterials," *Phys. Rev. Lett.*, vol. 95, p. 137404, Sep 2005.

[17] G. Dolling, M. Wegener, C. M. Soukoulis, and S. Linden, "Negative-index metamaterial at 780 nm wavelength," *Opt. Lett.*, vol. 32, no. 1, pp. 53–55, Jan 2007.

[18] V. M. Shalaev, W. Cai, U. K. Chettiar, H.-K. Yuan, A. K. Sarychev, V. P. Drachev, and A. V. Kildishev, "Negative index of refraction in optical metamaterials," *Opt. Lett.*, vol. 30, no. 24, pp. 3356–3358, Dec 2005.

[19] J. B. Pendry, "Negative refraction makes a perfect lens," *Phys. Rev. Lett.*, vol. 85, pp. 3966–3969, Oct 2000.

[20] Y. S. K. Nikolay I. Zheludev, "From metamaterials to metadevices," *Nature Materials*, vol. 11, pp. 917–924, October 2012.

[21] A. V. Kildishev, A. Boltasseva, and V. M. Shalaev, "Planar photonics with metasurfaces," *Science*, vol. 339, no. 6125, 2013.

[22] N. Yu, P. Genevet, M. A. Kats, F. Aieta, J.-P. Tetienne, F. Capasso, and Z. Gaburro, "Light propagation with phase discontinuities: Generalized laws of reflection and refraction," *Science*, vol. 334, no. 6054, pp. 333–337, 2011.

[23] P. Genevet, N. Yu, F. Aieta, J. Lin, M. A. Kats, R. Blanchard, M. O. Scully, Z. Gaburro, and F. Capasso, "Ultra-thin plasmonic optical vortex plate based on phase discontinuities," *Applied Physics Letters*, vol. 100, no. 1, p. 013101, 2012.

[24] E. H. Khoo, E. P. Li, and K. B. Crozier, "Plasmonic wave plate based on subwavelength nanoslits," *Opt. Lett.*, vol. 36, no. 13, pp. 2498–2500, Jul 2011.

[25] Y. Zhao and A. Alù, "Manipulating light polarization with ultrathin plasmonic metasurfaces," *Phys. Rev. B*, vol. 84, p. 205428, Nov 2011.

[26] Y. Liu and X. Zhang, "Metasurfaces for manipulating surface plasmons," *Applied Physics Letters*, vol. 103, no. 14, p. 141101, 2013.

[27] S. B. Glybovski, S. A. Tretyakov, P. A. Belov, Y. S. Kivshar, and C. R. Simovski, "Metasurfaces: From microwaves to visible," *Physics Reports*, vol. 634, pp. 1 – 72, 2016, metasurfaces: From microwaves to visible.

[28] C. Balanis, "Advanced enginerring electromechanics," 1989.

[29] G. Goubau, "Surface waves and their application to transmission lines," *Journal of Applied Physics*, vol. 21, no. 11, pp. 1119–1128, 1950.

[30] C. A. Balanis, *Antenna theory: analysis and design*. John Wiley & Sons, 2016.

[31] A. Vallecchi, J. R. D. Luis, F. Capolino, and F. D. Flaviis, "Low profile fully planar folded dipole antenna on a high impedance surface," *IEEE Transactions on Antennas and Propagation*, vol. 60, no. 1, pp. 51–62, Jan 2012.

[32] S. S. Attwood, "Surfacewave propagation over a coated plane conductor," *Journal of Applied Physics*, vol. 22, no. 4, pp. 504–509, 1951.

[33] K. N. Rozanov, "Ultimate thickness to bandwidth ratio of radar absorbers," *IEEE Transactions on Antennas and Propagation*, vol. 48, no. 8, pp. 1230–1234, Aug 2000.

[34] B. A. Munk, *Frequency selective surfaces*. John Wiley & Sons, 2005.

[35] C. L. Holloway, D. C. Love, E. F. Kuester, J. A. Gordon, and D. A. Hill, "Use of generalized sheet transition conditions to model guided waves on metasurfaces/metafilms," *IEEE Transactions on Antennas and Propagation*, vol. 60, no. 11, pp. 5173–5186, Nov 2012.

[36] R. E. Collin, *Foundations for microwave engineering*. John Wiley & Sons, 2007.

[37] G. Goussetis, J. L. Gomez-Tornero, A. P. Feresidis, and N. K. Uzunoglu, "Artificial impedance surfaces for reduced dispersion in antenna feeding systems," *IEEE Transactions on Antennas and Propagation*, vol. 58, no. 11, pp. 3629–3636, Nov 2010.

[38] W. B. Weir, "Automatic measurement of complex dielectric constant and permeability at microwave frequencies," *Proceedings of the IEEE*, vol. 62, no. 1, pp. 33–36, Jan 1974.

[39] G. T. Ruck, D. E. Barrick, W. D. Stuart, and C. K. Krichbaum, *Radar cross section handbook*. Plenum press New York, 1970, vol. 1.

[40] E. F. Knott, *Radar cross section measurements*. Springer Science & Business Media, 2012.

[41] and others, "Absorbent body for electromagnetic waves," Jun. 10 1952, uS Patent 2,599,944.

[42] B. A. Munk, "Frequency selective surfaces theory and design. john wiley&sons," 2000.

[43] H. Tao, N. I. Landy, C. M. Bingham, X. Zhang, R. D. Averitt, and W. J. Padilla, "A metamaterial absorber for the terahertz regime: Design, fabrication and characterization," *Optics express*, vol. 16, no. 10, pp. 7181–7188, 2008.

[44] H. Li, L. H. Yuan, B. Zhou, X. P. Shen, Q. Cheng, and T. J. Cui, "Ultrathin multiband gigahertz metamaterial absorbers," *Journal of Applied Physics*, vol. 110, no. 1, p. 014909, 2011.

[45] F. Ding, Y. Cui, X. Ge, Y. Jin, and S. He, "Ultra-broadband microwave metamaterial absorber," *Applied physics letters*, vol. 100, no. 10, p. 103506, 2012.

[46] S. Kim and D. F. Sievenpiper, "Theoretical limitations for tm surface wave attenuation by lossy coatings on conducting surfaces," *IEEE Transactions on Antennas and Propagation*, vol. 62, no. 1, pp. 475–480, 2014.

[47] H. Wakatsuchi, S. Kim, J. J. Rushton, and D. F. Sievenpiper, "Circuit-based nonlinear metasurface absorbers for high power surface currents," *Applied Physics Letters*, vol. 102, no. 21, p. 214103, 2013.

[48] ——, "Waveform-dependent absorbing metasurfaces," *Physical review letters*, vol. 111, no. 24, p. 245501, 2013.

[49] Z. Luo, X. Chen, J. Long, R. Quarfoth, and D. Sievenpiper, "Nonlinear power-dependent impedance surface," *IEEE Transactions on Antennas and Propagation*, vol. 63, no. 4, pp. 1736–1745, 2015.

[50] D. F. Sievenpiper, J. H. Schaffner, H. J. Song, R. Y. Loo, and G. Tangonan, "Two-dimensional beam steering using an electrically tunable impedance surface," *IEEE Transactions on Antennas and Propagation*, vol. 51, no. 10, pp. 2713–2722, Oct 2003.

[51] I. Gil, J. Garcia-Garcia, J. Bonache, F. Martin, M. Sorolla, and R. Marques, "Varactor-loaded split ring resonators for tunable notch filters at microwave frequencies," *Electronics Letters*, vol. 40, no. 21, pp. 1347–1348, Oct 2004.

[52] O. Reynet and O. Acher, "Voltage controlled metamaterial," *Applied Physics Letters*, vol. 84, no. 7, pp. 1198–1200, 2004.

[53] T. Hand and S. Cummer, "Characterization of tunable metamaterial elements using mems switches," *IEEE Antennas and Wireless Propagation Letters*, vol. 6, pp. 401–404, 2007.

[54] A. R. Katko, J. P. Barrett, and S. A. Cummer, "Time-varying transistor-based metamaterial for tunability, mixing, and efficient phase conjugation," *Journal of Applied Physics*, vol. 115, no. 14, p. 144501, 2014.

[55] F.-R. Yang, K.-P. Ma, Y. Qian, and T. Itoh, "A uniplanar compact photonic-bandgap (uc-pbg) structure and its applications for microwave circuits," 1999.

[56] G. Goussetis, A. P. Feresidis, and J. C. Vardaxoglou, "Tailoring the amc and ebg characteristics of periodic metallic arrays printed on grounded dielectric substrate," *IEEE Transactions on Antennas and Propagation*, vol. 54, no. 1, pp. 82–89, Jan 2006.

[57] S. A. Tretyakov and S. I. Maslovski, "Thin absorbing structure for all incidence angles based on the use of a high-impedance surface," *Microwave and Optical Technology Letters*, vol. 38, no. 3, pp. 175–178, 2003. [Online]. Available: http://dx.doi.org/10.1002/mop.11006

[58] O. Luukkonen, M. G. Silveirinha, A. B. Yakovlev, C. R. Simovski, I. S. Nefedov, and S. A. Tretyakov, "Effects of spatial dispersion on reflection from mushroom-type artificial impedance surfaces," *IEEE Transactions on Microwave Theory and Techniques*, vol. 57, no. 11, pp. 2692–2699, Nov 2009.